Copyright Undertaking

MACHINE LEARNING-BASED INTEGRATION OF MULTI-SATELLITE INSAR TO RETRIEVE LONG-TERM TIME SERIES DISPLACEMENT

HASSAN DOHA AMR ABDELTAWWAB ABDELMEGEED

PhD

The Hong Kong Polytechnic University

2025

The Hong Kong Polytechnic University
Department of Land Surveying and GeoInformatics

Machine Learning-based Integration of Multi-satellite InSAR to Retrieve Long-term Time Series Displacement

Hassan Doha Amr Abdeltawwab Abdelmegeed

A thesis submitted in partial fulfillment of the requirements for
the degree of Doctor of Philosophy
August 2024

CERTIFICATE OF ORIGINALITY

I hereby declare that this thesis is my own work and that, to the best of my knowledge and belief, it reproduces no material previously published or written, nor material that has been accepted for the award of any other degree or diploma, except where due acknowledgment has been made in the text.

Signature: ______________ __________

Name of Student: Hassan Doha Amr Abdeltawwab Abdelmegeed

Abstract

In the world's fast-growing mega-cities, ground deformation is one of the crucial issues threatening many cities in both societal and economic aspects. Traditional field procedures (e.g., leveling and global navigation satellite system (GNSS)) have been utilized for deformation monitoring. Notwithstanding these methods' high reliability, their main drawbacks are low spatial resolution in large-scale projects, relatively high cost, and lack of manpower. In contrast, remote sensing techniques, particularly, differential InSAR (DInSAR) provide high-resolution deformation maps in large-spatial coverage at high levels of accuracy. Recently, synthetic aperture radar (SAR) data are available from diverse bands including C-band (e.g., SIR-C, European remote-sensing satellite (ERS), ENVISAT, RADARSAT-1/2, and Sentinel-1), X-band (e.g., TerraSAR-X and COSMO-SkyMed), L-band (e.g., JERS, ALOS-1/2, TerraSAR-L, and DESDynl), and P-band (e.g., BIOMASS). A key challenge of integrating multi-band SAR datasets is that they have diverse maximum detection gradients, degrees of decorrelation, noise rejection capability, etc. The integration of multiple operational bands, polarimetric channels, and orbit orientations is anticipated to enrich the gained information thus enabling depth interpretation of the surface deformation. In this research, the problem of integrating multi-satellite SAR data is addressed based on two aspects (1) adaptation of the traditional small baseline subset (SBAS) time series and (2) utilization of machine learning machine learning (ML) to perform integration. The proposed methodology exploits complementary information from different SAR data to generate integrated long-term ground displacement time series.

Part I of this thesis focuses on the integration of multi-satellite SAR data by adaptation of traditional SBAS. The proposed method is employed to generate the vertical displacement maps of Almokattam City in Egypt from 2000 to 2020. The experiments have shown promising results based on ERS, ENVISAT, and Sentinel-1A interferograms. Significantertical deformation has been recorded along the west of the city with a mean value of - 2.32 mm/year and a standard deviation of 0.21 mm/year. Moreover, the research findings are in line with those from previous studies in the area. Accordingly, the proposed integration approach has great potential in retrieving long-term vertical displacement based on multi-satellite SAR data.

In part II of the thesis, machine learning is used to integrate multi-satellite SAR data. At least a pair of SAR images from complementary tracks is the input of the proposed method. The line-of-sight (LOS) displacements are computed based on DInSAR at a series of high-coherence points. The vertical components of displacement are then computed from the recovered LOS displacement. After that, the vertical displacement maps are geocoded to the ground coordinate system. Finally, the support vector regression (SVR) is used to integrate the displacement on a pixel-by-pixel basis. The proposed method does not employ simultaneous processing of huge DInSAR interferogram sequences, which is a key advantage compared to other methods. The SVR integration is tested using COSMO-SkyMed (CSK),TerraSAR-X (TSX) images, and a small monitoring cycle Sentinel-1 (S1) images to monitor the deformation of the reclaimed territories near Hong Kong Kowloon City. The results show that the average annual displacement (AAD) ranges from -12.86 to 11.63 mm/year from 2008 to 2020 with a Standard Deviation (STD) of 0.69 mm/year. Moreover, the root mean square error (RMSE), MAE, correlation coefficient, and R-squared are computed. Accordingly, a potential performance of the proposed method in multi-satellite SAR data integration has been recorded.

Publications Arising from the Thesis

1. Doha. Amr, Xiao-Li. Ding, and Reda. Fekry, “A Multi-Satellite SBAS for Retrieval of Long-term Ground Displacement Time Series”, *Remote Sensing MDPI 2024*(Q1(WoS) & IF = 5.0).
2. Doha. Amr, Xiao-Li. Ding, and Reda. Fekry, “A machine learning-based method for multi-satellite SAR data integration”, in *The Egyptian Journal of Remote Sensing and Space Sciences (EJRS)* (2023). (Q1(WoS) & IF = 6.4).

Acknowledgments

I am immensely fortunate to have had the privilege of pursuing a Ph.D., as it provided me with the opportunity to collaborate with a multitude of enthusiastic and brilliant individuals who have made invaluable contributions to the completion of my dissertation. I express my deepest gratitude to Allah for allowing me to be a part of the esteemed research team at PolyU. I extend my sincerest appreciation to my Ph.D. supervisor, Prof. DING Xiao-Li, whose exceptional guidance and unwavering support shaped the direction of my research and granted me the freedom to explore topics that ignited my scientific curiosity. I am indebted to my friends for their unwavering support and enduring interest in my work, and I extend special thanks to my closest companions at LSGI, whose instrumental support led to the successful completion of my Ph.D. Finally, I am profoundly grateful to my family for their constant support and encouragement, as their unwavering belief in me has been a constant source of strength and motivation. I am genuinely honored to have had the opportunity to work with such exceptional individuals, and I extend my heartfelt appreciation to all those who have contributed to my Ph.D. journey.

Dedication

This thesis is dedicated to my beloved father Amr Abdeltawwab: Dedicate this work to your pure spirit, with the grace of Allah Almighty, to bless you with His mercy. This work is also dedicated to my mother, husband, and children (Roaa and Abdulrahman): May Allah protect and bless you all.

List of Abbreviations

AD	Anderson-Darlington
KS	Kolmogorov-Smirnov
3D	three-dimensional
2D	two-dimensional
AAD	average annual displacement
APS	atmospheric phase screen
AZPO	azimuth pixel offset
CSK	COSMO-SkyMed
DEM	digital elevation model
ERS	European remote-sensing satellite
ENVISAT	Environmental Satellite
E-W	east-west
InSAR	interferometric synthetic aperture radar
DInSAR	differential InSAR

DS	distributed scatterers
DLR	German Space Agency
GNSS	global navigation satellite system
GPS	global positioning system
LiDAR	Light Detection and Ranging
LS	least squares
LMS	least mean squares
LOS	line-of-sight
LP	low pass
ML	machine learning
MinA	minimal acceleration
MQQA	modified quantile-quantile adjustment
MT-InSAR	multi-temporal InSAR
MSBAS	multidimensional small baseline subset
MTI	multi-temporal interferometry
N-S	north-south
OTL	ocean tide loads
PO	pixel offset
PO-SBAS	pixel-offset SBAS
PSI	persistent scatterer interferometry

PS	persistent scatterers
PRF	pulse repetition frequency
RADAR	RAdio Detecting And Ranging
RBF	radial basis function
RAR	real aperture radar
RMSE	root mean square error
S1	Sentinel-1
SAR	synthetic aperture radar
SBAS	small baseline subset
SCR	signal-to-cluster ratio
SLC	single look complex
SM	single master
SNR	signal to noise ratio
SRTM	shuttle radar topography mission
SHP	statistically homogeneous pixel
SVD	singular value decomposition
SVM	support vector machine
SVR	support vector regression
TSVD	truncated singular value decomposition
TSX	TerraSAR-X

U-D	up-down
CNNs	convolutional neural networks
TanDEM-X	TanDEM-X
MMSBAS	Modified Multi-satellite SBAS
GIS	Geographic Information System
STD	Standard Deviation

Contents

List of Figures

List of Tables

Chapter 1

INTRODUCTION

This chapter lays the groundwork for the proposed research by first establishing the relevant background and context. Following this, a clear and concise statement of the research problem and the existing gaps in knowledge will be presented. The chapter then outlines the specific research objectives that this dissertation aims to achieve. Finally, to provide a roadmap for the reader, the overall structure of the dissertation will be presented.

1.1 Background

ne of the most pressing threats to life and property in rapidly expanding megacities is ground deformation. Human activities related to urbanization—such as land reclamation, groundwater extraction, and underground construction [4]—can significantly contribute to ground deformation. So, it is important to monitor and study the long-term earth surface deformation to make an early warning and to prevent disasters related to this displacement. Traditional methods for observing and monitoring ground deformation include ground leveling and global positioning system (GPS) measurements. Ground leveling, when combined with advanced GPS technology and precise control point coordinates, allows for an accurate assessment of ground motion. However, these traditional methods face challenges in expanding urban areas, including limited manpower, high costs of additional measurements, and difficulties in covering extensive areas over time and space [2]. To address these challenges and consistently map ground deformation over large areas, advanced remote sensing techniques were developed as Synthetic aperture radar SAR interferometry, also termed interferometric synthetic aperture radar (InSAR) [5].

InSAR, is an active remote sensing technique for observing the Earth's surface. It can measure the digital elevation model (DEM) of Earth or ground deformation by exploring the phase difference of two SAR images (Differential InSARDInSAR) (i.e., the interferometric phase, the measurement of InSAR) in the same area. acDInSAR has become one of the most useful geodetic techniques for ground deformation measurement due to its all-weather and day-and-night imaging capability, wide-coverage (over hundreds of kilometers), high spatial resolution (meter-level), and high measurement accuracy [6, 7, 8, 9]. Due to the extensive availability of SAR images, DInSAR technology has proven highly effective in mapping surface changes and monitoring active deformation areas associated with earthquakes [10, 11], volcanic eruptions [12], glacial movements [13], landslides [14], underground mining [15], land reclamation

[16], and subsidence [17].

In a traditional DInSAR technique, the phase difference between two SAR acquisitions includes contributions from topography, atmospheric delay and decorrelation noise, as well as information from the elevation reference surface. After removing the phase components related to the elevation reference surface and topography, the phase difference attributed to the deformation signal can be isolated. However, this approach often struggles to eliminate other phases, such as atmospheric artifacts, decorrelation noise, and topographic errors, which can obscure small displacements [18, 19, 20, 21]. These unexpected phase components are referred to as error sources, and effectively correcting them is crucial for accurate deformation retrieval in DInSAR processing. Also, DInSAR is limited in observing long-term time-series deformation of the earth's surface [22]. Consequently, several multi-temporal InSAR multi-temporal InSAR (MT-InSAR) techniques have been developed to examine the temporal evolution of land deformation and map ground deformation, thus mitigating space-time decorrelation issues inherent in traditional DInSAR techniques [23].

The MT-InSAR techniques are classified into three main categories: persistent scatterer interferometry (PSI) [24, 25, 26, 27, 28, 29], SBAS [30, 31, 32, 17, 33, 34], and the fusion of PSI and SBAS [35, 36, 37, 38]. The PSI approach extracts phase information from point-like persistent scattererss (PSs), which are typically stable features like large rock outcrops or man-made structures. This method generates $N-1$ single master (SM) interferograms from N single-look SAR images and selects isolated PSs to derive displacement time series. However,PSI is most effective in urban or semi-urban areas due to the scarcity PSs in rural regions [39, 40]. On the other hand, SBAS uses distributed scattererss (DSs) in interferograms with small spatial and temporal baselines, which often show moderate correlations. By employing spatial multilooking to enhance the signal-to-noise ratio of these targets, it SBAS performs well in rural areas with many DSs due to the use of short baselines and multilooked pixels [41]. The third technique integrates PSI and SBAS combines phase information from both

PSs and DSs. Recent advancements in MT-InSAR improving phase quality by using a full combination of interferograms and collaborative processing with PSs within the SM interferogram framework [35, 42]. These approaches improve the accuracy of deformation retrieval while minimizing the impact of the error source through spatial and temporal modeling.

With the progress of InSAR and MT-InSAR techniques, a growing number of SAR satellites have been launched, including C-band (SIR-C, ERS, ENVISAT, RADARSAT-1/2, and Sentinel-1), X-band (TerraSAR-X and COSMO-SkyMed), L-band (JERS, ALOS-1/2, TerraSAR-L, and DESDynI), and P-band (BIOMASS) [43], as shown in Figure 1.1. These multi-band SAR datasets, with varying imaging parameters such as azimuth and incidence angle, spatial and temporal resolution, orbit direction, and wavelength, enable in-depth comparison and analysis of surface deformation. They offer different characteristics in terms of maximum detection gradient, degree of decorrelation, and noise rejection capability [44].

With the increasing availability of SAR images, new methodologies are being developed to optimize the processing and analysis of the vast amounts of data gathered by constellations of next-generation SAR sensors. These advancements aim to extract new insights from the combined use of multiple operational bands, polarimetric channels, and orbit orientations [45]. Previous research by Pepe et al. [46] has explored this by applying a time-dependent geotechnical model of observed deformation to solve a non-linear optimization problem using the Levenberg-Marquardt method. Additionally, the computation of three-dimensional (3D) components of ground deformation velocity has been a focus in multi-sensor DInSAR studies [47, 48, 49, 50, 51]. Recent approaches for integrating multi-satellite and multi-angle SAR data have enabled the development of long-term 3D time-series of ground deformation, including vertical, east-west, and north-south components [51, 46, 52, 53]. Notable techniques include minimal acceleration (MinA) [54], which combines radar line-of-sight (LOS)-projected time-series of deformation from various SAR platforms by ensuring that 3D displace-

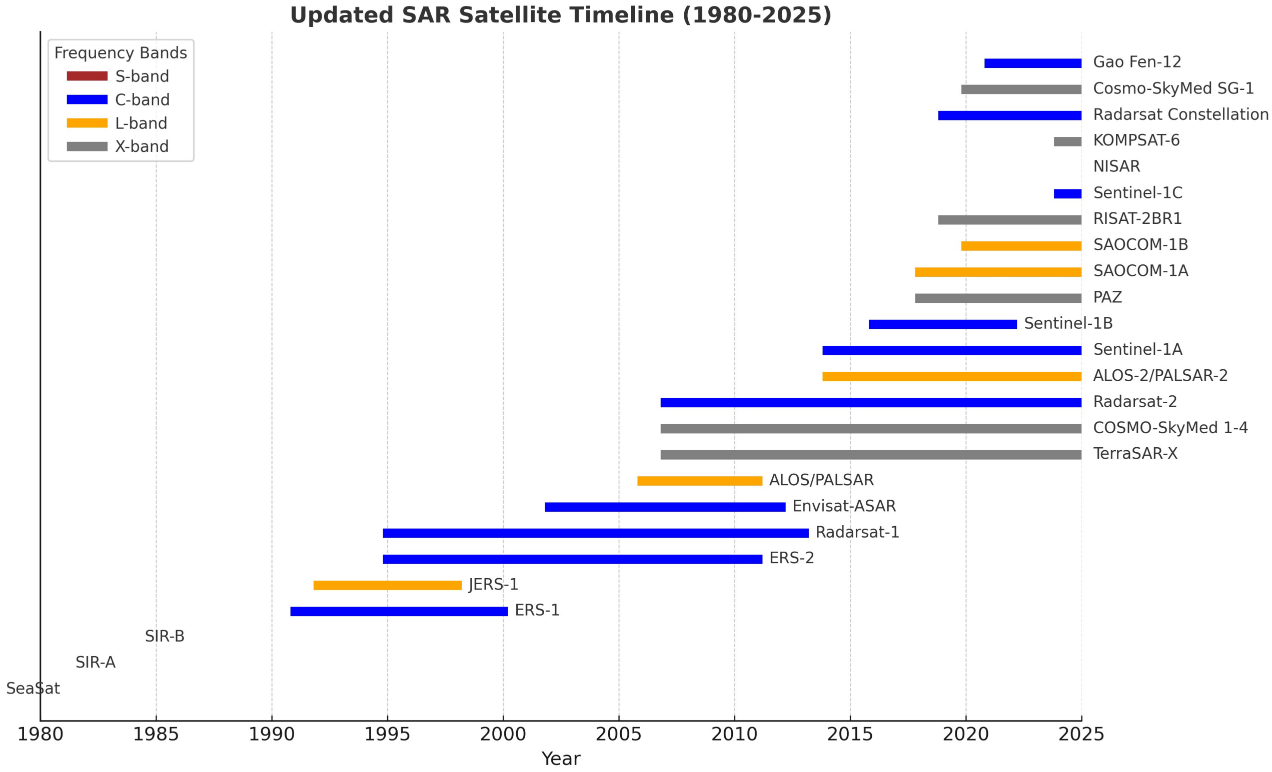

Figure 1.1: SAR satellites.

ment components have minimal accelerations independently. Another approach, the modified quantile-quantile adjustment (MQQA) method [55], links time-overlapped multi-satellite DInSAR deformation time-series, analyzing nearly 12 years of SAR data to produce long-term displacement time-series for the ocean-reclaimed lands of Shanghai. The Multidimensional Time Series (MasTer) toolbox [56], a fully automatic, unsupervised processing chain based on the multidimensional small baseline subset (MSBAS) method [57, 58, 52, 59], is another example of recent advancements.

From the literature, while numerous research studies have explored the integration of multi-satellite InSAR data, several challenges remain. First, processing large archives of SAR images and interferograms simultaneously is computationally intensive and requires high-performance computing resources. Second, integrating time-gapped data presents difficulties, as previous studies have addressed this issue using time-dependent deformation models, which can lead to boundary non-convergence problems. Additionally, these time gaps contribute to the emergence of low-coherence areas in displacement results. Third, cross-sensor biases arise due to differences in satellite sensors, imaging geometries, viewing angles, atmospheric conditions at different acquisition times, and variations in orbital parameters. These biases are challenging to estimate and correct, complicating the generation of accurate long-term displacement measurements.

1.2 Motivation and Research Questions

This thesis research is motivated by two key factors. First, the increasing availability of SAR data from multiple radar satellites operating in the same region but at different wavelengths, viewing angles, and acquisition modes presents a challenge in effectively integrating these diverse datasets. Efficiently combining the information from various SAR satellites is essential to maximize their collective advantages. Second, there is a growing interest in leveraging machine learning ML techniques to extract valuable insights from InSAR data and its associated products. ML-based SAR algorithms have been developed for a range of applications, including object detection, terrain classification, surface displacement analysis, parameter inversion, and despeckling. These advancements enable better interpretation of SAR data, addressing both societal and economic needs [60, 61]. Over the past decade, significant research has focused on surface displacement and terrain classification, particularly in distinguishing SAR signal characteristics based on spatial patterns and statistical properties. The anticipated deployment of next-generation SAR sensors, potentially capable of daily revisits through geosynchronous SAR systems, is expected to further enhance the role of ML in integrating multi-satellite SAR data, benefiting both disaster prevention and post-emergency response efforts.

The specific research questions that guide this research are the following:

- How to obtain reliable vertical displacement results from integrating time-gaped

SAR data without an external time-dependent displacement model?

- Which strategy can overcome the statistical and systematic temporal biases in displacement values obtained from multimodal SAR datasets?
- How to overcome the challenges related to data volume and integration complexity "simultaneous processing of vast amounts of images/interferograms"?
- How to overcome low coherence areas resulted from the temporal gap between different SAR satellites?
- What is the role of machine learning techniques in mapping earth displacement from different SAR satellites and overcoming integration challenges of different SAR datasets?

1.3 Objectives and Contributions

The main aim of this research can be summarized as follows:

- Monitoring long-term vertical displacement in regions affected primarily by subsidence by integrating a large dataset of multi-satellite SAR images while addressing or mitigating the challenges associated with this integration.
- Assessing the effectiveness of ML algorithms in integrating multi-satellite SAR data to generate accurate long-term vertical displacement maps.

To address these aims, the research contributions are:

- Develop a post-processing framework to integrate multi-satellite DInSAR data, addressing statistical and systematic temporal biases while eliminating the need for simultaneous processing of hundreds of differential SAR interferograms.

- Apply temporal alignment of SAR data using techniques such as interferometric time series analysis (e.g., Modified Multi-satellite SBAS (MMSBAS)) or by integrating velocities instead of displacement values, as done in ML-based integration methods, to seamlessly merge time-gapped SAR datasets without relying on an external time-dependent displacement model.

- Retrieve the integrated vertical displacement at high-coherence common points selected based on Permanent Scatterers PS and Distributed Scatterers DS measurements, minimizing low-coherence areas caused by temporal gaps between different SAR data acquisitions.

- Developing a ML-based method to integrate multi-band SAR data.

  This machine learning (ML)-based integration method offers several key advantages, enabling automated and efficient multi-satellite SAR data fusion. This approach enhances scalability while reducing manual effort and accelerating the generation of displacement results. The benefits of this method can be outlined as follows:

  1. **Automation and Efficiency** – ML-driven integration automates the fusion of multi-satellite SAR data, minimizing manual intervention and significantly improving processing speed. This allows for the rapid generation of displacement maps, making large-scale applications more feasible.
  2. **Mitigation of Inconsistencies** – Variations in orbital geometries, spatial resolutions, and atmospheric conditions across different satellites introduce discrepancies in displacement measurements. The ML-based approach helps standardize and correct these inconsistencies, leading to more precise and reliable displacement results.
  3. **Adaptive Weighting for Improved Accuracy** – By assigning dynamic weights to displacement data based on reliability factors such as temporal baseline, coherence, and signal quality, ML enhances the accuracy of

integration. This ensures that more reliable data points contribute more significantly to the final displacement maps.

4. **Scalability for Large Datasets** – The vast volume of SAR data generated by multiple satellites requires efficient processing techniques. ML models are capable of handling large-scale, high-dimensional datasets, ensuring seamless integration and analysis without excessive computational overhead.
5. **Identification of Complex Patterns** – Unlike traditional algorithms, ML techniques can detect intricate patterns and relationships in SAR data that may not be immediately apparent. This capability enhances the understanding of ground deformation dynamics and improves the accuracy of displacement estimations. By leveraging ML, this approach optimizes the integration of multi-band SAR data, ensuring greater precision, efficiency, and reliability in generating long-term ground displacement time series

1.4 Thesis Structure

There are five chapters in this thesis, the outline of which are arranged as follows:

Chapter 1 is an introductory chapter that outlines the motivation, research questions, objectives, and research contributions.

Chapter 2 reviews the principles of SAR, InSAR, and DInSAR. We introduce the Limitations of conventional DInSAR. The concept and types of Multi-temporal InSAR are underlined. Moreover, the literature review of Multi-Track/Multi-Satellite InSAR Methodologies. The shortcomings of the existing methods are also highlighted.

Chapter 3 proposes the Modified Multi-Satellite SBAS method. This framework enabled us to generate long-term deformation time series from extended sequences of time-overlapped and time-gapped multi-satellite SAR data. The adopted method is implemented at Almokattam city, located at the upper plateau of Almokattam mountain in Cairo, using three SAR datasets.

Chapter 4 introduces a method for multi-sensor SAR data integration to retrieve long-term ground deformation maps. The proposed method exploits the ML algorithm namely multi-variable SVR. The proposed method was tested in the Kowloon district in Hong Kong using TSX, CSK, and S1 SAR images.

Chapter 5 represents a conclusion and a summary of the contributions leading to providing insight on suggestions for future research.

Chapter 2

SAR, InSAR, and MTInSAR:A Literature Review

This chapter delves into the foundational aspects of deformation mapping using DInSAR. It offers a comprehensive overview of the constraints and latest advanceslti-temporal Interferometric Synthetic Aperture Radar is dedicated to elucidating the general definition and essential characteristics of MT-InSAR. It covers the basics of deformation monitoring and modeling by integrating multi-satellite SAR images. Furthermore, Section 2.5 presents a detailed review of the current state of multi-track and multi-satellite InSAR methodologies for ground deformation mapping, highlighting the latest innovations and methodologies in this field.

2.1 Synthetic Aperture Radar (SAR)

SAR is a radar imaging technique that uses microwave signals to create high-resolution images of the surface of the Earth with a spatial resolution of a few meters which was discovered approximately 50 years ago [62]. SAR employs a frequency-modulated waveform and pulse compression to aggregate several echoes, unlike conventional radar. Based on this concept, SAR can create a synthetic aperture that is much longer than the real one, allowing targets that are illuminated by the same beam to be distinguished and recorded. By employing SAR, it is possible to increase the spatial resolution in the azimuth and range directions to meters-level accuracy. The spatial resolution of the recently launched TerraSAR-X and COSMO-skyMED can even reach 1 meter in azimuth, greatly increasing the amount of observational detail. SAR is therefore capable of differentiating small-scale ground characteristics [63].

The SAR image geometry is shown in Figure 2.1 when a short pulse from the RAdio Detecting And Ranging (RADAR) returns to the antenna with a recording of the back-scattered earth from a location on the earth's surface. The azimuth direction is the direction perpendicular to the motion of the satellite, while the range direction is the direction of illumination. The swath refers to the portion of the Earth's surface that was photographed. The look angle and slant range are represented by the angles θ and range r, respectively. H stands for the satellite's altitude. The nominal slant range resolution, $\Delta\ r$, can be written as the following equation, where tau is the pulse length and C is the light speed.

$$\Delta r = \frac{C\tau}{2} \tag{2.1}$$

The slant range resolution and the ground range resolution are mathematically connected as follows:

$$R_r = \frac{C\tau}{2\sin\theta} \tag{2.2}$$

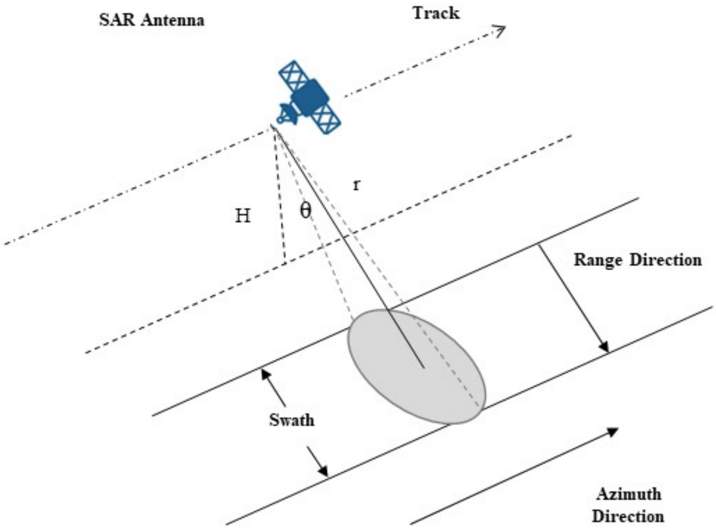

Figure 2.1: SAR imaging geometry.

The look angle is connected to the range resolution, independent of the height of the SAR satellite. The range of resolution is limitless if the look angle is zero. The look angle of the SAR satellite now ranges from 15° to 65°. While reducing pulse length can enhance range resolution, this improvement is constrained by the satellite and ground station data transmission speed. In the case of real aperture radar (RAR), the azimuth resolution is determined by the ratio of the RADAR wavelength λ to the antenna length L, and is expressed as:

$$R'_a = r\tan\theta = \frac{r\lambda}{L} = \frac{\lambda H}{L\cos\theta}, \tag{2.3}$$

where r is the nominal slant range. The azimuth resolution can be greatly enhanced by assembling the synthetic aperture with a length equal to the along-track beam width of length of $2R_a$, and it can be written as:

$$R_a = \frac{\lambda r}{2R_a} = \frac{L}{2} \tag{2.4}$$

The potential resolution of the most popular SAR mode, stripmap mode, is represented by the R_a.Additionally, it is unaffected by the SAR satellite's height. Reducing the antenna length can increase azimuth resolution, but this improvement is constrained by the satellite's motion velocity and pulse repetition frequency (PRF).

The single look complex (SLC) image that makes up the raw SAR image contains data on the brightness (ie., amplitude) and phase of the scatterers on the ground. Airborne and space-borne SAR systems are now used to collect SAR images. Spaceborne SAR systems have the advantages of extensive ground coverage, frequent coverage of the same area, and a large number of multi-temporal SAR images for interferometric processing and surface deformation research. As a result, the primary data source for InSAR deformation monitoring globally has been space-borne SAR images[64, 65].

2.2 Interferometry (InSAR)

InSAR is a radar-based technique widely employed in geodesy and remote sensing. This method leverages two or more SAR images to generate maps of surface deformation or digital elevation, relying on differences in the returning wave phases captured by the satellite [7] or airborne platforms. InSAR enables the detection of deformation changes at the millimeter scale over periods ranging from days to years. It has applications in structural engineering, particularly for monitoring subsidence and ensuring structural stability, as well as in geophysical studies, such as tracking natural hazards like earthquakes, volcanic activity, and landslides.

Satellites equipped with SAR sensors can repeatedly observe the same region from slightly varying perspectives. This can be achieved either simultaneously, using two radars on the same platform, or at different times by exploiting the satellite's repeated orbital paths. The interferogram, a key product of InSAR, is created by cross-multiplying the first SAR image with the complex conjugate of the second image on a pixel-by-pixel basis. The interferometric phase, derived from the difference in phase between the two images, is represented in the interferogram, while its amplitude is the product of the amplitudes of the two images [66]. A typical configuration of the repeat-pass InSAR system is illustrated in Figure 2.1.

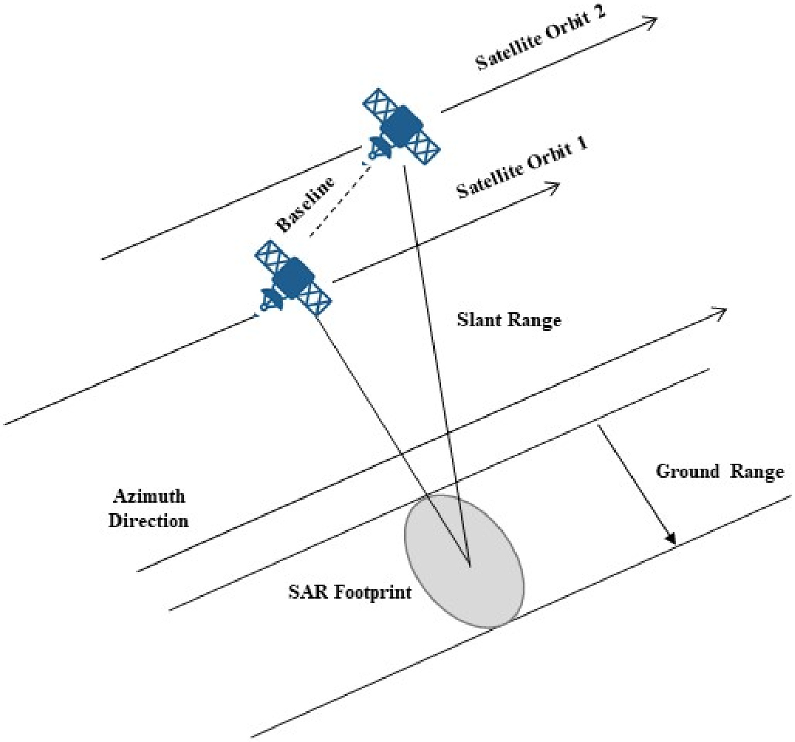

Figure 2.2: Geometry of a satellite InSAR system.

Once a ground reference point is established, the variation in the travel path difference, r, when moving from the reference resolution cell to another can be approximated using a simple expression. This approximation is valid for short baselines and when the resolution cells are relatively close to each other, and it is determined based on a few geometric parameters. This expression is shown in Figure 2.3.

$$\Delta r = -2\frac{B_n q_s}{R}, \tag{2.5}$$

where B_n represents the perpendicular baseline, R is the radar-to-target distance, and q_s represents the displacement between the resolution cells perpendicular to the radar LOS. Thus, the change in the interferometric phase $\Delta\phi$ is determined based on the radar wavelength λ and Δr as follows:

$$\Delta\phi = \frac{2\pi\Delta r}{\lambda} = \frac{4\pi B_n q_s}{\lambda R} \tag{2.6}$$

Several factors, including orbital contribution $\Delta\phi_{orb}$, topographic phase $\Delta\phi_{topo}$, dis-

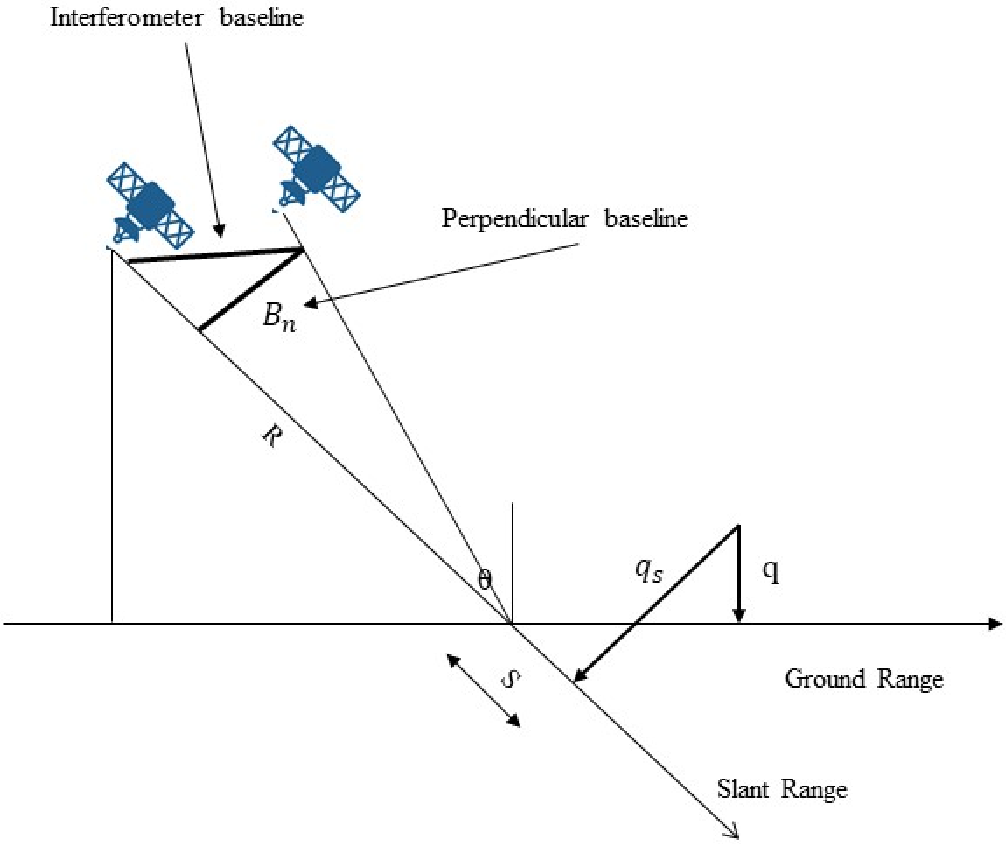

Figure 2.3: Geometric configuration of a satellite-based interferometric SAR system.

placement $\Delta\phi_{def}$, atmospheric effect $\Delta\phi_{atm}$, and phase due to noise $\Delta\phi_{noise}$, contribute to the interferometric phase $\Delta\phi$, Which is:

$$\Delta\phi = \Delta\phi_{orb} + \Delta\phi_{topo} + \Delta\phi_{def} + \Delta\phi_{atm} + \Delta\phi_{noise} \tag{2.7}$$

2.2.1 InSAR for topographic mapping

To gather topography data within the overlapped area of two images, traditional photogrammetry employs stereo mapping. In terms of the InSAR technique, it is necessary to have the phase information from two SAR images that overlap one another to determine the Earth's surface elevation. It is possible to estimate the geometrical and physical relationship between the two-phase observations needed to determine the topographic height using the interferometric arrangement shown in Figure 2.4.

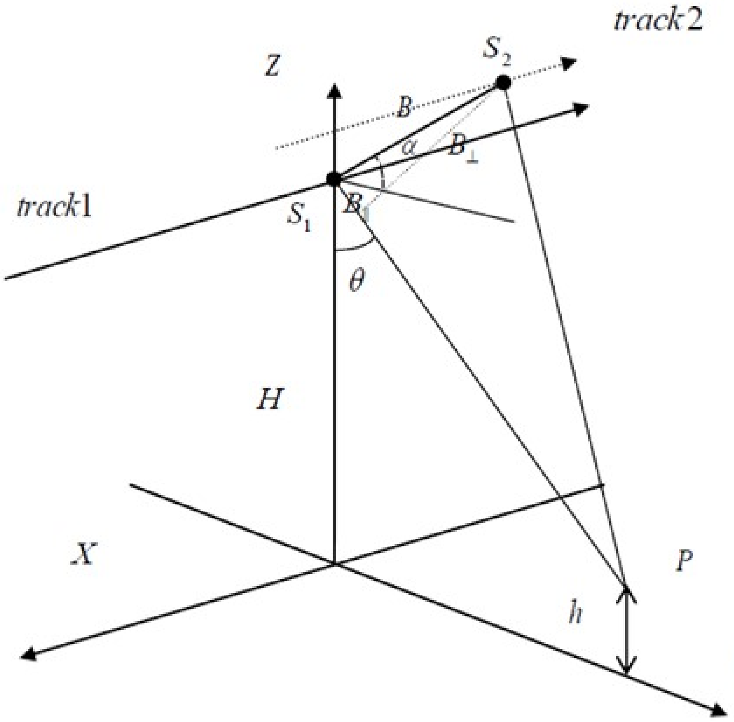

Figure 2.4: InSAR geometric configuration for topographic mapping.

Figure 2.4 illustrates the two SAR satellites S_1 and S_2, with a spatial baseline B. The angle between the baseline vector and the horizontal plane is denoted by α, and the satellite's look angle is represented by θ. The baseline components are split into the parallel baseline $B_{||}$ and the perpendicular baseline $B_\perp$. The figure also indicates the height difference H from a surface reference datum and the target height h relative to that datum. Additionally, the slant range from S_1 to the target point P is given by R, while the slant range from S_2 to P is $R+r$. From this configuration, the following relationships can be derived:

$$h = H - R\cos\theta \tag{2.8}$$

Cosine Law in $\Delta S_1 S_1 P$ allows us to obtain

$$(R+r)^2 = R^2 + B^2 - 2RB\cos\left(\frac{\pi}{2} - \theta + \alpha\right) = R^2 + B^2 - 2RB\sin\left(\theta - \alpha\right) \tag{2.9}$$

On the left side of equation 2.9 after expansion, we obtain

$$R^2 + r^2 + 2Rr = R^2 + B^2 - 2RB\sin(\theta - \alpha), \tag{2.10}$$

such that R^2 is removed from both sides of equation 2.10, and we derive:

$$R = \frac{B^2 - r^2}{2r + 2B\sin(\theta - \alpha)}, \tag{2.11}$$

where r can be defined as:

$$r = -\frac{\lambda\phi}{4\pi}, \tag{2.12}$$

so, using equations 2.8, 2.11 and 2.12, the functional relationship between h and interferometric phase can be written as follows:

$$h = H - \frac{B^2(\frac{\lambda\phi}{4\pi})^2}{2B\sin(\theta - \alpha) - \frac{\lambda\phi}{2\pi}}\cos\theta \tag{2.13}$$

Equation 2.13 shows how the interferometric phase can be used to invert the elevation of the Earth's surface, which allows us to construct the digital elevation model (DEM) of the overlapped region by combining the interferometric phase and the satellite motion parameters for the region. On the contrary, the InSAR technique in practice requires a series of steps to mitigate or remove the contributions and ultimately derive the local DEM. These steps include taking into account the phase contribution by the reference datum, topographic fluctuation, deformation, atmospheric delay, and noise. Generalized summaries of the essential phases in topographic mapping with InSAR include: choosing the suitable SAR images, focusing the SAR images to create SLC images, co-registering SLC images, interferometric processing, applying noise filtering to interferograms, and interferometric processing. Interferograms are processed by deducting the reference and topographic phases, unwrapping the phase, geocoding, and translating the phase to height. Figure 2.5 illustrates the process of InSAR topographic mapping.

2.2.2 InSAR for surface deformation mapping

When a location is observed by a satellite twice or more, and the ground is displaced during that time, the information about the ground displacement is included

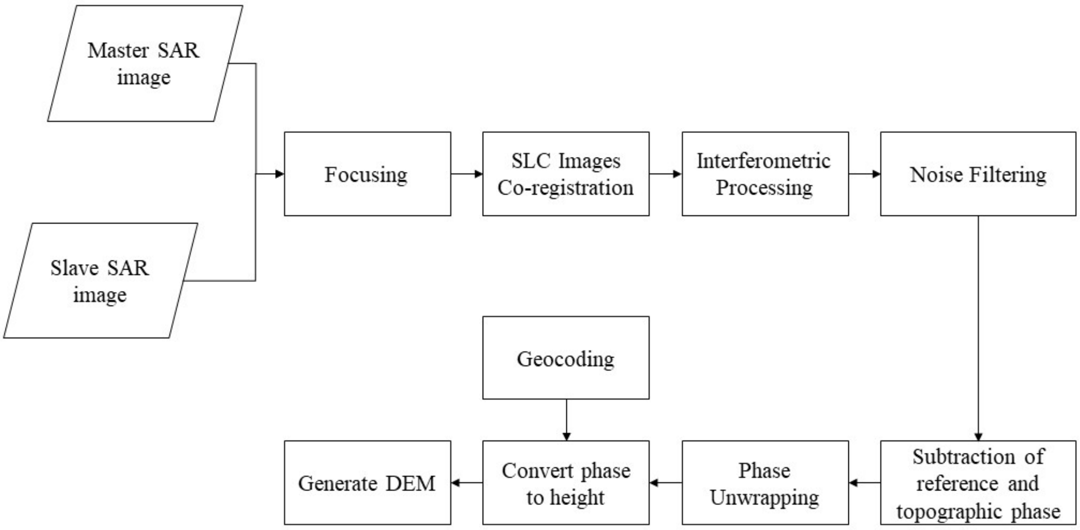

Figure 2.5: Workflow of InSAR topographic mapping.

in the interferogram that is created from these two images in addition to information about the topography. The interference fringe resulting from ground elevation is associated with the baseline distance in the interferogram, incorporating both topographic and ground displacement information. In contrast, the interference fringe caused by ground changes is independent of the baseline distance. In the interim, topographically related interference fringes can be eliminated using differential SAR interferometry. The DInSAR technology can achieve millimeter-level surface deformation precision when combined with other observational methods.

To detect ground surface displacement in the LOS direction, DInSAR uses phase information from multiple repeated LOS observations. Surface deformation mapping by InSAR is shown in Figure 2.6 in its configured state. It is expected that P is a ground target and P' is the same ground target after displacement. The slant range difference in the LOS direction is denoted by r.

The phase component resulting from deformation can be defined using equation 2.7 as follows:

$$\phi_{def} = \phi - \phi_{orb} - \phi_{topo} - \phi_{atm} - \phi_{noise}, \tag{2.14}$$

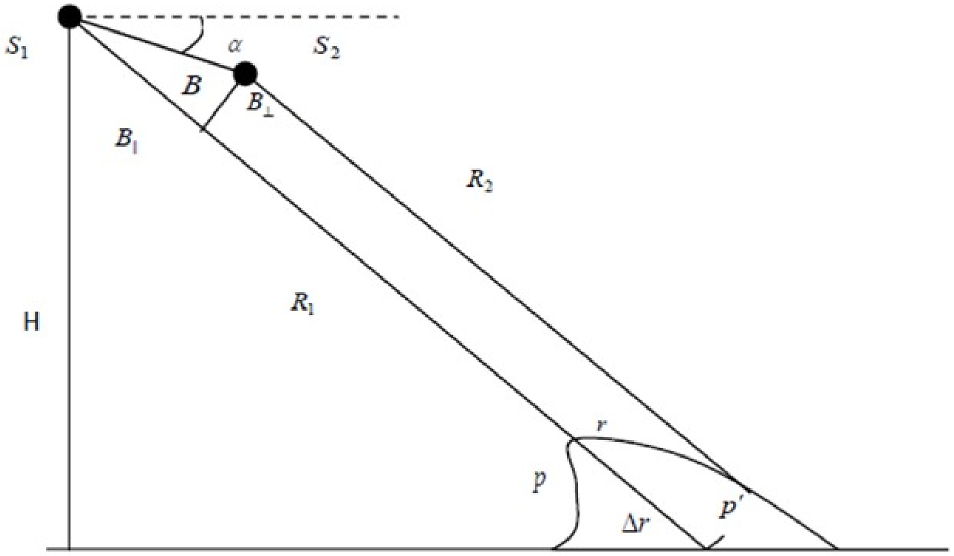

Figure 2.6: Configuration of surface deformation mapping using InSAR.

when combined with equation 2.6, the deformation measurement can be written as follows when displacement is in the LOS direction:

$$\Delta r = -\frac{\lambda(\phi - \phi_{orb} - \phi_{topo} - \phi_{atm} - \phi_{noise})}{4\pi} \tag{2.15}$$

DInSAR has been extensively applied in the field of landslide monitoring, seismic geological catastrophes, urban land subsidence, and other areas depending on the various types of surface deformation. The hypocentral location, focal mechanism, distribution of seismic slip, and other information can be proposed by performing interferometric processing with SAR complex images of pre-earthquake and post-earthquake obtained by satellite, providing trustworthy and valuable information for seismic research. After removing the atmospheric phase delay provided by GPS and MERIS, SAR interference images can obtain more precise surface deformation data, with an accuracy of up to a millimeter. It is possible to get urban ground deformation information with high temporal and high spatial resolution by combining the deformation result of DInSAR with standard settlement observation methods (e.g., GPS, leveling). This information can also be used to supply the necessary functions of government departments as a reference. To this end, numerous methods have been devised by various researchers. As a result, several DInSAR techniques have been developed, including the two-pass method [10], three-pass method [5, 11], and four-pass method.

All of the methods mentioned above require external data sources (e.g., DEM or an additional set of interferometric measurements) to effectively remove the topographic component from Equation2.15. One exception exists in the case of zero or near-zero spatial baseline [66].

2.3 Diffrential Interferometry (DInSAR)

DInSAR aims to separate the topographic and the displacement terms in an interferogram. The topographic phase must be eliminated to determine the displacement component. When a DEM is present, two-pass differential interferometry is used; otherwise, three- or four-pass differential interferometry is used. The methods for obtaining a differential interferogram vary depending on whether or not a DEM is available as well as whether or not a phase unwrapping procedure is necessary. The differential phase must be eliminated if the goal is to instead determine the topographic component. An effective baseline that is greater than the original baselines can be obtained by combining complex interferograms with scaling to eliminate phase noise.

2.3.1 Approaches of differential interferometry

2.3.1.1 Two-pass DInSAR

In the case of two-pass DInSAR, an interferogram is formed using a pair of SAR images that are mutually coherent. These images could be combined with a DEM. In addition, the interferometric image pairs can be acquired using the same sensor at different times or with another sensor with similar properties. Two types are involved. First, two-pass DInSAR without an external DEM to detect deformation or displacement signals in the interferogram. This approach assumes zero perpendicular baselines to significantly eliminate the topographic component of the interferometric phase [66]. Second, two-pass DInSAR with a DEM which is used to remove the topographic phase [10]. Zero baselines are unrealistic, therefore the second type is more commonly employed [66]. A DEM can be produced from Light Detection and Ranging (LiDAR), aerial photogrammetry, and online resources such as shuttle radar topography mission (SRTM). In DInSAR research, Massonnet et al. [10] were pioneers in using this technique to generate DInSAR for the Landers earthquake on 28^{th} June 1992. They have removed the topographic phase using a $15'$ DEM from the U.S. Geological Survey. Zebker et al. [11] summarized the shortcomings of this technique which include the global DEM coverage, accuracy concerns including errors and distortions in third-party or existing DEMs, challenges in SAR image to DEM registration, and difficulties in determining the phase relationship between random points in the scene. However, with the release of near-global coverage SRTM in various resolutions in 2000, most of these challenges have been mitigated, as DEM coverage has become more accessible for most sites on the Earth.

2.3.1.2 Three-pass DInSAR

The three-pass setup does not utilize an external DEM. Instead, three SAR images are employed in a mutually coherent manner. One image serves as the common master for the other two images [11]. One interferometric pair shouldn't be affected by ground deformation (i.e., deformation-free) among this triplet. Such a pair is then utilized to generate a DEM for topographic phase removal from the other pair (deformation pair). It is important to consider the perpendicular and temporal baselines of both pairs to maintain accurate results. For example, the typical temporal baseline of ERS SAR is one day while the perpendicular baseline ranges from 100 m to 300 m [66]. This approach was first introduced in Zebker et al. [11] where they produced a pair of interferograms based on ERS-1 data. They scaled down the second interferogram while one interferogram was used to eliminate the topographic phase to keep only the deformation phase. In comparison with the two-pass DInSAR, the DEM registration to the master image is simpler. The reason is that all SAR images are transformed into the coordinate frame of the master image. Moreover, third-party DEM is not required therefore it eliminates the requirement for azimuth-slant range SAR coordinate transformation of the DEM.

2.3.1.3 Four-pass DInSAR

The four-pass DInSAR and three-pass DInSAR are comparable. The two methods differ in both the number of SAR images employed and the selection of the master SAR images used in the two InSAR pairs. This technique makes use of up to four coherent SAR images. The topographic phase is calculated from two of the four images and then deduced from the interferogram created from the other pairs. A tandem pair, which is made up of two SAR images of the same area taken by the ERS-1/2 SAR systems one day apart, or images with a very short temporal baseline can be used to create a topographic pair. This approach is less flexible than the three-pass DInSAR because the external master SAR image required for co-registration differs from the master SAR image of the differential pair.

2.3.2 Limitations of conventional DInSAR

The accuracy of typical differential InSAR measurements is compromised by several uncertain elements, such as ocean tide loads (OTL), decorrelation, satellite orbital error, DEM inaccuracy, and decorrelation (in the coastal zone). The precision of interferometric deformation measurements will decrease due to these uncertainties, which will also cause phase noise and phase decorrelation. In rare cases, the phase unwrapping procedure may even fail. Phase decorrelation typically comprises six components [9, 19]: Doppler decorrelation caused by a variation in the Doppler centroid frequency; Temporal decorrelation caused by a change in scatterer characteristics on the ground surface; Spatial decorrelation caused by a difference in side-looking angle; Radar systematic noise causes thermal decorrelation, ground objects, particularly for ground coverage, produce scatterer decorrelation, and algorithm flaws cause decorrelation in the data process.

2.3.2.1 Spatial decorrelation

The length of the perpendicular baseline is connected to the interferometric quality since the fundamental idea behind InSAR is that the same scene is captured by interferometry from two different incidental angles. The correlation between the radar signal echoes of two images is high when the perpendicular baseline is minimal. Despite the long perpendicular baseline, there is little association between the echoes of the two images. The correlation of radar signal echoes and the phase signal to noise ratio (SNR) will both be extremely poor if the baseline length reaches a threshold value, which will prevent interferometry information from being extracted [19].

2.3.2.2 Temporal decorrelation

Once the interferometric image acquisition time difference exceeds a threshold point, temporal decorrelation typically happens. The backscattering mechanism on the terrain surface by different acquisition times will change randomly due to a variety of quantitative and non-quantitative factors, such as vegetation growth, farmland cultivation, and other anthropogenic events because the phase information records not only the slant range but also the characteristic and structure of the ground resolution cell. Loss of coherence and SNR are the outcomes of the phase contribution from these unforeseen events, which might even mask the true signal. In this case, phase unwrapping will be challenging since the interferometry's fringes will be confusing and discontinuous. Temporal decorrelation typically occurs in locations with dense vegetation, but in sparsely vegetated or desert regions, this negative effect will be less pronounced, especially in urban areas with a high density of hard targets. According to several research [9, 19], long wavelength interferometric systems can maintain temporal correlation more successfully than shorter wavelength systems. L-band satellite picture (23.5 cm wavelength) shows a greater temporal correlation than C-band satellite image (5.6 cm wavelength).

2.3.2.3 Atmospheric effect

One of the most important errors in InSAR measurements is the atmospheric effect, which frequently appears as a heterogeneous radar signal delay. Temperature, humidity, pressure, and water vapor are only a few of the variables that affect atmospheric delay. Whether in the time or spatial realms, these elements are distributed unevenly. Since the photographs were taken at various times, the air conditions were probably not the same. Additionally, the atmospheric conditions may vary even within the same region. RADAR transmissions from the satellite experience unexpected signal delays because of the non-identical and heterogenic air conditions that bend their routes. The signal delay introduces additional phase fringes into the interferogram and results in undesirable phase variation [18]. The accuracy of deformation measurements will be impacted by this phase distortion, which will also reduce the precision of the final results. In the case of a spatial baseline spanning from 100 to 400 meters, [18] found that a relative humility variation of 20 % results in deformation errors of 10 to 14 cm and topographic errors of 8 to 290 meters. According to [67], an extreme atmospheric delay in a coastal zone can cause an error in deformation of around 10 cm, severely restricting the use of the technology there. [68] presented an approach based on stacking several interferograms and smoothing the atmospheric effects to reduce the negative impact caused by atmospheric artifacts. However, this approach does not eliminate the artifacts; rather, it simply averages them into each interferogram.

2.3.2.4 Orbital error

In InSAR measurements, orbital error is frequently present since it is impossible to determine the sensor state vector with exact precision. There are three ways that orbital inaccuracy can negatively impact InSAR measurements: First, when the flat earth and topographic phase components from the interferometric phase are subtracted, inaccurate orbital data will lead to incorrect determination of the spatial baseline. Second, the reliability and precision of this method will be impacted by orbital data inaccuracies. Third, the application of geocoding will be negatively impacted by inaccurate orbital satellite ephemerides, which will result in mistakes in the transfer of radar coordinates into geographic coordinates. In small region processes, the error resulting from an erroneous sensor state vector is typically tolerable. However, the inaccuracy must be considered while working with a broad area. To estimate the phase residual owing to orbital error and rectify the phase information, ground control points can be used to derive topographic information. When extracting short wavelength deformation, the inaccuracy can be eliminated by a low-order polynomial concerning creating deformation maps. However, it is almost hard to distinguish between orbital error and long-wavelength deformation data.

2.4 Multi-temporal Interferometric Synthetic Aperture Radar (MT-InSAR)

The use of DInSAR for movement detection and monitoring is constrained by several issues (see, for example, [69]. The main restrictions rely on atmospheric disturbances and incoherent changes in target backscattering (coherence loss). These issues are reduced by identifying radar targets that generate a backscattered phase signal that can be measured over time and processing large temporal series of SAR data (about 15 radar pictures), known as multi-temporal interferometry (MTI) techniques.

Since 2000, numerous techniques for highly accurate long-term ground surface deformation signal detection have been created and successfully used to investigate a variety of geophysical phenomena [70, 71]. LOS displacement time series, mean LOS velocity (or equivalent LOS displacement), and improved elevation estimates are the results of MTI processing for each coherent target. These techniques use a long sequence of radar images that have been processed using various techniques that are mainly divided into two broad categories to solve the primary drawbacks of DInSAR (temporal/geometrical decorrelation, atmospheric artifacts):

1. PSI and related techniques [72, 73, 27, 69, 29, 74] rely on phase data from solitary, isolated objects that exhibit strong temporal phase stability. These methods typically involve computing differential interferograms for all acquisitions relative to a single reference image (master image) and then performing advanced phase analysis on the pixels that demonstrate a stable SAR response across the entire stack of images [75].
2. SBAS and related techniques leverage differential interferograms generated from image pairs with optimal spatial baseline values (i.e., below a specific threshold) to extract geographically distributed information. These methods obtain connected time series of phase values indicative of deformation by applying spatial filtering and employing various techniques, such as least mean squares (LMS) and singular value decomposition (SVD) [30, 31, 76].

2.4.1 Permanent Scatterer Interferometry

PSI, was introduced in 2000 by [77]. In contrast to the conventional DInSAR method, the new method concentrates on the permanent scatterer, which is more stable over time than the interferogram's other pixels. Additionally, the method has advanced significantly, enabling it to now not only track linear deformation but also nonlinear deformation. The monitoring area is also increased from the initial 5 square kilometers to that without any limitations. According to [77, 26], the PS approach can produce DEM data at the decimeter level on permanent scatterers and increase the monitoring accuracy of the deformation rate to the millimeter level. Since then, a lot of progress has been made in the application of the PS method to track surface deformation. A coherence coefficient-based technique for Permanent scatterer point recognition was proposed in 2001 by [78].

The seasonal ground deformation of San Jose in America was examined using PSI in 2003. According to the findings, the region's settlement time runs from April to August each year, and its elevating period runs from September to the following March. The variation range difference is roughly 2 cm [79]. German Space Agency (DLR) researchers employed the PSI approach in 2004 to track ground subsidence in Berlin, Germany [80]. Using the PSI method, it was possible to determine the surface deformation in Campania, southern Italy, between 1992 and 2001 in 2008. Recently, the SAR images used in the PSI approach have evolved from low-resolution images with low-resolution image processing to high-resolution images with X-band. Numerous academics have successively examined the X-band SAR data. For instance, 30 Terra SAR images were analyzed to track the Venetian coast's centuries-level deterioration [81]. Through the comparison analysis of Dossena in Italy, other researchers noted that PS points with high density generated from high-resolution images are more suitable for deformation monitoring in non-urban locations [82].

There are four steps to the PSI method: First, N differential interferograms are created for a chosen master image using a stack of N +1 co-registered and calibrated SAR images. To account for the topographic phase, a reference DEM is used. The master picture is chosen to minimize the baseline spread of the interferograms and maximize coherence (the master image often resides in the middle of the time series). The pixel's unwrapped phase in the K^th differential interferogram. Because the estimation is carried out in the complex domain in PSI, wrapped differential interferograms are utilized. Second, pixels with a single PS, or those with minimum phase dispersion for time, are chosen. There are two methods to accomplish this: The normalized amplitude dispersion index, which is derived by [26], is a useful indicator of the phase standard deviation at high SNR.

$$D_a = \frac{\sigma_a}{\mu_a} = \sigma_\phi, \tag{2.16}$$

where σ_a and μ_a represent the temporal mean and sample standard deviation of the amplitude time series a, respectively. Pixels are chosen as initial PS candidates if their normalized amplitude dispersion index is less than a certain threshold (about 0.25) Analyzing the signal-to-cluster ratio (SCR) of the pixels in the temporal mean image is another way to find PSs. If the clutter in the adjacent cells is assumed to be similar to those surrounding the dominant scatterer within a pixel, a spatial window is used to compute the clutter based on the pixel neighborhood. Adam et al. [83] provides the phase standard deviation of the PS as follows:

$$\sigma_\phi = \frac{1}{\sqrt{2 + SCR}} \tag{2.17}$$

Pixels that have an SCR greater than a specific threshold (about 2) are chosen as PSs. Third, to eliminate the atmospheric phase components from the interferograms, an initial estimation is carried out on the preliminary set of PS candidates. A reference network is created by connecting nearby PSs with arcs, and the network is given a reference point. Usually, only sites that are closer together than a predetermined distance are connected. Since the arcs are normally confined to 2-3 km, the effects of air propagation and orbital inaccuracies are not substantial enough to cause issues with phase unwrapping. Instead, phase differences between locations connected by the arcs are calculated directly [8]. In the K^{th} differential interferogram, the phase difference $\Delta\Phi^K_{diff_{model}}$ between two generic pixels connected by an arc in the reference network is represented by the following model:

$$\Delta\Phi^K_{diff_{model}} = \Delta\Phi^K_{def} + \Delta\Phi^K_{topo} = \frac{4\pi}{\lambda} B^t_K \Delta v + \frac{4\pi}{\lambda} \frac{B^K_\perp}{R_1 \sin\theta} \Delta h, \tag{2.18}$$

such that $K = 1, \ldots, N$ represents the index of the differential interferograms, while Δv and Δh denote the differential displacement velocity in the LOS and the differential DEM error between the two locations, respectively. To estimate the differential DEM error and differential velocity, the coherence function of the model is maximized as follows:

$$\xi(\Delta v, \Delta h) = \frac{1}{N} \left| \sum_{k=1}^{N} e^j (\Delta\Phi^K_{diff_{obs}} - \Delta\Phi^K_{diff_{model}}) \right| \tag{2.19}$$

For any pair of pixels, their phase difference is $\Delta\Phi^K_{diff_{obs}}$ in K^{th} differential interferogram. The differential velocity and differential DEM error influence the periodogram, which is a two-dimensional (2D) function. The available temporal baselines B_T^K and the available spatial baselines $B_\perp^K$ define an uneven grid over which its values are known. The peak of this periodogram is utilized to calculate the differential velocity and differential DEM error:

$$(\Delta\hat{v}, \Delta\hat{h}) = argmax(\xi) \tag{2.20}$$

It is worth noting that the term "temporal coherence," as used in some literature to describe the periodogram's maximum, is misleading. This term does not pertain to the temporal decorrelation phenomenon discussed earlier. Instead, it represents the degree to which the observed interferometric phase corresponds to the modeled interferometric phase. The reference pixel serves as a basis for estimating the velocities and DEM errors for each PS through a weighted least squares (LS) integration. Notably, a temporal coherence threshold is used to exclude the arcs with values less than the threshold. Also, other arcs are weighted based on these values. The chosen PS interferograms are then stripped of low-pass deformation and DEM error phase components. Atmospheric phase components are estimated for the initial PS candidates using low-pass spatial filtering followed by high-pass temporal filtering, given their high spatial but low temporal correlation. Atmospheric phase screen (APS) is created for each interferogram, and the initial data is removed from the APS. The remaining PS candidates are then selected, and residual DEM and deformation velocities are computed relative to the nearest PS in the reference network, similar to single arc estimation.

A temporal coherence threshold of approximately 0.75 is used, below which points are disregarded. After geocoding the PS locations, the deformation information is provided to end users. The effectiveness of the PS analysis depends on both the number of available images and the density of PS points, with an optimal density of approximately 5-10 PS/km^2 and a minimum requirement of around 25 images [79]. Before deformation estimation, a deformation model must be defined. While linear models are commonly used, non-linear models, such as seasonal models, are also applicable [77, 79].

Traditional PSI methods struggle to resolve multiple dominant scatterers within a single-resolution cell. However, recent PSI algorithms have proposed techniques to distinguish between double scatterers or multiple dominant scatterers at different elevations within the same cell [84]. PSI offers millimeter-level precision in deformation mapping. For example, Bamler et al. [85] investigated the rates of linear deformation projected for the Las Vegas area in the US, derived from 45 ERS-1/2 acquisitions between 1992 and 2000. This analysis utilized the DLR operational PSI module of the PSI-GENESIS generic system for InSAR [84, 86, 29], which also includes DInSAR processing. The processor's co-registration module employs a geometry-based approach using precise orbits and an SRTM DEM. Due to its lack of systematic errors, the PSI-GENESIS processing system is considered the standard for product validation by several PSI operational service providers [87].

2.4.2 Small Baseline Subset

A post-processing technique called the SBAS algorithm is employed to extract deformation parameters and DEM error from a series of multi-master short spatial baseline differential interferograms. This method is easier to implement compared to the PSI technique. However, one of the main sources of error in this approach is phase unwrapping errors, as the unwrapped phases serve as the initial input for the SBAS process. In this section, we will outline the core principles of the SBAS algorithm. The key steps in SBAS processing are as follows:

1. **Image Acquisition**: A set of $N+1$ co-registered SLC SAR images is obtained at times t_n, where $n = 0, ..., N$. It's assumed that each image can be successfully generated.

2. **Interferogram Selection**: A total of M interferograms are selected with low

spatial and temporal baselines, along with modest Doppler centroid differences, to minimize the decorrelation phenomenon. It's worth mentioning that the SAR data used to generate the interferograms may be divided into several small baseline subsets, which need to be accurately combined to reconstruct the deformation time series.

3. **Interferometric Signal Representation**: For a coherent pixel at coordinates (x, r), the interferometric signal in a generic interferogram K, created from SAR images recorded at times t_B and t_A, can be described as follows:

$$\begin{aligned} \delta\Phi_K = \Phi(t_B, x, r) - \Phi(t_A, x, r) = \frac{4\pi}{\lambda} \\ [d(t_B, x, r) - d(t_A, x, r)] + \Delta\Phi^t opo_K(x, r) + \\ \Delta Q\Phi^a tm_K(t_B, t_A, x, r) + \Delta n_j(x, r), \end{aligned} \tag{2.21}$$

Such that $K = 1, ..., M$ represents the index of the interferograms, and $d(t_B, x, r)$ and $d(t_A, x, r)$ are the cumulative deformations along the LOS at times t_B and t_A, respectively, concerning the first scene at time t_0. The phases obtained at times t_B and t_A are denoted as (t_B, x, r) and (t_A, x, r). In DInSAR interferograms, the residual topographic phase is represented by $\Delta\Phi^{topo}K(x, r)$. The phase differences caused by atmospheric dispersion at times t_B and t_A are denoted by $\Delta Q\Phi^{atm}K(t_B, t_A, x, r)$. The term $\Delta n_j(x, r)$ represents the phase component contributed by additional noise sources and potential decorrelation effects.

After the phase unwrapping stage, the low-pass deformation signal component and topographic error are computed for each coherent pixel using the LS solution. The low-pass deformation, often referred to as low pass (LP) deformation, can be modeled using a cubic model.

$$\begin{aligned} d(t_B, x, r) =& \overline{v} * (t_i - t_0) + \frac{1}{2}\overline{a} * (t_i - t_0)^2 + \\ & \frac{1}{6}\overline{\Delta a} * (t_i - t_0)^3, \end{aligned} \tag{2.22}$$

where $\overline{v}$, $\overline{a}$, and $\overline{\Delta a}$ are unknowable. Equation 2.21can be stated as a result as:

$$\delta\Phi_K = M_K P + \delta N_K, \tag{2.23}$$

where P is the parameter vector as stated in Equation 2.24 as follows:

$$P_T = [\overline{v}, \overline{a}, \Delta\overline{a}, \Delta z] \tag{2.24}$$

The design vector M, in Equation 2.23, contains the coefficients corresponding to the unknown parameters. Such parameters include the mean velocity, mean acceleration, variation in mean acceleration, and topographical error. These coefficients are used to model the relationship between the observed interferometric phase and the underlying physical quantities that we aim to estimate. By incorporating these coefficients into the design vector, we can solve for the unknown parameters using LS estimation, providing insights into the deformation and topographic characteristics of the observed area.

The non-modeled displacement, atmospheric signals, and other noise all add phase components to $\Delta N_j(x, r)$. The system of observations for a general coherent point can be expressed as follows when M interferograms are taken into account:

$$\delta\Phi = M \times P + \delta N, \tag{2.25}$$

where $\delta\Phi$ is the unwrapped and ramp-removed phase vector, M is an $M \times 4$ design matrix corresponding to the parameters in P, and δN is the non-modeled phase vector. Assuming $\delta\Phi$ behaves randomly in temporal space, Equation 2.25 can be solved under the framework of LS.

It is worth noting that the LP displacement model, whether represented by a cubic pattern or a linear model, is used exclusively in the SBAS approach for estimating the DEM error. This calculated LP displacement component is not considered in the subsequent displacement time series analysis. To simplify the phase unwrapping process, both the topographic error and the estimated LP phase component are removed from the wrapped input interferograms. By doing so, the fringe rate is significantly reduced, allowing the remaining phase to be more easily unwrapped. The unwrapped phase is then combined with the LP phase component to form the phase observations, which can be expressed as:

$$\begin{aligned} \Phi_K &= \sum_{k=1}^{M} \frac{4\pi}{\lambda}(t_K - t_{K-1})v_K + \delta N'_K \\ v_K &= \frac{\Phi_K - \Phi_{K-1}}{t_K - t_{K-1}}, \end{aligned} \tag{2.26}$$

where v_K denotes the average velocity of motion between time-adjacent acquisitions and delta N'_K denotes the phase affected by ambient noise and artifacts. In light of this, a set of M equations with N unknowns can be arranged as $\Phi = BV + \delta N'$, where the unknown vector V is represented by an $MtimesN$ matrix called B. Once more, LSs can be used to resolve the parameters corresponding to the velocities. Since matrix $\mathbf{B}$ indicates the total time between each interferometric pair and depends on the combination of SLC pictures for interferograms, it, unfortunately, runs the risk of being rank deficient at this point. The pseudo-inverse of $\mathbf{B}$, which may be determined using SVD, is utilized to solve this issue [30]. According to the speeds and time intervals, one can immediately achieve the displacement time series. It is important to emphasize that the assumption of atmospheric artifacts and decorrelation noise following a Gaussian distribution in the temporal domain is not always accurate in practice. Consequently, additional processing is often required to account for these discrepancies, as the estimated displacement time series may contain potential atmospheric inaccuracies.

The SBAS technique focuses on scattered scatterers (without dominant elements within the resolution cell), which are more susceptible to both temporal and volume decorrelation than PSI, which is optimized for resolution cells dominated by a single scatterer. Due to these characteristics, significant variations in the quantity and spatial distribution of measurable targets can occur, depending on the scattering properties of the ground [88].

Additionally, new enhanced processing techniques have recently been introduced to effectively merge PSI and SBAS methodologies, allowing for the study of both isolated and distributed targets [35, 41]. In practice, reducing the distance between nearby targets decreases the likelihood of phase aliasing, thus improving processing robustness [75]. The development of MTI is ongoing, and several methods have been proposed to enhance processing reliability through revised three-dimensional (3D) phase unwrapping algorithms [89, 71, 90].

2.5 Multi-Track/Multi-Satellite InSAR Methodologies

Large archives of SAR data are increasingly becoming available, collected by numerous RADAR sensors on space-borne platforms operating at various wavelengths, unique angle geometries, and possibly through different acquisition modes. This raises the challenge of how to successfully merge the complementary information embedded in these various SAR datasets. Integrating multi-platform (multi-sensor) LOS displacement time series is particularly valuable, as it enhances the ability to retrieve the 3D components of measured surface displacement, namely east-west (E-W), north-south (N-S), and up-down (U-D). This approach addresses the primary limitation of DInSAR, which is its ability to measure only the satellite LOS projection of the displacement. Several approaches have been developed to combine multiple-orbit/multiple-angle DInSAR-based measurements and integrate DInSAR data products with other external information [50, 47, 48, 91, 92, 93, 49, 94, 95, 96].

Let's examine the combination of InSAR data from two satellites, one on an ascending orbit and the other on a descending orbit, with side-looking angles of θ_1 and θ_2, respectively as shown in Figure 2.7. For simplicity, the N-S deformation components have been minimized. This is because the limited diversity in viewing geometries makes it challenging to accurately detect N-S displacements, as nearly all contemporary space-based satellites operate in nearly polar orbits, with the azimuthal direction of the satellite being approximately parallel to the N-S axis.

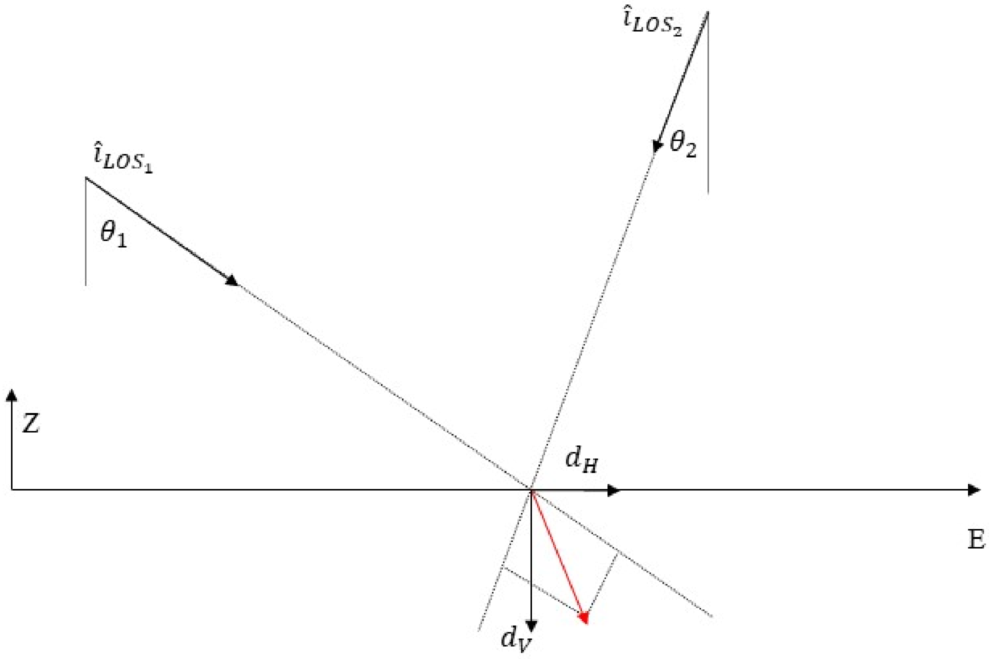

Figure 2.7: Multi-angle InSAR observations.

According to Pepe [97], the following equations can be used to relate the LOS components of the deformation d to the E-W, namely d_H, and U-D, namely d_V, components:

$$d_{LOS_1} = \mathbf{d}.\hat{\mathbf{i}}_{LOS_1} = d_H \sin\theta_1 + d_V \cos\theta_1 \tag{2.27}$$

$$d_{LOS_2} = \mathbf{d}.\hat{\mathbf{i}}_{LOS_2} = -d_H \sin\theta_2 + d_V \cos\theta_2 \tag{2.28}$$

Matrix formalism allows for the following expression of the system of Equations 2.27, 2.27:

$$\begin{pmatrix} \sin\theta_1 & \cos\theta_1 \\ -\sin\theta_2 & \cos\theta_2 \end{pmatrix} \cdot \begin{pmatrix} d_H \\ d_V \end{pmatrix} = \begin{pmatrix} d_{LOS_1} \\ d_{LOS_2} \end{pmatrix} \tag{2.29}$$

In this streamlined scenario, the following is a formal way to reach a straight solution:

$$\begin{pmatrix} d_H \\ d_V \end{pmatrix} = \begin{pmatrix} \sin\theta_1 & \cos\theta_1 \\ -\sin\theta_2 & \cos\theta_2 \end{pmatrix}^{-1} \cdot \begin{pmatrix} d_{LOS_1} \\ d_{LOS_2} \end{pmatrix} = \begin{pmatrix} d_{LOS_1}\cos\theta_2 - d_{LOS_2}\cos\theta_1 \\ d_{LOS_1}\sin\theta_2 + d_{LOS_2}\sin\theta_1 \end{pmatrix} / \sin(\theta_1+\theta_2) \tag{2.30}$$

The effects of the combination specifically manifest as follows in the more straightforward scenario where ascending and descending SAR data are obtained from the satellite with the same side-looking angle:

$$\begin{pmatrix} d_H \\ d_V \end{pmatrix} = \begin{pmatrix} d_{LOS_1}\cos\theta_2 - d_{LOS_2}\cos\theta_1 \\ d_{LOS_1}\sin\theta_2 + d_{LOS_2}\sin\theta_1 \end{pmatrix} / \sin(2\theta) = \begin{pmatrix} \frac{d_{LOS_1}-d_{LOS_2}}{2\sin\theta} \\ \frac{d_{LOS_1}+d_{LOS_2}}{2\cos\theta} \end{pmatrix} \tag{2.31}$$

The E-W deformation component can be derived from the difference between measurements taken from ascending and descending orbits, while the vertical displacement is obtained by summing these LOS deformation readings. This technique is useful for combining deformation rates from both orbit types, offering a more complete view of surface movement. However, integrating deformation time series poses challenges because ascending and descending orbits seldom cover the same area at the same time. To address this, one approach involves interpolating LOS time series from both orbit types across the entire period. Despite its potential, this interpolation method often suffers from lower accuracy due to various sources of errors including atmospheric, orbital, thermal, and interpolation noise.

The challenge of integrating multi-track InSAR data has been tackled in several ways in the literature. Wright [50] was among the first to address this problem on a global scale, focusing on how to recover 3D displacements from a mix of ascending/descending and right/left-looking SAR acquisitions. For instance, Wright's study combined five RADARSAT-1 interferograms from four right-looking ascending and descending passes to recover the U-D and E-W deformation fields caused by the October 23, 2002, Nenana Mountain earthquake in Alaska. The study deliberately omitted the N-S deformation, considering it to be relatively minor. However, accurately capturing the N-S components is essential, as spacecraft typically follow N-S-oriented orbits.

To estimate the full 3D motions of the Henrietta Nesmith Glacier, Gray [47] combined LOS displacements from the extra-low and extra-high beams of the RADARSAT-2 sensor. This approach addressed the challenge of capturing N-S displacements. Similarly, [48, 91] combined LOS displacements with GPS measurements to infer complete 3D deformation components.

Pixel offset (PO) tracking methods have also been employed to overcome the limited sensitivity of LOS measurements to N-S displacements. For example, [92, 93] used a combination of ascending and descending interferograms along with azimuth pixel offset (AZPO) observations to determine 3D co-seismic displacements for the 1999 Hector Mine and 2001 Bam earthquakes. This technique can achieve precision better than 10 cm [98, 99], with azimuth offsets predicted to a fraction of the pixel spacing (e.g., 1/30th).

While PO methods have largely been used for analyzing individual deformation events, efforts are to extend these techniques to develop 3D displacement time series. One notable example is the pixel-offset SBAS (PO-SBAS) approach [99]. This method examines the amplitudes of the selected image pairs to determine relative across-track and along-track phase offsets. Then it applies SVD to invert these values and retrieve the displacement time series. The PO-SBAS technique has successfully analyzed the temporal evolution of significant or rapidly changing surface deformation phenomena, achieving accuracy on the order of 10–12 cm, as demonstrated in experiments with ENVISAT images over Sierra Negra Caldera.

The central concept of Casu and Manconi [100] is to integrate the PO-SBAS time series, which directly measures the deformation in the azimuth direction (approximately parallel to N-S) and the LOS direction, taking into account orbital flight characteristics. The integration is conducted by treating ascending and descending acquisitions as if they were obtained simultaneously, assuming they are as close in time as possible, to address the challenge of non-coeval orbits. Methods to address this restriction can be found in [97, 101, 52, 54]. For example, the PO-SBAS, GPS, and InSAR-based data have been combined using the MinA technique within a single framework. The method described in Ozawa and Ueda [101] produces high spatiotemporal resolution maps of the combined LOS displacement field by integrating overlapping segments of SAR images recorded at adjacent tracks. Similar techniques have integrated multi-track interferograms from different SAR sensors and orbital positions [52, 54], resulting in time series of the U-D and E-W displacements. These methods assume minimal N-S deformation such that they maintain the temporally variable components of deformation.

For instance, the MSBAS technique described in [52] involves simultaneously generating multiple-satellite DInSAR interferograms and analyzing them. These interferograms are jointly inverted to extract 2D (U-D and E-W) surface deformation time series across a geocoded grid shared by all accessible SAR data tracks. This method links the 2D deformation components to the LOS displacements applicable to all available unwrapped interferograms and is inverted using the LS approach, seeking a minimum-norm velocity solution with Tikhonov regularization [54]. The MQQA approach was used by [55] to integrate time-overlapped multi-satellite DInSAR deformation time series over the Eastern coast of Shanghai, analyzing nearly 12 years of SAR data to produce long-term displacement time series for the ocean-reclaimed lands of the Shanghai megacity. Additionally, the Multidimensional Time Series (MasTer) toolbox [56], which is an automatic, unsupervised processing chain based on MSBAS, was proposed by[57, 52, 58].

2.6 Machine Learning and InSAR

The increasing availability of SAR data from various satellites has expanded InSAR's applications but also introduced challenges such as phase noise, atmospheric disturbances, and data integration complexities [102]. Machine learning ML has emerged as a powerful tool to address these challenges, improving the efficiency and accuracy of InSAR data processing. For example, [103] applied unsupervised learning techniques to mine InSAR displacement time series, enabling efficient analysis of large data sets. Similarly, [104] used convolutional neural networks convolutional neural networks (CNNs) to classify volcanic deformation in routinely generated InSAR data, improving the detection of volcanic disturbance. Deep learning models have also been developed to detect change points in InSAR time series, facilitating the timely identification of ground deformation events [105]. Other studies have focused on ML-based integration of multi-temporal InSAR data for landslide susceptibility mapping [106] and deep learning-accelerated pixel selection for time-series SAR interferometry [107]. Advanced ML algorithms, such as vision transformers, have been explored for detecting volcanic unrest in synthetic InSAR datasets [108]. Furthermore, ML-based approaches have been employed to forecast reservoir pressure variations in carbon storage sites using InSAR displacement data [109]. These advancements highlight ML's potential in automating complex InSAR analyses, improving noise reduction, phase unwrapping, and predictive modeling, thereby providing deeper insights into Earth's dynamic processes [15]. As next-generation SAR sensors with increased temporal resolution, such as geosynchronous SAR systems, become available, ML is expected to play an even greater role in integrating multi-satellite SAR data for disaster prevention and post-emergency response [102].

In this chapter, the fundamental concepts of SAR, InSAR, DInSAR, MT-InSAR, the application of ML in InSAR field and previous studies that have combined SAR data from different radar sensors were reviewed. The limitations of current methods for mapping deformation using multisatellite SAR data can be summarized as follows:

1. **Differences in Radar Wavelengths and Frequencies**: Various SAR satellites operate at different frequencies (e.g., X-band, C-band, L-band), leading to different sensitivities to surface deformation, penetration depths, and coherence

levels. Integrating displacement results from different wavelengths can be challenging due to the varying phase responses of different radar signals [19, 110].

2. **Temporal and Spatial Decorrelation**: The time gaps between SAR acquisitions from different satellites can cause decorrelation, especially in vegetated and dynamic urban areas. Temporal decorrelation reduces the coherence of interferograms, making it difficult to track long-term displacement accurately [8, 66].

3. **Differences in Imaging Geometry and Viewing Angles**: SAR satellites have different orbital parameters and imaging geometries, leading to variations in the line-of-sight LOS displacement measurements. The integration process requires careful geolocation corrections and LOS-to-vertical displacement transformations [27, 111].

4. **Atmospheric and Orbital Errors**:Atmospheric disturbances, such as tropospheric delays, can vary across SAR acquisitions from different satellites. Additionally, orbital inaccuracies introduce biases in displacement measurements, which require sophisticated correction techniques [20, 112].

5. **Time-Gap Between Different SAR Acquisitions**:Multi-satellite SAR data often have non-overlapping acquisition periods, making it difficult to construct continuous deformation time series. Time-dependent deformation models are often required, but they may introduce boundary non-convergence issues and inaccuracies [113].

6. **Cross-Sensor Biases**:Differences in radar sensor characteristics, including noise levels, incidence angles, and calibration procedures, introduce biases when integrating displacement measurements. These biases must be estimated and compensated for in the integration process [114, 115].

7. **Computational Complexity and Data Volume**:processing large archives

of SAR images and interferograms from multiple satellites requires significant computational resources and storage. High-performance computing and cloud-based solutions are often necessary for efficient processing [89, 29].

8. **Inconsistencies in Phase Unwrapping**:Phase unwrapping errors can propagate when integrating multiple SAR datasets, particularly when combining data from different sensors with varying noise levels and coherence. These inconsistencies can lead to inaccuracies in displacement measurements [116, 117].
9. **Weighting and Fusion Strategies**: determining the optimal weighting of displacement data from different satellites based on reliability factors, such as coherence, temporal baselines, and noise levels, remains a challenge. Various fusion strategies have been proposed, including machine learning approaches, but there is no universally accepted method [106, 118].

By addressing these challenges, this research aims to develop robust methods for integrating multi-satellite SAR data, improving the accuracy and reliability of long-term earth surface displacement monitoring. The following chapters aim to address these challenges.

Chapter 3

Research Strategy

This chapter outlines the comprehensive research workflow employed in the two case studies of this research. The core objective is to integrate multi-satellite, time-gapped, and time-overlapped SAR images to generate long-term vertical displacement maps in areas primarily affected by vertical movement.

In the first case study, the Modified Multi-Satellite SBAS MMSBAS algorithm was introduced as an adaptation of the traditional SBAS method by [30] for the integration of multimodal InSAR data sets.ta sets. The algorithm selects only high-coherence image pairs based on perpendicular and temporal baseline thresholds, applies the DInSAR technique, and performs inversion at high-coherence points identified through both Permanent Scatterers PS and Distributed scatterers DS measurements.

In the second case study, a Machine-Learning fusion approach was employed to generate combined vertical displacement maps by integrating vertical displacements from multiple SAR datasets. This method enables the monitoring of land subsidence for more than two decades. This method follows a similar workflow, prioritizing high-coherence image pairs before applying DInSAR and performing the integration on high-coherence points.

3.1 General Framework

Figure 3.1 presents the comprehensive research workflow, which consists of three main components:

1. **Multi-Baseline DInSAR Processing** : High-coherence (M) image pairs are selected based on specific spatial and temporal baseline thresholds. The traditional DInSAR is then applied to each pair, generating M line-of-sight LOS displacement maps, which are subsequently converted into vertical displacement maps.
2. **Selection of High-Coherence Common Points**: Integration is performed at selected high-coherence points, identified based on both Permanent Scatterers (PS) and Distributed Scatterers (DS) measurements.
3. **Integration Techniques**: Two approaches are used for integration:
   - Modified SBAS Method: An adaptation of the traditional SBAS approach for multimodal SAR datasets, producing vertical time-series velocity maps and a long-term mean vertical displacement velocity map of the study area.
   - Machine Learning-Based Integration: A Support Vector Regression (SVR) method that combines multiple independent variables, generating M integrated vertical velocity maps and a long-term mean vertical displacement velocity map.

3.1.1 Surface Displacement Using Multi-baseline DInSAR

The multi-baseline DInSAR technique has utilized the selected SAR image pairs based on short temporal and spatial baselines. Accordingly, temporal and spatial phase decorrelation has been minimized, and the phase quality of the processing pixels has been improved. The multi-baseline DInSAR processing chain has included several steps for each selected high-coherence image pair as follow:

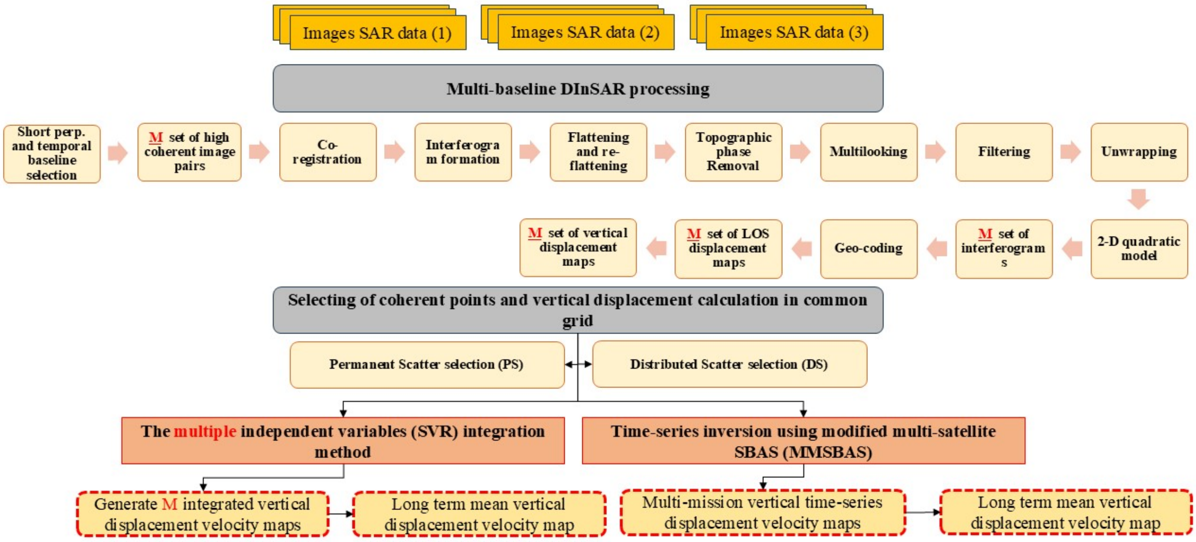

Figure 3.1: Research Flowchart.

1. **Co-Registration**: Co-registration is the process of aligning multiple SAR images to ensure pixel-to-pixel correspondence. Since SAR images are acquired at different times and under varying conditions, precise alignment is necessary to ensure accurate phase comparison. Misregistration errors can lead to phase inconsistencies and degraded interferometric results [110].

2. **Interferogram Generation**: An interferogram is generated by computing the phase difference between two co-registered SAR images. This phase difference contains contributions from:

   - Topography (terrain elevation).
   - Surface displacement (ground movement between the two acquisition times).
   - Atmospheric effects (signal delay due to variations in water vapor and ionospheric disturbances).
   - Orbital errors (differences in satellite positions).

   The raw interferogram consists of fringes that indicate phase variations, and these need further processing to extract meaningful displacement information

[9].

3. **Topographic Phase Removal**: To isolate surface displacement, the topographic phase contribution is removed using a Digital Elevation Model DEM, such as SRTM (Shuttle Radar Topography Mission) or TanDEM-X (TanDEM-X) DEM. If the DEM is not highly accurate, residual phase errors may remain, affecting displacement accuracy [19].

4. **Multi-Looking (Speckle Reduction and Noise Mitigation)**: Multi-looking is applied to reduce speckle noise and improve phase estimation by averaging neighboring pixels in the interferogram. This step enhances signal coherence but reduces spatial resolution [66].

5. **Phase Unwrapping**: Since SAR phase measurements are recorded within a $-\pi$ to $+\pi$ radians, discontinuities arise when deformation causes phase shifts beyond this range. Phase unwrapping is applied to recover the true, continuous phase values corresponding to absolute displacement measurements. Common unwrapping methods include:

    - Branch-cut algorithms.
    - Minimum-cost flow algorithms.
    - Least-squares techniques [119].

    Errors in this step can lead to incorrect displacement estimations, particularly in areas with low coherence or rapid deformation [28].

6. **Atmospheric and Noise Mitigation**: SAR signals are affected by atmospheric conditions such as water vapor content, which introduces delays in signal propagation. These atmospheric phase artifacts can be corrected using:

    - Spatial filtering techniques (e.g., high-pass filtering to remove large-scale atmospheric distortions).

  - Temporal filtering techniques (e.g., stacking multiple interferograms to reduce random noise).
  - External meteorological data assimilation to estimate atmospheric contributions [20].

   In addition, temporal and spatial decorrelation—which occurs due to changes in land cover, vegetation, or sensor geometries—can reduce coherence, making phase interpretation more challenging [8].

7. **Ground Displacement Calculation**: Once unwanted phase components are minimized, the remaining phase values correspond to surface displacement along the Line-of-Sight LOS direction. Displacement maps are generated by converting these phase differences into metric units (millimeters or centimeters). Depending on the satellite's incidence angle, LOS measurements may need to be decomposed into vertical and horizontal displacement components [111].

8. **Geocoding**: The displacement maps generated from SAR imagery are initially in radar coordinates. Geocoding converts these results into geographic coordinates (latitude, longitude, and elevation) using orbital parameters and DEMs. This step is essential for integrating DInSAR results with Geographic Information System (GIS) applications and other remote sensing datasets [113].

3.1.2 Selection of high Coherent Points

To integrate multi-satellite displacement, it was crucial to retrieve a significant number of high-coherence points. To this target, both PS and DS measurements were fundamentally utilized [120]. In the case of PS, temporal amplitude stability approximated the phase stability based on the Amplitude Dispersion Index $D_A = \frac{\sigma_A}{\mu_A}$ where the σ_A and μ_A were the mean and standard deviation of the amplitudes for a specific pixel, respectively. Initial consideration for PS candidates was given to pixels with $D_A < 0.4$. Unlike PS, DS preserved a moderate level of coherence during one or more

SAR acquisition periods. The value of complex coherence at a specific pixel in an interferometric pair was calculated as follows:

$$\tau^{m,n} = \frac{\sum_{t=1}^{L} s^m(t)s^n(t)}{\sqrt{\sum_{t=1}^{L}|s^m(t)|^2 \sum_{t=1}^{L}|s^n(t)|^2}} = \gamma^{m,n}e^{i\phi^{m,n}}, \tag{3.1}$$

where L represents the number of statistically homogeneous pixels (SHPs) around the central pixel, $s^m(t)$ and $s^n(t)$ denote the complex phase values of the SAR image pair, $\gamma^{m,n}$ indicates the degree of coherence, and $\phi^{m,n}$ denotes the spatially averaged interferometric phase.

To determine the SHPs for the central pixel, statistical similarity tests based on time series amplitudes, such as the Kolmogorov-Smirnov (KS) and Anderson-Darlington (AD) tests, are employed. Initially, DS candidates are selected from points with an average temporal coherence greater than 0.5 and more than 20 SHP. The spatially averaged phases then replace the original phases of a subset of DS locations. DS points coinciding with PS points are excluded to preserve the phases of individual PSs. It is important to note that PS coherence is always one in every interferogram. The selected PSs and DSs are then integrated for joint processing in the subsequent analysis. The unwrapped phase $d\phi$ is converted into displacements d_{los} at the chosen coherence points, given the wavelength λ, using the following well-known equation:

$$d_{los} = \frac{\lambda.d\phi}{4\pi} \tag{3.2}$$

At each selected high-coherence point, the vertical component of displacement d_u was determined using Equation (3.3), based on the incidence angle θ as follows:

$$d_u = \frac{d_{los}}{cos\theta} \tag{3.3}$$

The vertical displacement values from the interferograms were geocoded to create a common grid of high-coherence points, on which the multi-satellite SBAS integration step was applied.

3.1.3 Multi-Satellite SAR Data Integration

The multi-satellite SAR data integration was conducted using two approaches: an adapted SBAS method MMSBAS and a machine learning-based integration using multiple independent variables SVR.

3.1.3.1 Modified multi-satellite SBAS integration MMSBAS

To adapt traditional SBAS for multi-satellite SAR data integration, let $\boldsymbol{M}$ be the number of interferograms formed by $\boldsymbol{N}+1$ multi-satellite SAR images spanning the period from t_o to t_N, where t_o is the reference starting date. Consequently, the vertical displacement time series was reconstructed according to [30] as follows:

$$\boldsymbol{A}\boldsymbol{V}_u = \boldsymbol{d}_u, \tag{3.4}$$

where $\boldsymbol{A}^{\boldsymbol{M}\times\boldsymbol{N}}$ is an incidence matrix constructed using the time intervals between successive SAR images, while ${d_u}^{\boldsymbol{M}\times 1}$ is the vector of vertical displacements. Additionally, ${\boldsymbol{V_u}}^{\boldsymbol{N}\times 1}$ represents the unknown vertical velocity time series.

Since this system of equations was under-determined and did not yield a unique solution, it exemplifies a linear discrete ill-posed problem. To address this, replacing the "original" linear system with a nearby system—less sensitive to perturbations of the right-hand side—can provide a meaningful solution [121]. This process, known as regularization, is achieved using TSVD [122], as outlined in Equation (3.5), where $\boldsymbol{A}$ is decomposed into three matrices $\boldsymbol{U}$, $\boldsymbol{S}$, and $\boldsymbol{V}$.

$$\boldsymbol{A} = \boldsymbol{U}\ \boldsymbol{S}\ \boldsymbol{V}^T, \tag{3.5}$$

where $\boldsymbol{U}$ and $\boldsymbol{V}$ are orthogonal, and $\boldsymbol{S}$ was a diagonal matrix formed using Equation (3.6) where r was the rank of $\boldsymbol{A}$.

$$S =\ diag(\sigma_1, \sigma_2, \ldots, \sigma_n),\ \sigma_1 > \sigma_2 > \ldots > \sigma_r > \sigma_{r+1} = \sigma_{r+2} = ... = \sigma_n = 0 \tag{3.6}$$

The main principle of truncated singular value decomposition (TSVD) and standard form regularization is to convert an ill-posed problem into a well-posed one. In the case of TSVD, this involves approximating the matrix $\boldsymbol{A}$ with a lower-rank matrix $\boldsymbol{A}_K$ of rank k, while disregarding components of the right-hand side that correspond to the omitted components of $\boldsymbol{A}$. The matrix $\boldsymbol{A}_K$ used in TSVD is the rank-k matrix.

$$\boldsymbol{A}_K = \boldsymbol{U}\ \boldsymbol{S}_K\ \boldsymbol{V}^T,\ S_K =\ diag(\sigma_1, \ldots, \sigma_k, \ldots, 0, 0), \tag{3.7}$$

where, $k < r$ and S_k equal S with the smallest $n-k$ singular values replaced by zeros. The solution of Equation (3.4) based on TSVD is defined by:

$$\boldsymbol{V_u} = \boldsymbol{A}_k^+ \boldsymbol{d_u}, \tag{3.8}$$

The matrix $\boldsymbol{A}_k^+$ is the pseudoinverse of $\boldsymbol{A}_K$:

$$\boldsymbol{A}_K^+ = \boldsymbol{V}\ \boldsymbol{S}_K^+\ \boldsymbol{U}^T, \tag{3.9}$$

According to the TSVD, we obtain $\boldsymbol{V_u} = [V_u^1,\ V_u^2, \ldots,\ V_u^N]$ with respect to t_0. The TSVD method estimates the unknown parameters V_u for each pixel, and numerical integration reconstructs the displacement time series from the computed displacement velocities. Through this approach, we derived a combined multi-satellite surface displacement time series, aligned with the initial acquisition date.

3.1.3.2 Multi-satellite SAR-ML based merging algorithm

SVR performed effectively in estimating real functions with great generalization and high predictive accuracy [123]. Consequently, SVR has been adapted for multi-band vertical displacement integration.

SVR is a machine learning algorithm that is an extension of support vector machine (SVM) for regression analysis. When given an input value, SVR searches for a function that can predict the continuous output value most accurately. SVR architecture is similar to artificial neural networks as shown in Figure 3.2. Input and output layers are connected by a hidden layer that is self-computed using the input data. SVR maps the feature vectors of sample data into high-dimensional space, and the regression is employed based on the kernel function as depicted in Figure 3.3.

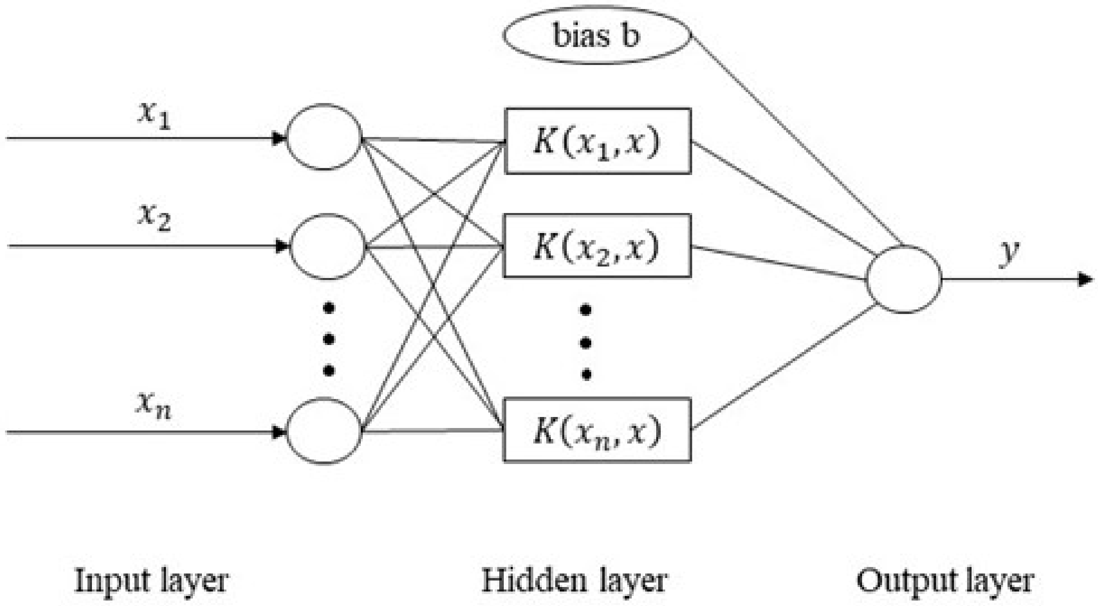

Figure 3.2: SVR structure.

Let $f(x) = \omega \times x + b$ be a SVR function that is defined by a coefficient ω, the input feature vector x; and the bias constant b therefore, The optimal regression function is determined by minimizing the following function [124]:

$$min\frac{1}{2}\omega^T\omega + c\frac{1}{N}\sum_{i=1}^{N} L(f(x_i), y_i) \tag{3.10}$$

$$L(y) = \begin{cases} 0, & \text{if } \ |f(x_i) - y_i| \ < \ \epsilon \\ |f(x_i) - y_i| - \epsilon, & \text{if } \ |f(x_i) - y_i| \ > \ \epsilon, \end{cases} \tag{3.11}$$

where c is the penalty factor, N is the sample's number, $f(x_i)$ is the predicted value of the i^{th} feature vector, y_i is the true value of i^{th} feature vector, L is the linear insensitive loss function, and ϵ is the maximum deviation. The Lagrange equation and the Karush-Kuhu-Tucker condition are employed to derive the dual mode of the SVR model and calculate the partial derivatives of the parameters [125]. The final decision function is:

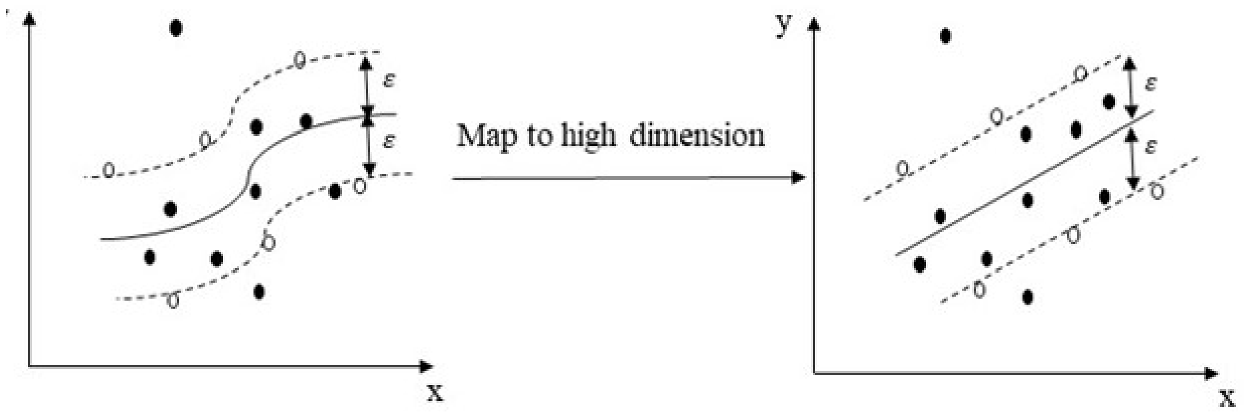

Figure 3.3: Schematic diagram of the kernel trick.

$$f(x) = \sum_{i=1}^{l} (\alpha_i^* - \alpha_i) K(x_i, x) + b, \tag{3.12}$$

such that l represents the number of SVR machines; α_i is the optimum solution; K represents the kernel function in the nonlinear regression, $K(x_i, x) = \Phi(x_i) * \Phi(x_j)$. To effectively manage the issue of dimensional explosion in high-dimensional spaces, a suitable kernel function is selected, and computations are performed in a lower-dimensional space. The radial basis function (RBF) kernel was utilized due to its excellent performance in nonlinear regression tasks. The RBF kernel is highly flexible and is based on the kernel function coefficientγ:

$$k(x_i, x_j) = exp(-\gamma |x_i - x_j|^2), \gamma > 0 \tag{3.13}$$

This chapter utilized multiple independent variables SVR which is an adaptation of those implemented in Scikit-learn python library[126] to integrate three sets of time-overlapped TSX, CSK, and S1 DInSAR vertical displacement over common high-coherent points. The response parameter $y = d_u^1, d_u^2, ..., d_u^m$ is the geocoded vertical ground displacement determined regarding a specific point from high-coherent points. The training set $x = (C^1, T^1), (C^2, T^2), ..., (C^m, T^m)$ is the combined vector of all the two input process parameters (coherence value at each point in each interferogram (C), and period (T) of each interferogram (in days)). SVR employs m sets of input-output pairings and the training procedure was carried out to obtain the ideal parameters. A combined multi-band displacement is then obtained using these parameters.

Chapter 4

Application of the Methodology: Case Studies, Results and Analysis

This chapter presents the case studies used to apply and validate the proposed methodology for integrating multi-satellite SAR datasets in long-term ground displacement monitoring. These case studies demonstrate the effectiveness of the approach in real-world scenarios and provide insights into its accuracy and limitations.

4.1 Improved Multi-Satellite SBAS For Retrieving Long-term Ground Displacement Time Series

This method has been applied to study long-term ground deformation in Almokattam City, Cairo, Egypt. Using SAR data from different sensors ERS, ENVISAT ASAR, and S1A, displacement time series from 2000 to 2020 were generated. The analysis revealed significant vertical deformation in the western area of Almokattam City, with a mean deformation velocity of -2.32 mm/year. Cross-validation results showed that the RMSE did not exceed 2.8 mm/year. These results are consistent with previous studies in the area. Thus, the proposed integration method shows great promise for generating displacement time series from multi-satellite SAR data, though it requires further validation with field measurements.

4.1.1 Materials

4.1.1.1 Study Area

Almokattam City, situated in the Arab Republic of Egypt, serves as the study area for this research, as depicted in Figure 4.1a. The city is located on the upper plateau of the Almokattam mountain in eastern Cairo. This plateau-like area covers an approximate surface area of 14 km^2. Elevations range from 60 m above mean sea level to approximately 140 m to the east. The city's layers are convex near the immediate vicinity, with heights rising to around 240 m near the castle and then decreasing northwards, ending at the Mountain of Al Amir near Abbasiyah. Over the past decade, Almokattam City has experienced significant urbanization, as shown in Figure 4.1b–d. Despite frequent collapses in areas such as Zbaleen, the southwestern scarp of the high plateau, and Manshiat Nasser, the city has continued to grow in population. As a result, the rocks in Almokattam City exhibit instability and are continually at risk of potential collapses [127, 128, 129].

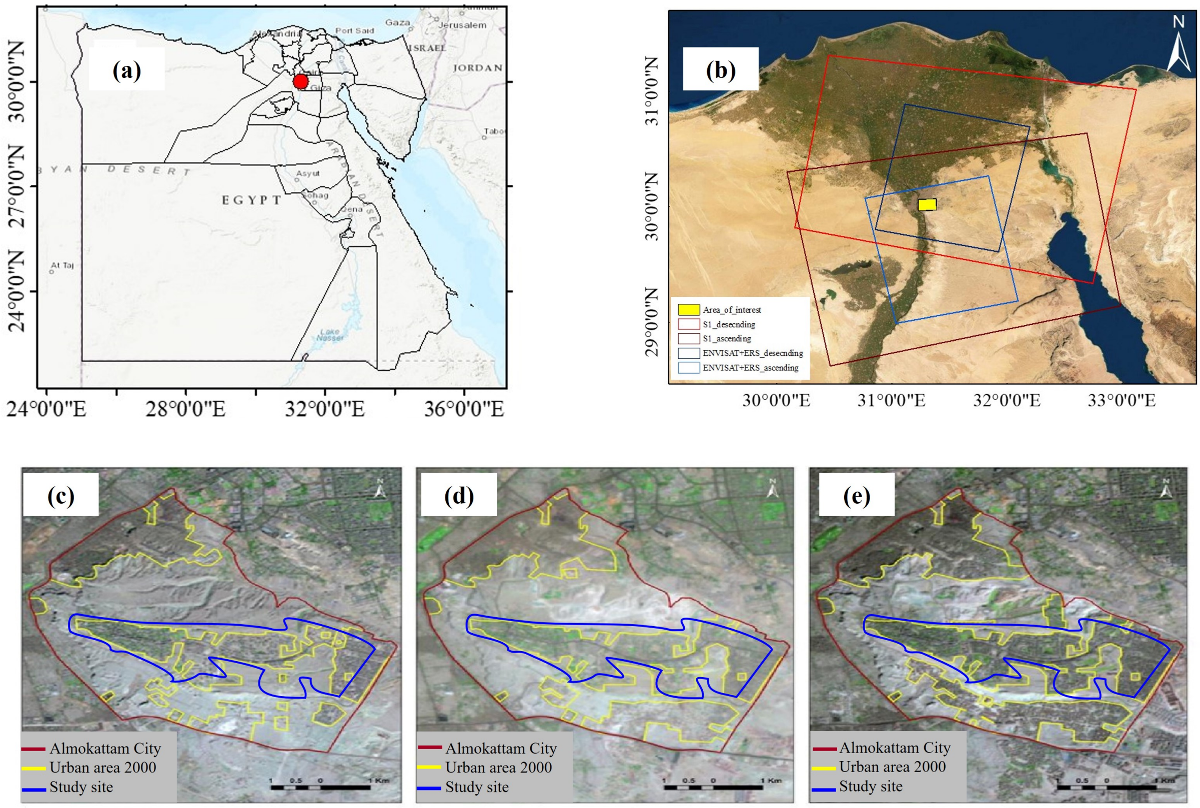

Figure 4.1: Study area. (a) Location of the Almokattam city in Egypt map. (b) The spatial coverage of the datasets over the study area, (c), (d) and (e): Urban area growth from 2000 to 2017.

4.1.1.2 Dataset

This research has introduced a method to integrate multi-satellite SAR data from three independent datasets to derive ground displacement. Set I includes ENVISAT ASAR data from 2008 to 2012. Set II consists of ERS SAR images acquired between 2000 and 2010. Lastly, Set III comprises European Union S1 images collected from 2014 to 2020. Table 4.1 outlines the characteristics of each dataset and Figure 4.2 represent its time-span. Additionally, Figure 4.1b illustrates the spatial coverage of the datasets over the study area.

Table 4.1: SAR Dataset used in this study.

Parameter	**ENVISAT**		**ERS**		**Sentinel-1**	
	Ascending	Descending	Ascending	Descending	Ascending	Descending
Period	21 March 2008 – 16 March 2009	13 May 2004 – 06 March 2012	09 February 2009 – 27 September 2010	20 January 2000 – 17 February 2005	9 October 2014 – 15 July 2020	30 September 2016 – 29 June 2020
No. of images	3	22	4	23	21	17

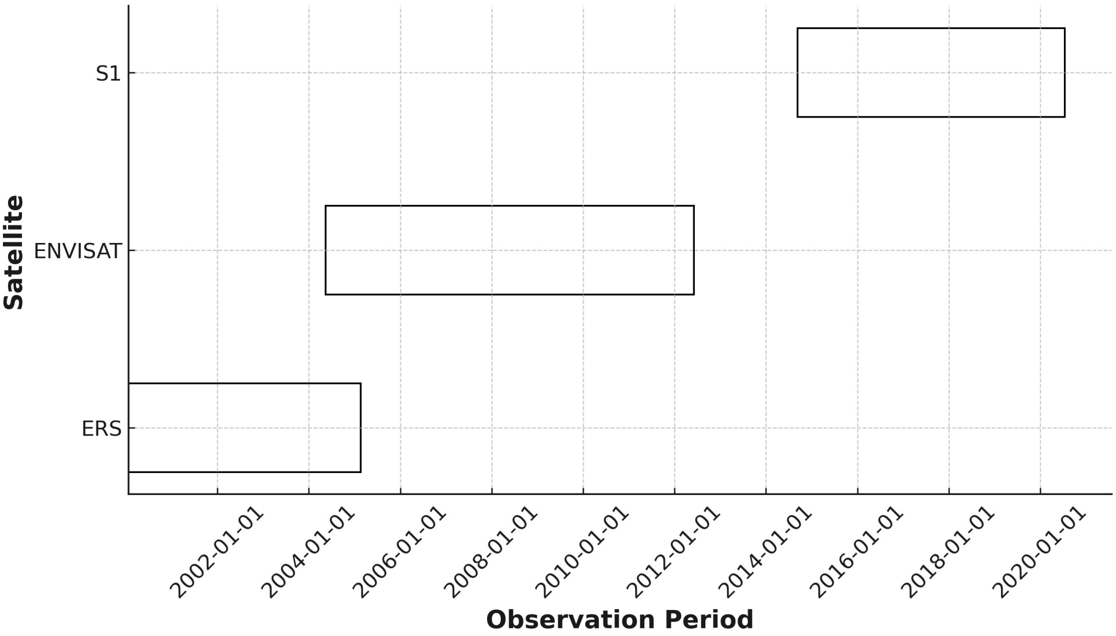

Figure 4.2: Case study 1 SAR Datasets Time-Span.

4.1.2 Results and Analysis

The experimental design utilized three sets of SAR data, as detailed in Section 4.1.1.2. Cross-validation was employed to evaluate the effectiveness of the proposed methodology. Notably, this approach is one of the first to integrate 20 years of multi-satellite SAR datasets over Almokattam city. To generate the long-term displacement time series, LOS displacements were computed for all interferograms within each dataset. These calculations were performed at high-coherence points identified using a specific threshold. Subsequently, all interferograms were geocoded to the WGS84 geographic coordinate system. The combined vertical displacement time series for the ENVISAT, ERS, and S1 datasets were then derived using TSVD inversion, with alignment to the earliest acquisition date of the ERS dataset, which corresponds to 20 January 2000.

4.1.2.1 Multi-baseline DInSAR displacement

SAR image pairs were selected according to rigorous criteria: for ENVISAT and ERS data, the perpendicular baseline was kept below 500 meters, while for S1 data, it was kept below 180 meters. Additionally, all image pairs were required to have a temporal baseline of less than 365 days. Figure 4.3 illustrates the distribution of SAR images within the temporal/perpendicular baseline plane, with connecting lines indicating the data acquisition points.

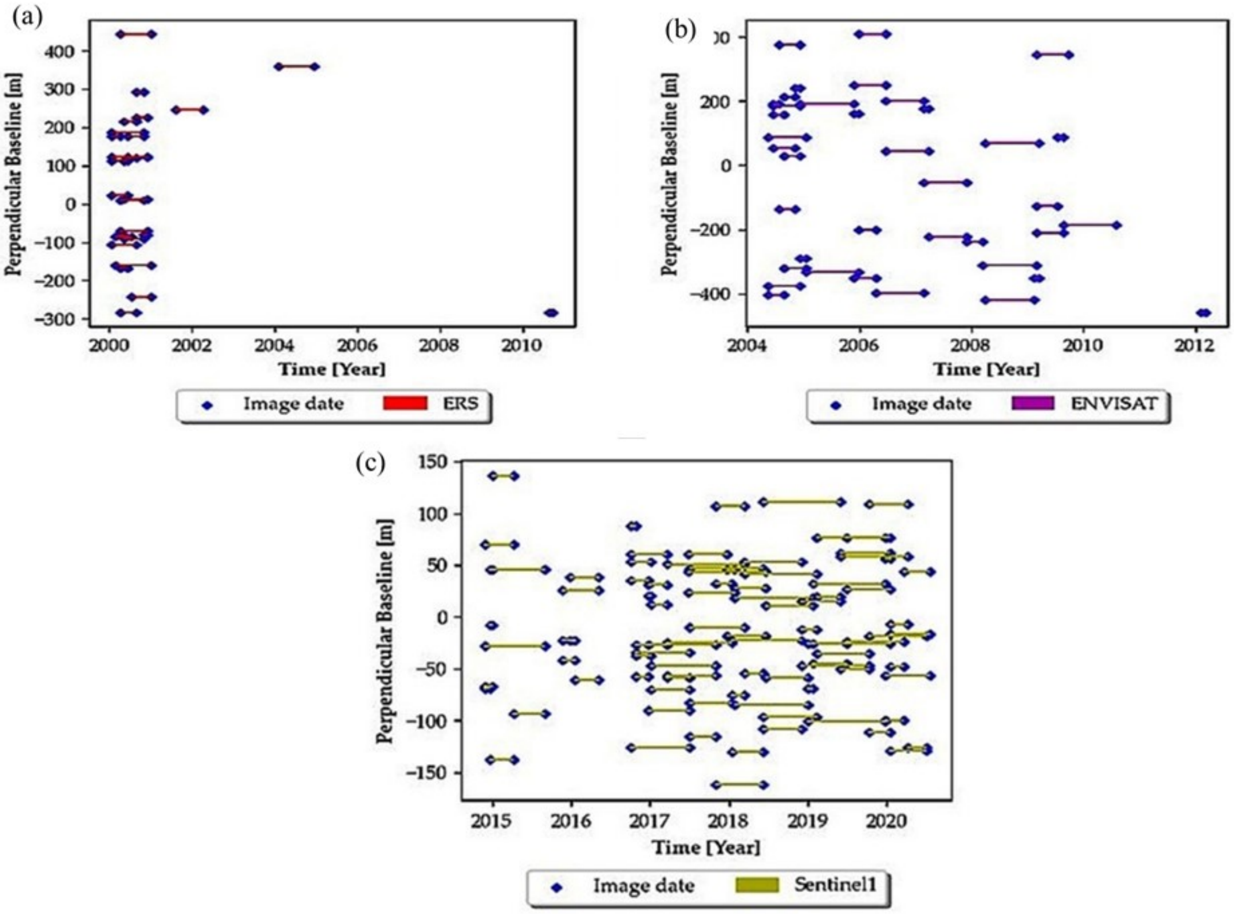

Figure 4.3: Distribution of SAR data in the temporal/ perpendicular baseline domain. (a) ERS. (b) ENVISAT. (c) sentinel-1.

Building on step 1, the DInSAR technique was applied to the co-registered SAR image pairs, utilizing a high-resolution 1 arc-second SRTM3 DEM for topographic phase removal. Each interferogram was multi-looked, with looks applied as 1 × 5 for ENVISAT, 10 × 2 for ERS, and in the range × azimuth direction for S1. The noise was then filtered from the individual interferograms using the Goldstein filter [119], and the unwrapped phase was extracted using the statistically cost network flow algorithm [130].

To address baseline residual errors and long-wavelength atmospheric artifacts, a two-dimensional quadratic model was employed. The LOS displacement was subsequently extracted for high-coherence pixels in each interferogram, using a coherence threshold of 0.50. The geocoded LOS displacements from all interferograms were then referenced to the WGS84 system for further analysis. Figure 4.4a displays the mean vertical displacement velocity from 20 January 2000 to 15 July 2020, calculated by stacking the vertical displacements derived from all interferograms. Subsidence areas (negative velocity) are highlighted in red shades, particularly in the western part of the city, with a maximum subsidence rate of −5.26mm/year.

4.1.2.2 Modified Multi-Satellite SBAS displacement

Using the proposed methodology, we successfully integrated temporally overlapping and gapped DInSAR-derived displacement values from ENVISAT, ERS, and S1. This integration produced a long-term displacement time series that spanned approximately two decades (2000–2020). Figure 4.4b illustrates the mean displacement velocity map generated from the combined ERS, ENVISAT, and S1 data. This map, derived using a set of high-coherence points common to all three datasets, reveals a maximum subsidence velocity of −2.32 mm/year in the western part of the city. As shown in Figure 4.4, the consistent spatial patterns of displacement rates observed before and after integration demonstrate the effectiveness of the proposed method.

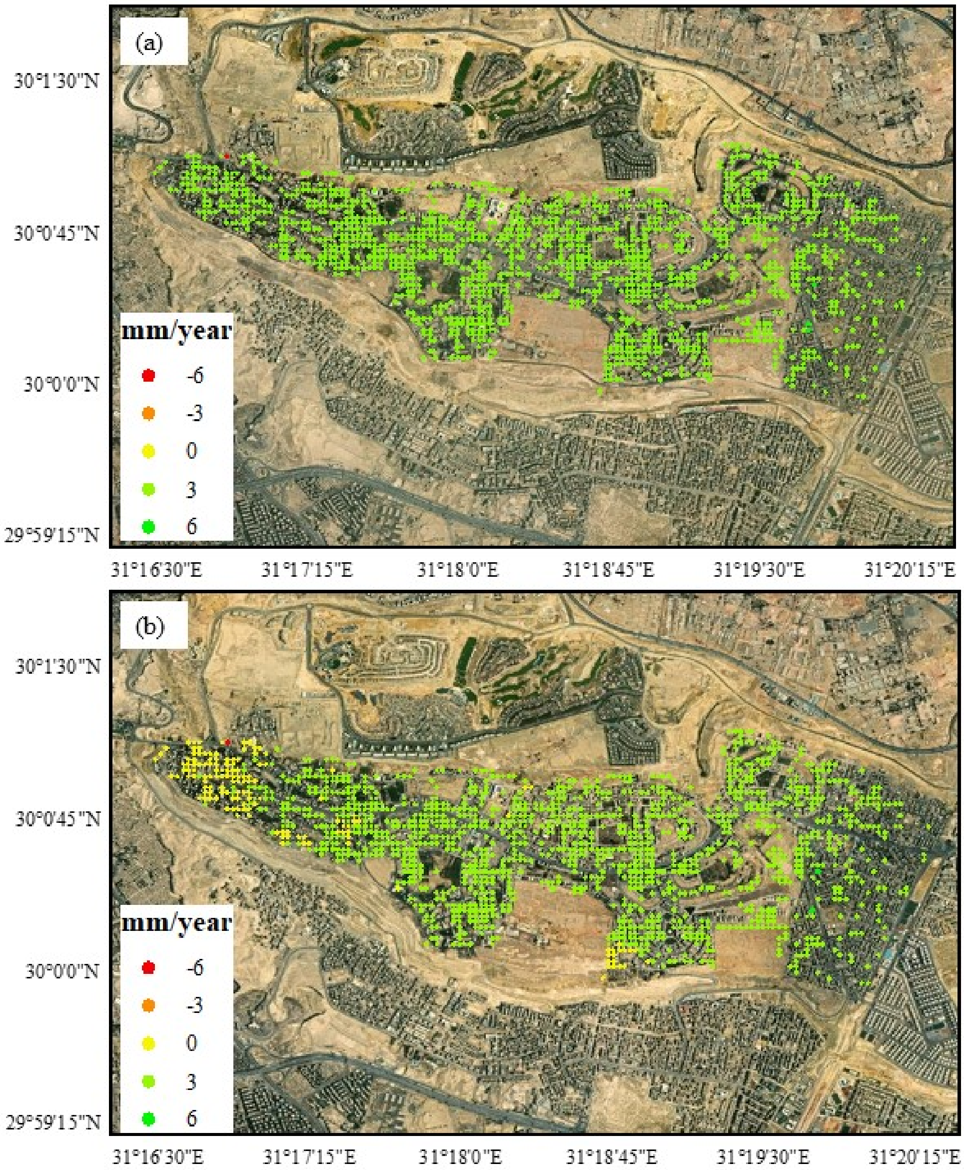

Figure 4.4: Mean displacement velocity (mm/year) of Almokattam city. (a) Pre-integration (b) Post integration.

4.1.2.3 Displacement from individual datasets

Mean vertical displacement velocity maps were generated using the SBAS method for the ERS, ENVISAT, and S1 datasets, as depicted in Figures 4.5. The displacement velocities derived from each dataset were subsequently compared with their corresponding temporal counterparts obtained through the integration.

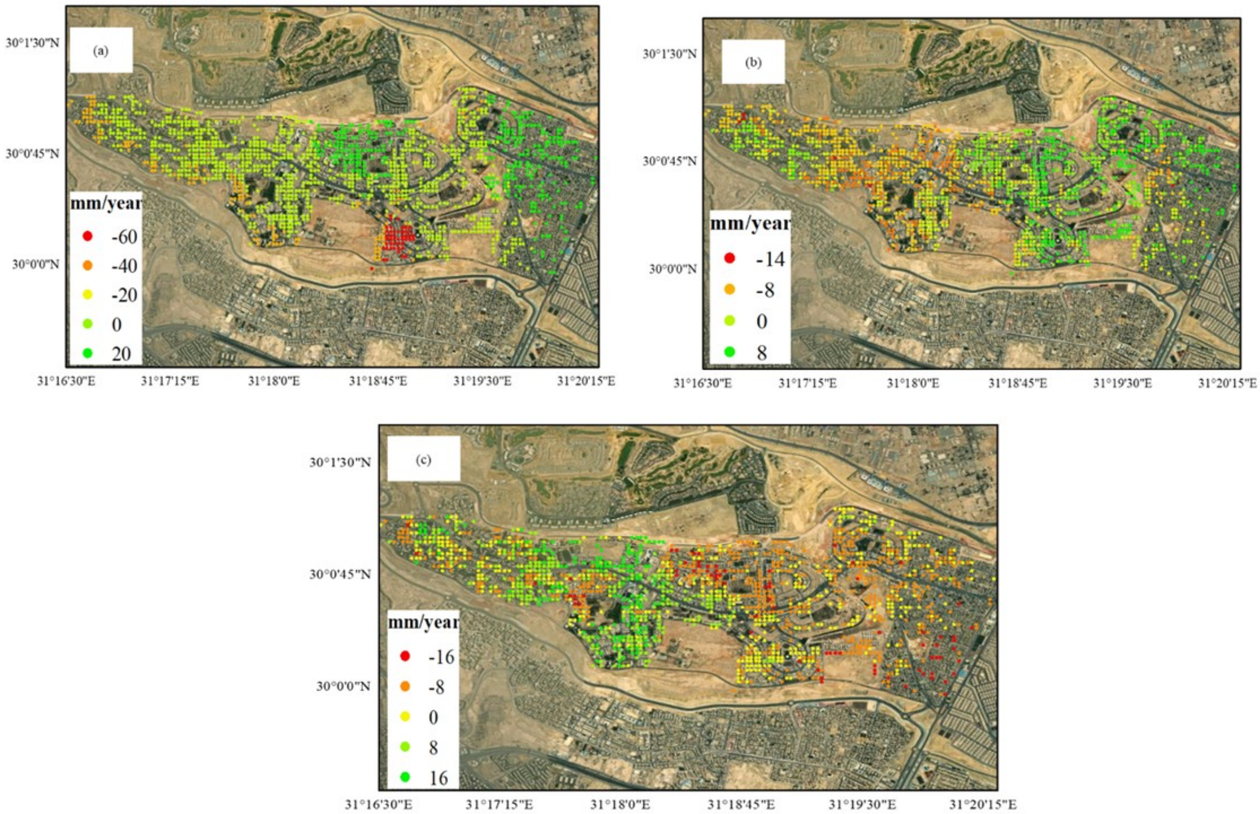

Figure 4.5: Mean displacement velocity map. ERS (20 January 2000 to 17 February 2005), ENVISAT (13 May 2004 to 6 March 2012), and Sentinel-1 (9 October 2014 to 15 July 2020) pre integration.

The results from the ERS data (2000–2010) show a broader displacement range (from −59.57 to 19.19 mm/year) compared to both the ENVISAT data (2004–2012; −13.39 to 7.66 mm/year) and the S1 data (2014–2020; −15.53 to 17.21 mm/year). Despite these variations, a consistent overall displacement pattern is observed across all three datasets, as illustrated in Figures 4.5. However, it is important to note that differences in the time intervals and image acquisition geometries, such as resolution, azimuth, and incidence angle, contribute to some discrepancies observed in the displacement rate maps.

After generating the integrated vertical displacement time series from the three datasets, the mean displacement velocity for each dataset's respective period was individually extracted from the combined time series. These extracted velocities are displayed in

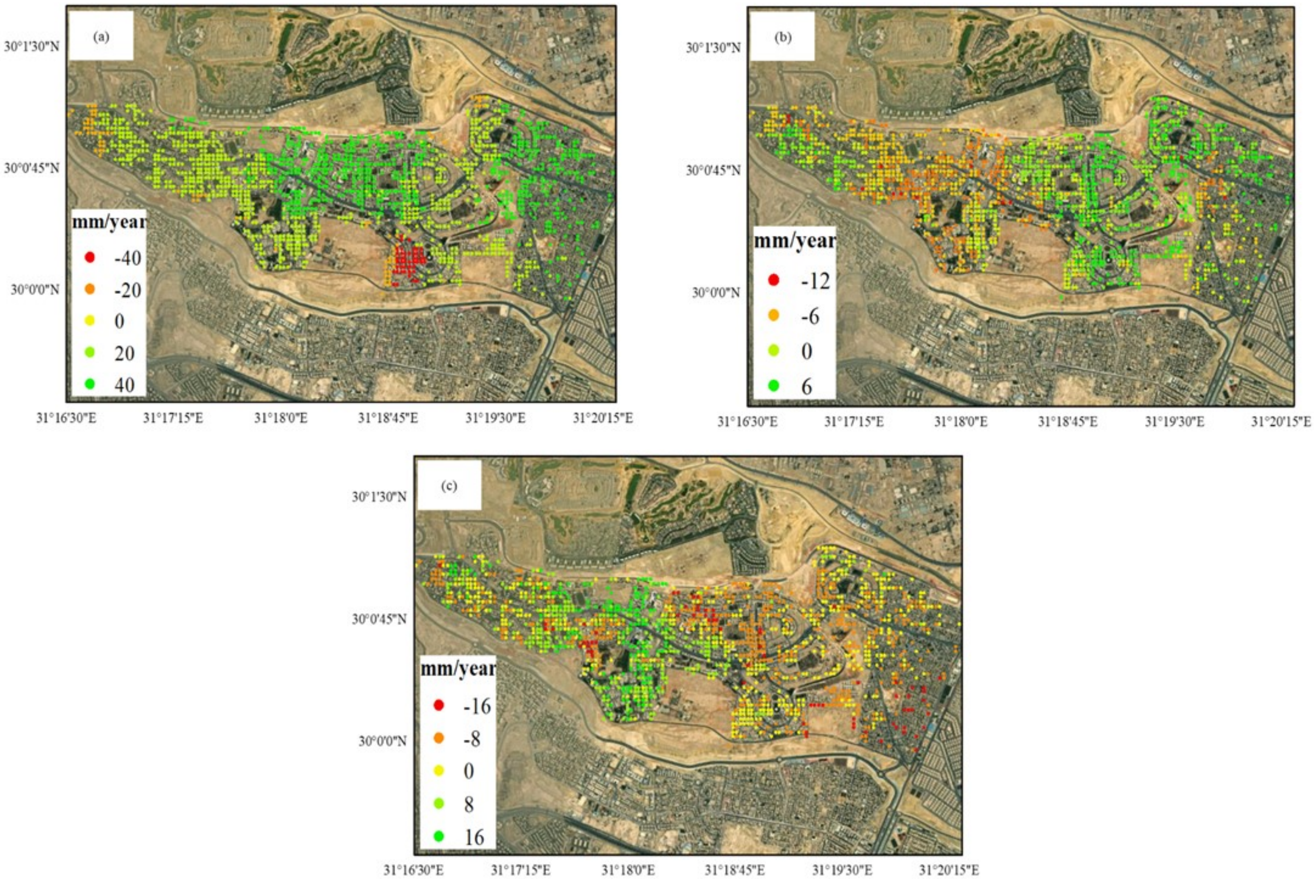

Figure 4.6: Mean displacement velocity map. ERS (20 January 2000 to 17 February 2005), ENVISAT (13 May 2004 to 6 March 2012), and Sentinel-1 (9 October 2014 to 15 July 2020). post integration.

Figures 4.6. A comparison between these velocities and those calculated using the SBAS method reveals minimal variation in the spatial distribution of displacement before and after integration. This consistency demonstrates the effectiveness of the Multi-Satellite SBAS-based method in achieving successful integration.

4.1.3 Evaluation

Due to the absence of field measurements, cross-validation was used to assess the precision of integration results. Two consistency evaluations were employed [131, 132]. First, the mean vertical displacement velocity map obtained from stacking the displacement values of all interferograms (selected image pairs) involved in the integration process was compared with the mean vertical displacement velocity map from the integration itself at a selected common high coherent points. A reasonable agreement between these two velocities would confirm consistency between the maps. The second assessment involved comparing the mean vertical displacement velocity from applying SBAS to each dataset with their corresponding values from the integration. This criterion examined whether the two maps showed similar behavior, with standard deviations of the differences being computed. The numerical and visual analysis is provided in the following subsections.

4.1.3.1 Displacement based on all interferograms

The mean vertical displacement velocity map, created by stacking the displacement values of all selected high-coherence image pairs before integration, was compared to the mean vertical displacement velocity map obtained after integration at selected high-coherence common points. The analysis revealed a mean absolute difference of 2.87 ± 0.21 mm/year, a root mean square error RMSE of 2.88 mm/year, and a correlation coefficient of 0.97 between the two maps. The scatter plot illustrating these results is shown in Figure 4.7a, reflecting a consistent deformation pattern and a high level of agreement between the two maps. Additionally, a histogram of these differences is presented in Figure 4.7b. The statistical analysis shows the effectiveness of the integration approach.

4.1.3.2 Displacement from individual datasets

Mean displacement velocities obtained from Environmental Satellite (ENVISAT), ERS, and S1 data using the SBAS method were compared with those derived from the proposed method. Absolute differences are summarized in Table 4.2, showing a mean absolute difference of 1.87 mm for ERS, 1.5 mm for ENVISAT, and 1.04 mm for S1. These results highlight the effectiveness of the proposed method in retrieving long-term multi-satellite vertical displacement time series. A histogram of these differences is presented in Figures 4.8a–c, with medians of 1.85 mm/year for ERS, 1.49

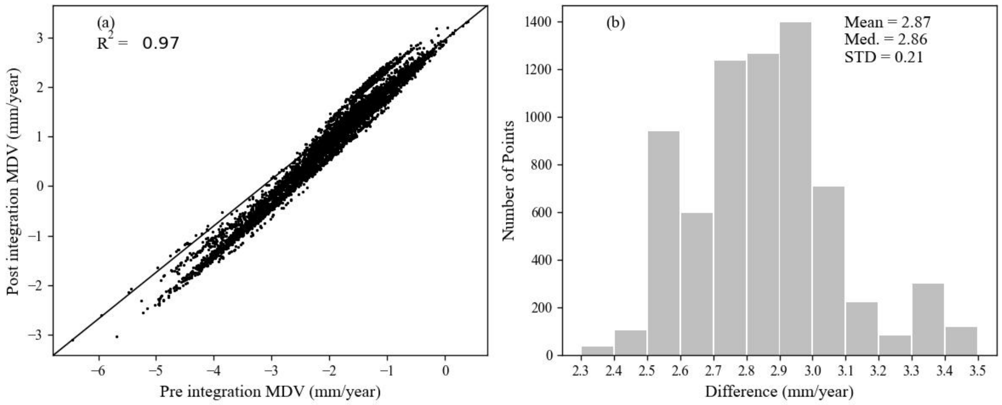

Figure 4.7: Scatterplot and comparison of mean displacement velocity at high-coherence points pre- and post-integration. (a) Correlation between mean displacement velocity pre- and post-integration. (b) Histogram of differences between mean displacement velocity pre- and post-integration.

mm/year for ENVISAT, and 1.08 mm/year for S1, indicating that the S1 dataset provided the best cross-validation results. This is attributed to the larger number of images and smaller temporal resolution of S1 satellite data.

The scatter plots between the two maps resulted from each satellite dataset, pre- and post-integration, are shown in Figure Figure 4.9. The correlation coefficients were 0.92 for ERS, 0.97 for ENVISAT, and 0.99 for S1, demonstrating a high level of consistency in the deformation patterns across the datasets. The root mean square errors (RMSE) were 1.92 mm/year for ERS, 1.66 mm/year for ENVISAT, and 1.19 mm/year for S1. These findings confirm that the Multi-satellite SBAS approach is efficient, with the S1 dataset showing superior performance compared to the ERS and ENVISAT datasets.

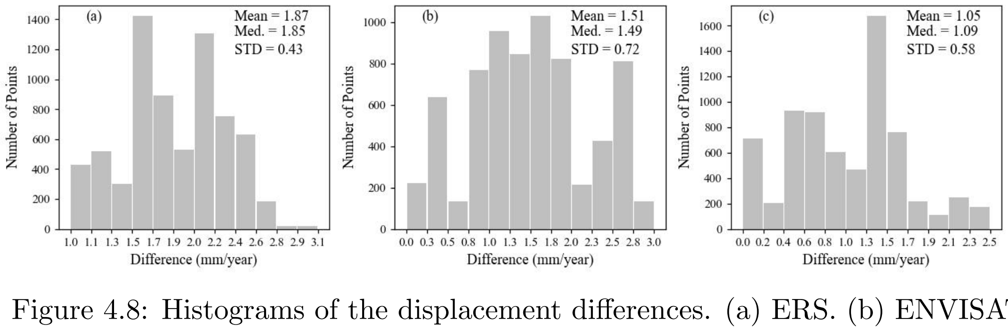

Figure 4.8: Histograms of the displacement differences. (a) ERS. (b) ENVISAT. (c) S1.

Table 4.2: Absolute differences between the mean displacement velocity values of each dataset before and after integration (mm/year).

Satellite	ERS	ENVISAT	Sentinel1
Min. Difference	0.97	0.002	0.0003
Max. Difference	3.11	3.02	2.5
Mean. Difference	1.87	1.5	1.04
RMSE	1.92	1.66	1.19
STD	0.42	0.72	0.57

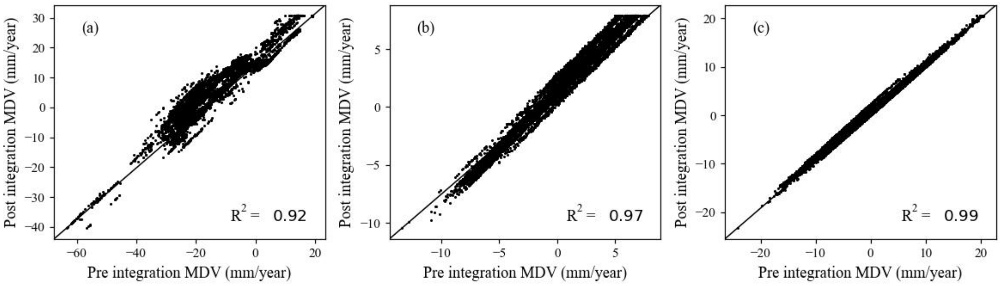

Figure 4.9: Scatterplots of the mean displacement velocities using the SBAS method at high-coherence points.

4.1.4 Discussion

The research methodology proposed Multi-Satellite SBAS to retrieve long-term ground displacement. In this section, several key aspects have been investigated to measure the potential of the proposed method. These aspects encompass the geological characteristics of the study area, Multi-Satellite SBAS, and comparison with previous methods.

4.1.4.1 Displacement in Almokattam city, causes and implications

The geological composition of Almokattam Mountain has been thoroughly examined in the literature. It has been reported that the Upper Eocene rocks, known as the Maadi Formation, consist of brown-colored cracked limestone, marl, and claystone. In contrast, the Middle Eocene rocks, or Almokattam Formation, are composed of white to gray limestone with lesser amounts of clay and marl. This geological structure has been identified as a significant factor contributing to the steep slopes in the region [133] as shown in Figure 4.10. Consequently, the Almokattam Formation is noted for its greater solidity and durability compared to the Maadi Formation [127].

Small-scale folds, which slope downward in a southeast or east direction, have been observed. These folds are associated with block faulting [134] and typically have spacings ranging from 5 to 8 meters. They are predominantly steep and characterized by slabs varying from less than 20 meters to 110 meters in length, with deep corners and angles between 60 and 70 degrees [135].

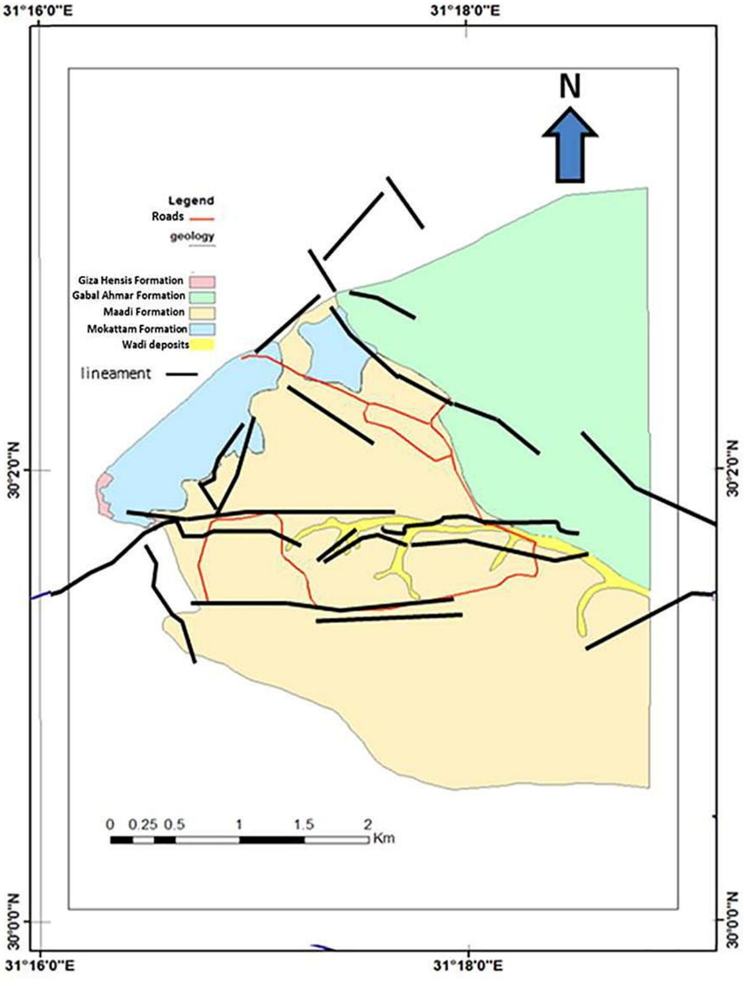

Figure 4.10: Geological map of Almokattam mountain.

The experimental results revealed a severe subsidence between 2000 and 2005 (ERS time period), with a rate reaching -59.5 mm/year and a rate of -13.39 mm/year from 2004 to 2012 (ENVISAT time period). This significant difference in vertical displacement velocity magnitude between ERS with ENVISAT and S1 is due to the actual events, as the most severe deformation occurred in 1993, 2000, 2002, and 2004. The primary factors contributing to the deformation of Almokattam city include: (1) the rough topography, with elevations ranging from 11 to 220 meters; (2) the potential presence of active faults; (3) the heterogeneous composition of the mountain's rocks; (4) environmental issues such as sewage leakage; (5) the slope angle's impact on rock failure risk—steeper slopes, like those reaching 70 degrees in Almokattam city, significantly affect slope stability; (6) the natural susceptibility of the Almokattam mountain to erosion and instability, exacerbated by human activities, with the situation worsening due to population growth (as shown in Figure 4.1b,c,d, which increased water infiltration and unregulated construction; and (7) the removal and replacement of vegetation in developed areas.

In the other hand, uplift pattern was observed in many points across Almokattam City especially in the east part of the city. This uplift pattern can be attributed to geological, geotechnical, and anthropogenic factors. Tectonic activity, fault movements, and subsurface stress redistribution may contribute to localized uplift. Additionally, the presence of gypsum- and clay-rich layers can cause ground expansion when exposed to water, while fluctuations in the groundwater table due to extraction or leakage may also induce uplift. Urban development, including construction and excavation, alters subsurface stress, leading to differential ground movement. Furthermore, karst activity in the limestone bedrock and post-seismic or isostatic adjustments could play a role.

Figure 4.4b illustrates irregular deformation across various locations, with the western part of Almokattam city being particularly prone to landslides, where the displacement rate reached -2.32 mm/year. This is consistent with the ongoing subsidence observed in the western part of the Almokattam Plateau during the study period. Validation results indicate that the proposed method effectively provided valuable subsidence information.

4.1.4.2 Modified Multi-Satellite SBAS for SAR Data Integration

InSAR has emerged as one of the most robust techniques for monitoring ground subsidence. However, when utilizing a single sensor and single platform, InSAR analysis encounters specific challenges, especially within urban environments. To overcome these obstacles, the growing availability of SAR satellites with varying temporal and spatial resolutions has been harnessed to develop a multi-platform InSAR time series. This integration is expected to alleviate the limitations of single-sensor or single-platform data. This motivation led to the development of our post-processing integration method. Notably, the proposed method offers several advantages compared to existing literature: (1) it does not require an external deformation model to bridge time gaps between datasets; (2) LOS ground displacement is generated without the need for a predefined displacement model; (3) a relatively small number of SAR scenes are used; and (4) it exploits the strengths of both PS and DS techniques to enhance the density of high-coherence points.

4.1.4.3 Comparison with previous studies

Due to the unavailability of field measurements, cross-validation was employed for evaluation. The key findings of this research were compared to previous studies in the area, specifically two significant works that utilized InSAR data during the study period. Poscolieri et al. [136] identified ground deformation in the Greater Cairo Metropolitan Region from 2003 to 2009 using ASAR SLC VV-polarization scenes in descending mode, applying Interferometric Stacking and PSs Interferometry to derive displacement. They reported subsidence rates of -2 to -5 mm/year in the west and -5 to -7 mm/year in the west-south areas of the city, and mapped numerous NW-SE-oriented normal faults. Their findings included a sinking phenomenon between these faults, particularly at point targets on the down-thrown sides. Additionally, Aly et al. [137] used a PS interferometric technique to measure subsidence in Greater Cairo, analyzing 34 InSAR images from the ERS-1 and ERS-2 from 1993 to 2000. The greatest subsidence was observed on the west side of Almokattam Hill, with rates of -4 to -7 mm/year, decreasing towards the middle of the hill to -1 to -3 mm/year, with some uplifts recorded in the east. They noted minor differences in vertical displacement when compared to earlier studies, attributing these discrepancies to different methodologies, SAR datasets, and time intervals.

In comparison, our proposed methodology has demonstrated sub-millimeter accuracy in estimating the subsidence and its trends. The Sentinel-1 data outperformed the results from ENVISAT and ERS, exhibiting a high degree of consistency, particularly due to the larger number of images and smaller temporal resolution used in the integration process. This consistency supports our hypothesis that vertical displacement accounts for the majority of the observed displacement. Our study underscores the importance of integrating multi-sensor and multi-track SAR data for long-term displacement monitoring, optimizing the potential of these datasets for comprehensive deformation monitoring.

4.2 A Machine Learning-Based Method for Multi-Satellite SAR Data Integration

Our study utilizes high-resolution CSK and TSX images, along with short-cycle S1 images, focusing on reclaimed areas near Hong Kong's Kowloon City. The AAD measured from 2008 to 2019 ranges from -12.86 to 11.63 mm/year. Evaluation metrics such as RMSE, MAE, correlation coefficient, and R-squared are used to assess the effectiveness of SVR in integrating SAR datasets. The results demonstrate that SVR excels in performance, accuracy, and generalization, highlighting the potential of this method for multi-satellite SAR data integration.

4.2.1 Materials

4.2.1.1 Study Area

Kowloon peninsula is the study area of this research. It is the most populous district of Hong Kong, China [2]. Because the land in Hong Kong is scarce and valuable, the government has been reclaiming land from the sea to construct skyscrapers, ports, airports, etc., Monitoring the subsidence of reclaimed lands for a long time and with precision can help to avoid geological hazards and financial loss. Figure 4.11 shows the location of the Kowloon district on the Hong Kong map.

The Kowloon Peninsula is the study area of this research, located in Hong Kong, China, and is one of the most densely populated districts in Hong Kong [2]. Due to the limited and highly valuable land in Hong Kong, the government has pursued extensive land reclamation from the sea to support the construction of skyscrapers, ports, and airports. Monitoring the long-term subsidence of these reclaimed lands with precision is crucial to preventing geological hazards and financial losses. Figure 4.11 illustrates the location of the Kowloon district within the map of Hong Kong.

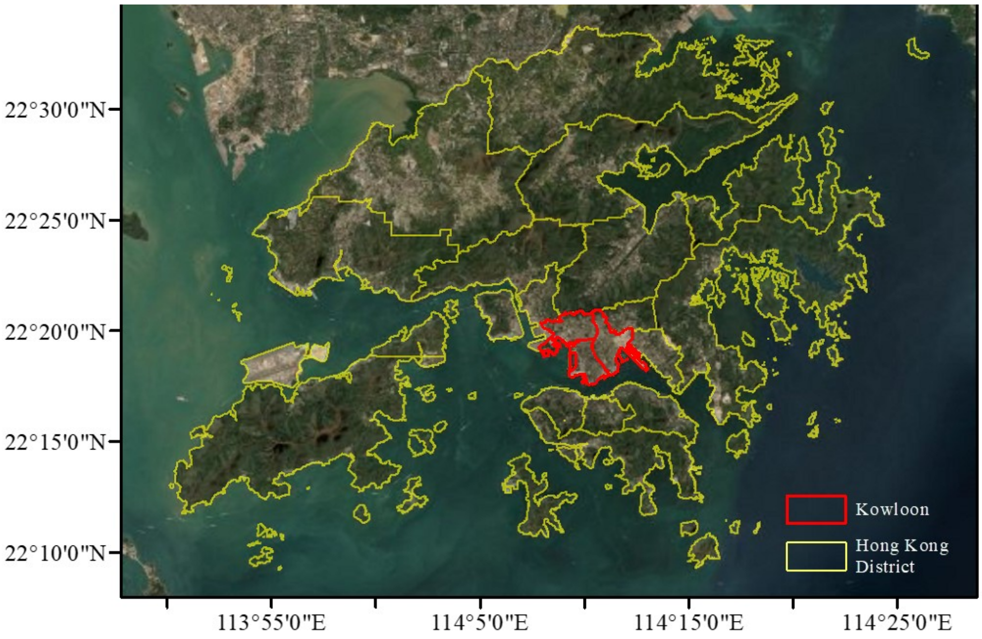

Figure 4.11: Location of Kowloon area framed by the red color.

Multiple phases of land reclamation have led to the significant expansion of the Kowloon Peninsula, as depicted in Figure 4.12. The majority of the southern and western reclamations were completed before 1904, with subsequent reclamation along the main Tsim Sha Tsui shoreline occurring by 1982. Reclamation efforts in Hung Hom Bay began in 1994 and were fully completed by 2019. The West Kowloon Reclamation, initiated by the Airport Core Programme, was largely finished by 1995. Reclaimed lands are prone to prolonged subsidence, which can endanger building structures and subterranean infrastructure, such as water and sewage systems. Ground deformation has been a persistent issue in Hong Kong, particularly on land reclaimed from the sea [138].

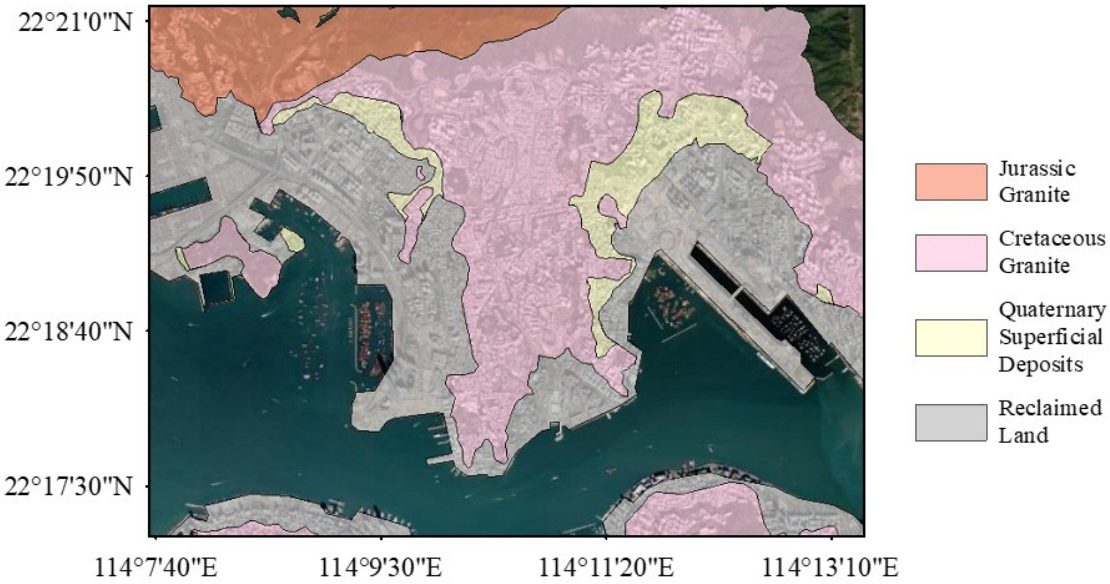

Figure 4.12: Geological map and reclamation land within the study area [1].

4.2.1.2 Dataset

Multi-satellite SAR datasets were gathered over the Kowloon area, as detailed in Table 4.3 and its time span illustrared in Figure 4.13. To comprehensively analyze the deformation mechanisms across the Kowloon Peninsula, three distinct sets of SAR data, each operating at different frequency bands, were selected. The coverage of these datasets is depicted in Figure 4.14. It is worth noting that these three SAR data sets are time-overlapping, allowing for a robust temporal analysis of the region's deformation patterns.

Table 4.3: Characteristics of the selected SAR data.

Satellite	TerraSAR-X (TSX)	COSMO-SkyMed (CSK)	Sentinel-1 (Path_11)		
			Frame_67	Frame_68	Frame_69
Orbital	Ascending	Descending	Ascending	Ascending	Ascending
Period	20081025−20170125	20160829−20190204	20151212−20160504	20160516−20170228	20150709−20151013
No. of image	130	16	8	18	9
Polarization	VV	HH	VV	VV	VV
Incidence angle	37°	38°	37.5°	37.5°	37.5°
Band	X	X	C	C	C
Wavelength (cm)	3.1	3.6	5.6	5.6	5.6

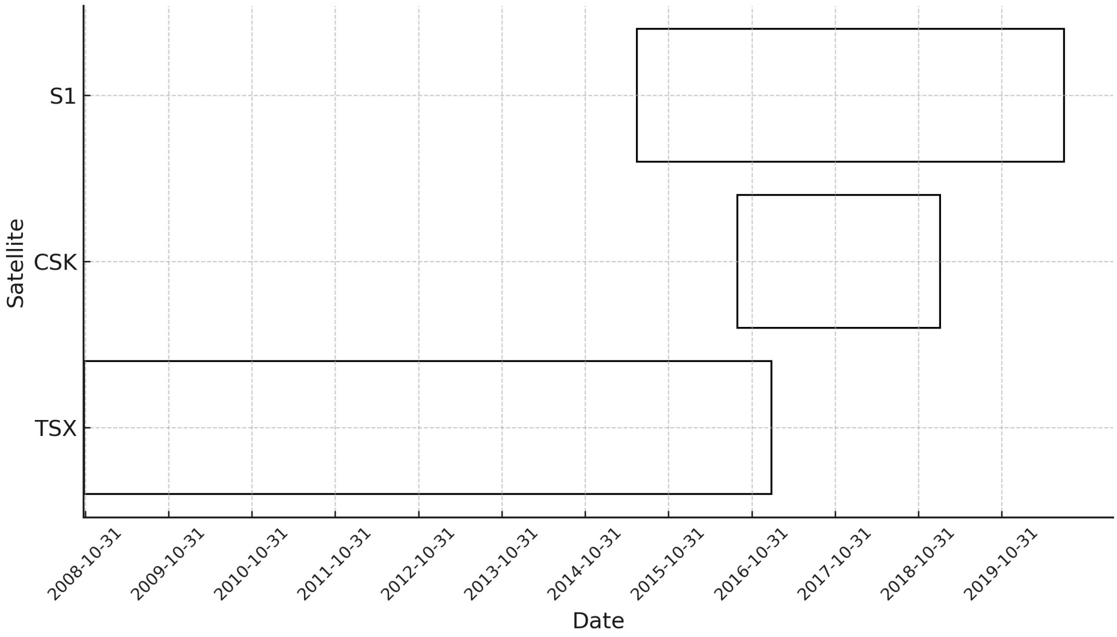

Figure 4.13: Case Study 2 SAR Datasets Time-Span.

4.2.2 Results

4.2.2.1 Interferogram generation

DInSAR technique was employed to C- and X-band SAR images, particularly, selected image pairs based on the perpendicular and temporal baseline threshold as shown in Table 4.4. Consequently, 1180, 98, and 181 interferograms were created from the

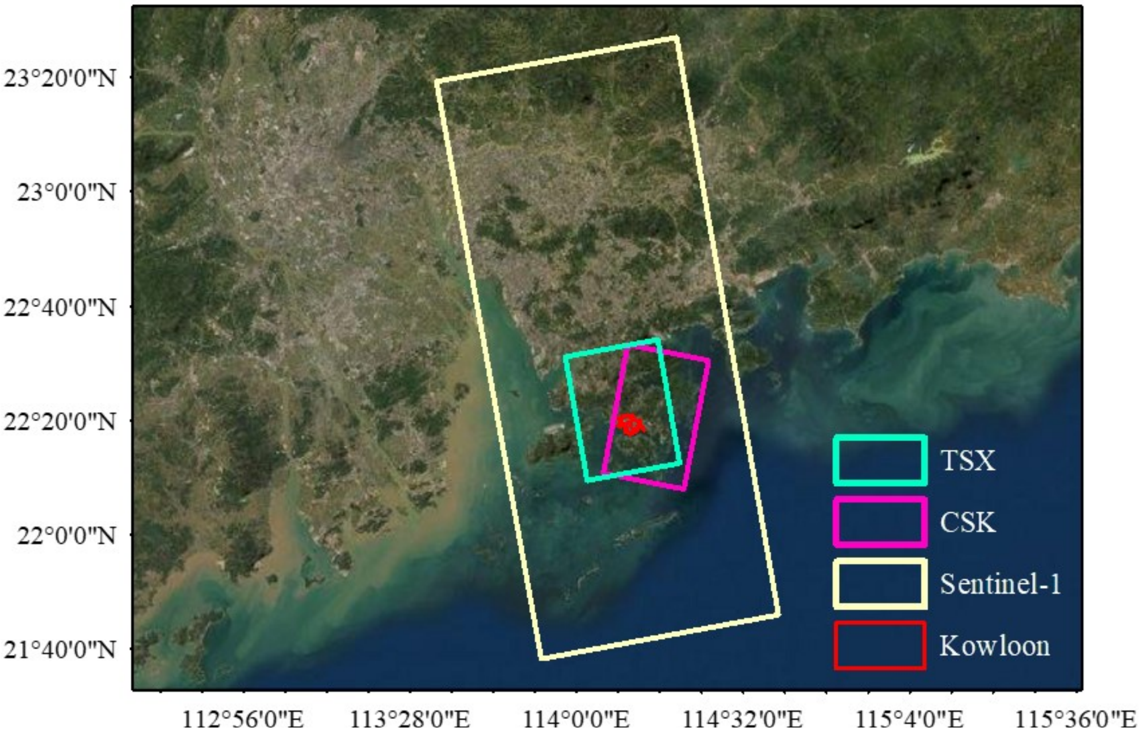

Figure 4.14: SAR data coverage for the study area.

TSX, CSK, and S1 datasets, respectively. Figure 4.15 and Figure 4.16 shows the configuration of the baseline of interferometric networks for individual datasets.

Table 4.4: Perpendicular and temporal baselines threshold of the three SAR datasets

Satellite	TerraSAR-X (TSX)	COSMO-SkyMed (CSK)	Sentinel-1 (Path_11)		
			Frame_67	Frame_68	Frame_69
Perpendicular baseline	150	1200	95	95	95
Temporal baseline	365	900	150	150	120

Across the monitoring period, the small baselines describing the accessible scenes exhibited good density and redundancy, and all scenes were used for DInSAR analysis. The image pairs were co-registered, and the phase difference was computed to generate DInSAR data. A DEM from SRTM was then used for topographic phase removal. A complex multi-look operation was performed independently to mitigate the effects of decorrelation noise: 5 looks in both azimuth and range directions for TSX, 5 looks in azimuth and 4 looks in range direction for CSK, and 10 looks in azimuth and 2 looks

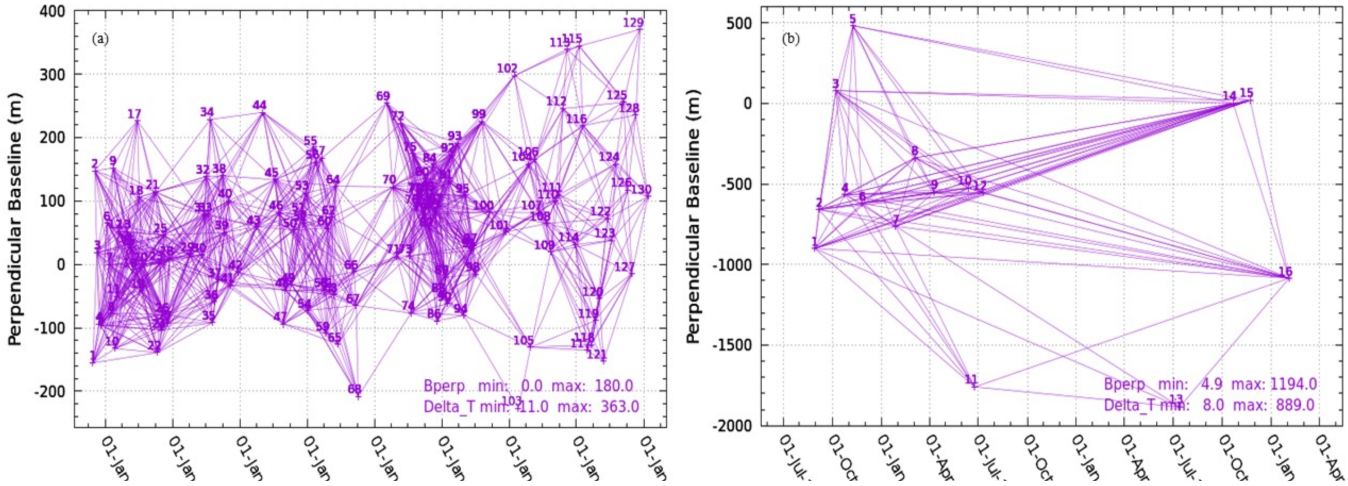

Figure 4.15: Baseline configuration of (a) TSX, and (b) CSK, datasets.

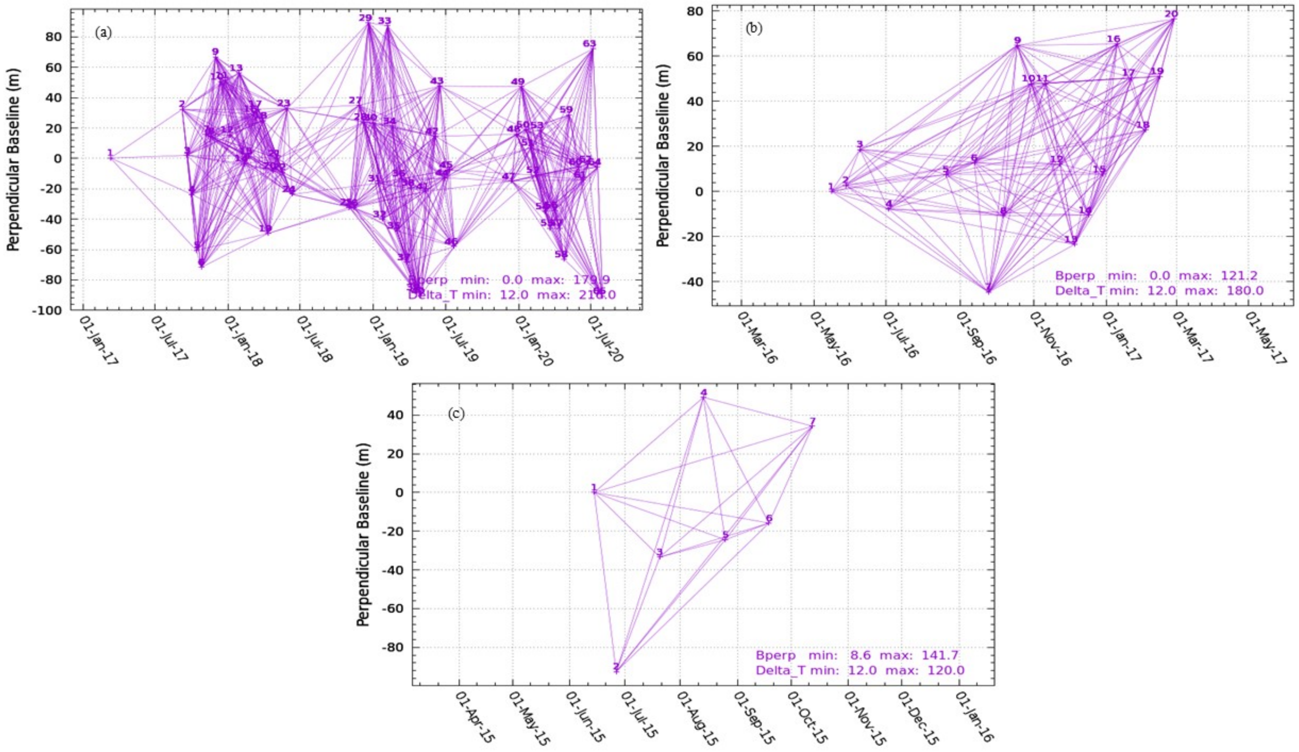

Figure 4.16: Baseline configuration of (a) S1 (fram 65), (b) S1 (fram 68) , and S1 (fram 69) datasets.

in range for S1. Additionally, noise filtering was applied to single interferograms.

Phase unwrapping was carried out using the extended minimum cost flow algorithm. Incoherent and sea areas were automatically masked off, ensuring that only the set of coherent pixels common to all interferograms was used for phase unwrapping. The unwrapped phase was calibrated to a unique ground reference point considered stable. Finally, the unwrapped phase was converted into LOS displacements, and a map of the average LOS deformation velocity was generated from each SAR dataset. The LOS-projected deformation datasets were transformed into a vertical (up-down) direction before integration using Equation 3.3.

4.2.2.2 Vertical Displacement

The vertical displacement velocities were displayed on a grid of highly coherent pixels that were common across the three datasets, specifically those with a temporal coherence greater than 0.8, to ensure accurate results. The number of selected coherent points varied across datasets because the maximum observable range is directly proportional to the radar wavelength. Consequently, a larger number of points were identified for S1 data. The C-band radar wave, which has a longer wavelength than the X-band, has a higher probability of detecting large-gradient deformation. Figure 4.17 illustrates that from 2008 to 2020, the AAD varied between -12.38 and 11.12 mm/year. Figure 4.18a, b, and c, respectively, show the AAD in the vertical direction for the X-band TSX, X-band CSK, and C-band S1 datasets before integration. The selected high-coherence points transition from blue to red, indicating an increase in subsidence values. The three datasets were resampled to the same resolution to ensure they were comparable and consistent for subsequent processing.

According to TSX data from 2008 to 2017, the ground displacement across Kowloon ranges from -9.72 to 6.25 mm/year. Additionally, a maximum subsidence rate of -8.49 mm/year is depicted on the CSK displacement map from 2016 to 2019, as shown in Figure 4.18b. The AAD ranges from -9.19 to 9.82 mm/year from 2015 to 2020, as illustrated by the S1 displacement map in Figure 4.18c. Ground displacement

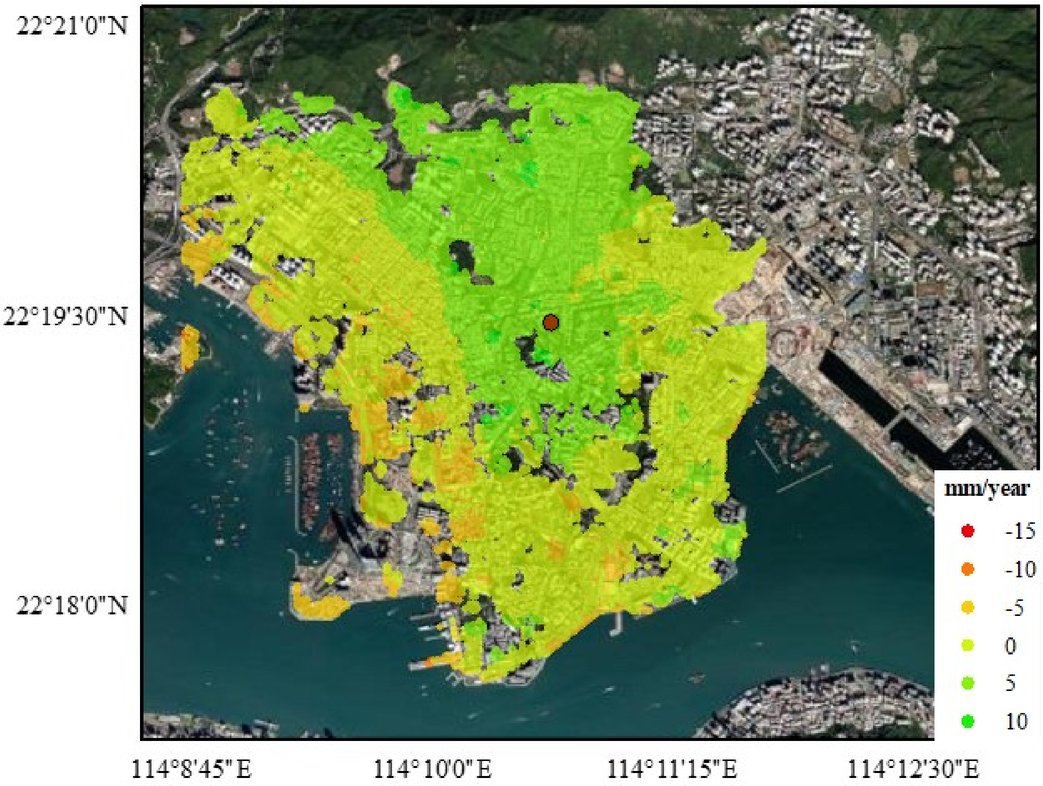

Figure 4.17: AAD of Kowloon from 2008 to 2020 by stacking all multi-baseline interferograms of TSX, CSK, and S1 datasets.

is primarily observed along the top and western borders of Kowloon in all three displacement maps. Since a portion of the Kowloon Peninsula has been reclaimed from the sea, the non-reclamation region is used as the reference area (black rectangle in Figure 4.18) for all datasets that is assumed to be stable. This area serves as the baseline for measuring displacement across the dataset. The reference point is identified at the point that has the highest coherence, is most accessible, and has minimal or no displacement over the observation period.

4.2.2.3 Fusion Results of TSX, CSK, and S1 datasets

The integration results compensate for the shortcomings of individual datasets, as the map reflects both the high resolution of TSX and CSK data, as well as the enhanced observing capability of Sentinel-1. Positive values (green) represent ground uplift,

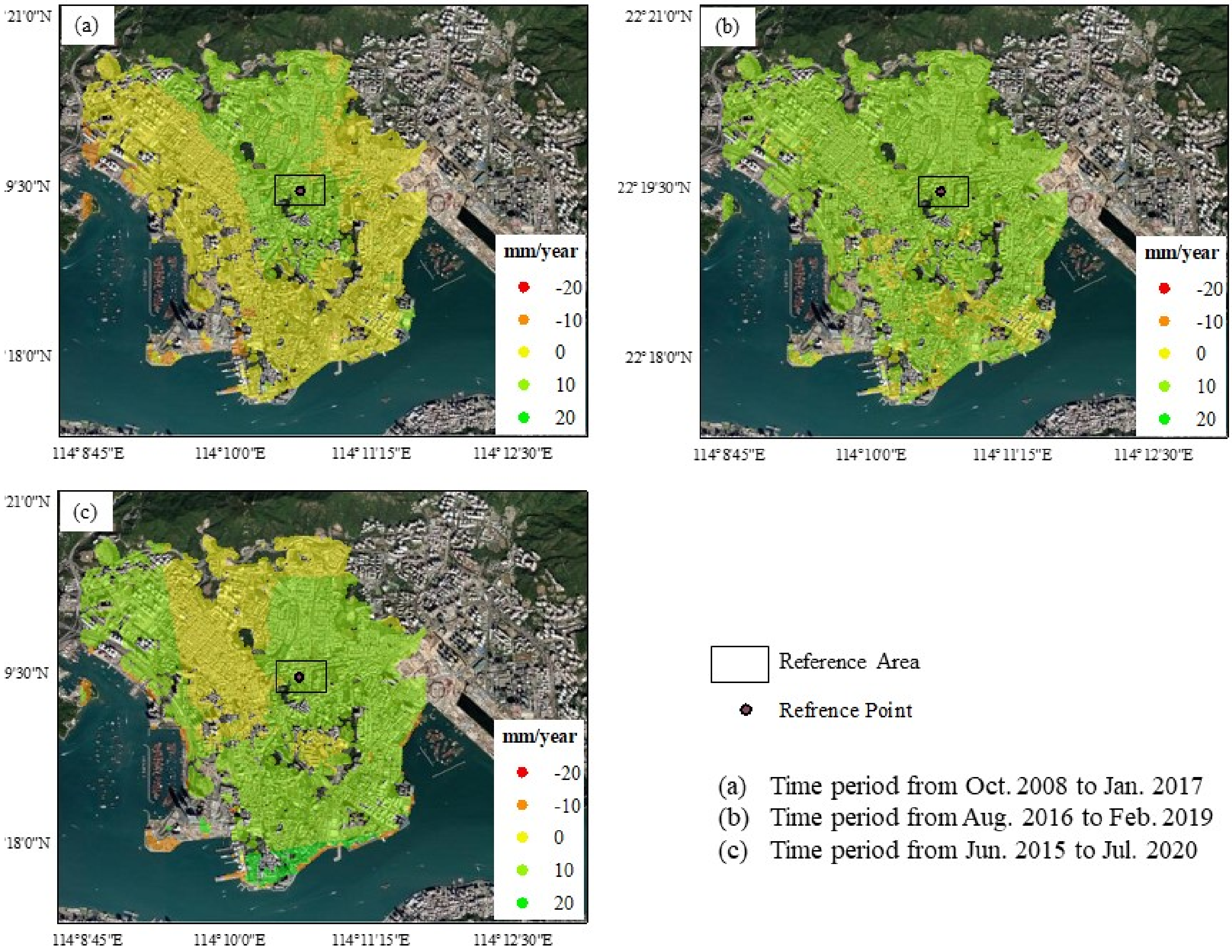

Figure 4.18: AAD maps of Kowloon. (a) TSX. (b) CSK. (c) Sentinel-1A.

while negative values (red) indicate ground subsidence. Figure 4.19) illustrates the integration results of the TSX, CSK, and S1 data. The average annual velocity ranged from -12.86 to 11.63 mm/year. The displacement behavior and magnitudes computed from the integration of the three datasets closely match previous research in this area [4].

4.2.3 Evaluation

Since field measurements were unavailable, four evaluations were conducted to assess the internal precision of the proposed methodology; the first one is an assessment of the SVR model performance in multi-band displacement integration by computing the

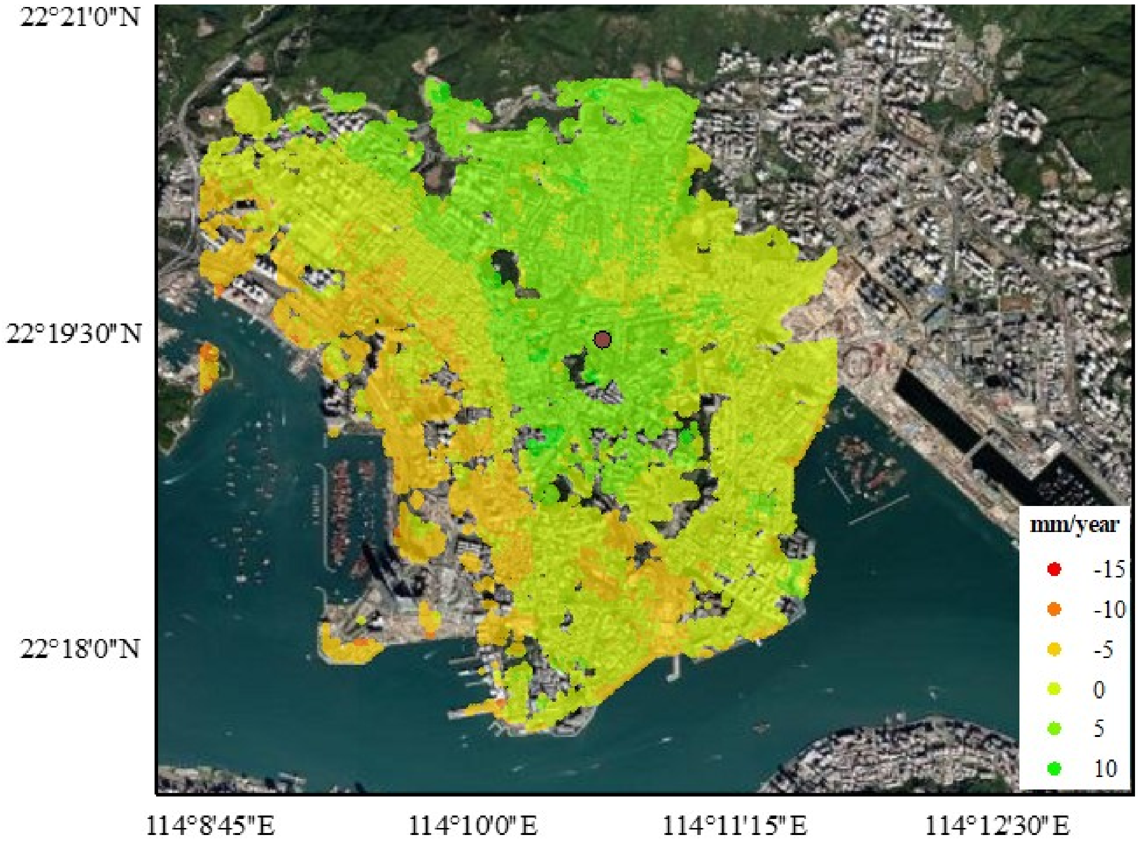

Figure 4.19: Combined AAD map resulted from SVM-based integration of TSX, CSK, and S1 datasets.

RMSE $= \sqrt{\frac{1}{n}\sum_{i=1}^{n}(y_i^P - y_i^O)^2}$, Mean Absolute Error $MAE = \frac{1}{n}\sum_{i=1}^{n}|y_i^P - y_i^O|^2$, Correlation Coefficient $r = \frac{\sum(y_i^O - \overline{y}^O) - (y_i^P - \overline{y}^P)}{\sqrt{\sum(y_i^O - \overline{y}^O)^2 - (y_i^P - \overline{y}^P)^2}}$, R-squared R^2 of the difference between the mean vertical displacement velocity map obtained by stacking the displacement values of all participating image pairs before integration and the mean displacement velocity map derived from the integration process at a set of high-coherence common points, where n is the total number of observations y^O or predictions y^P in the testing period. Also, $\overline{y}^O$ and $\overline{y}^P$ are the averages of the observed and integrated values, respectively. The other three evaluations are cross-validations:

- Comparing the relationship between results before and after integration for datasets with the same flight direction, geometry, and time span.
- Comparing the results of each dataset separately before and after integration.

- Comparing the relationship between results before and after integration for different frames of the same satellite.

4.2.3.1 SVR validation results

The SVR integration results were validated according to the scheme described in Section 4.2.3. $RMSE$, MAE, correlation coefficient, and R-squared of the differences between Figure 4.17 and Figure 4.19 are computed at a set of selected high coherent points as summarized in Table 4.5. Figure 4.20 elucidates the scatter map between AAD from stacking all interferograms of TSX, CSK, and S1 and the SVR-based integration model. The results indicate that the two datasets exhibit a consistent deformation pattern.

Table 4.5: Performance of the SVR Integration model.

Evaluation Index (mm/year)	value
$RMSE$	1.12
MAE	0.88
Correlation coefficient (r)	0.97
R-squared	0.95
Standard deviation (STD)	0.69

According to the statistical evaluation parameters, the results demonstrated that the SVR soft computing model is superior in terms of integration performance, accuracy, and generalization capability. SVR thus shows significant potential in multi-satellite SAR data integration and related fields.

4.2.3.2 Cross Validation Results

First, TSX and S1 SAR datasets were used for cross-validation as described by [4]. These datasets were obtained in ascending directions and have the same geometry. The displacement velocity maps of the two datasets over the Kowloon area from

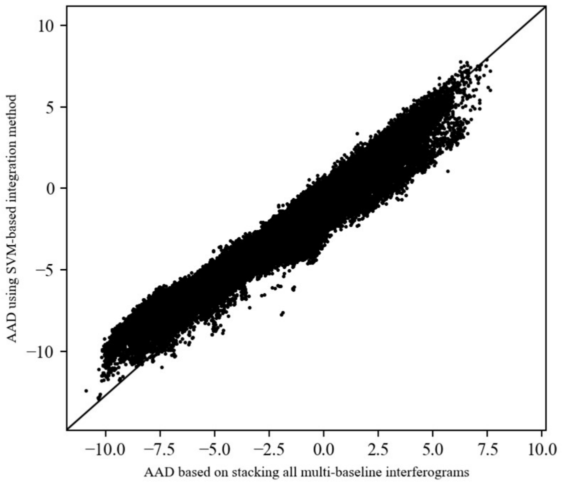

Figure 4.20: Scatter map of AAD pre and post SVM-based integration.

the same period (2015-2017) were extracted before applying the proposed integration method. To validate the derived displacement, the absolute differences between the two datasets (Δd_{TSX-S1}) were calculated, as illustrated in Table 4.6, where the vertical displacement velocity maps are resampled onto a common grid.

Table 4.6: Absolute difference between AAD obtained from TSX and S1.

Evaluation index (mm/year)	Δd_{tsx-s1}	
	Pre	Post
Mean	7.15	5.44
Median	6.05	4.87
STD	4.99	3.78
$RMSE$	8.72	6.62

The normality of the distribution of the difference between the two dataset's results is examined using a quantile-quantile (q-q) plot and histogram for AAD resulting from both datasets for the period 2015 to 2017, as shown in Figure 4.21 a and b, respectively.

On the right side and center of Figure 4.21a, there is an almost-perfect normal distribution. The tails, particularly those on the left, show large departures from the

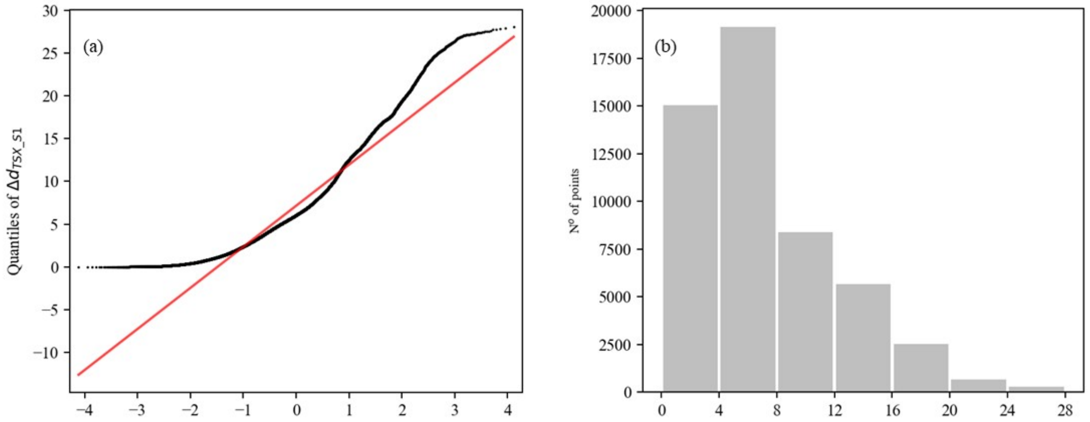

Figure 4.21: Quantile-quantile (q-q) plot and histogram of Δd_{TSX-S1} from 2015 to 2017.

normal distribution; the histogram, Figure 4.21 b, shows that the distribution on the left is right-skewed. These departures could be related to the uncertainty in the SAR dataset, as well as atmospheric delay and acquisition time. The (Δd_{TSX-S1}) before and after integration were compared and described by box plots as shown in Figure 4.22. Figure 4.22 demonstrates that the distribution is biased toward lower values and the mean is more positive than the median, as shown by the boxplot graph, which will automatically identify the min/max range, 75 percent quantile range, mean value, and outliers. The $RMSE$ values are 8.72 and 6.62, and the standard deviations are 4.99 and 3.78 mm/year before and after integration, respectively. After using the ML-based integration method, the results have shown a greater improvement.

Second, a quantitative study of the absolute differences between the displacement velocities obtained before and after SVR-based integration, as shown in Table 4.7, was applied to validate integration-derived displacement for each dataset (i.e., TSX, CSK, and S1) separately. Figure 4.23 represents a comparison of the differences in measured displacement velocities of the three datasets' boxplots.

Mean, median, $RMSE$, and standard deviation of the displacement velocity differences were listed in Table 4.7. TSX provides a lower mean difference than the S1 and CSK, with values of 0.97, 1.19, and 3.61 mm/year, respectively. In addition, when compared to CSK and S1, TSX has the best standard deviation and $RMSE$ values.

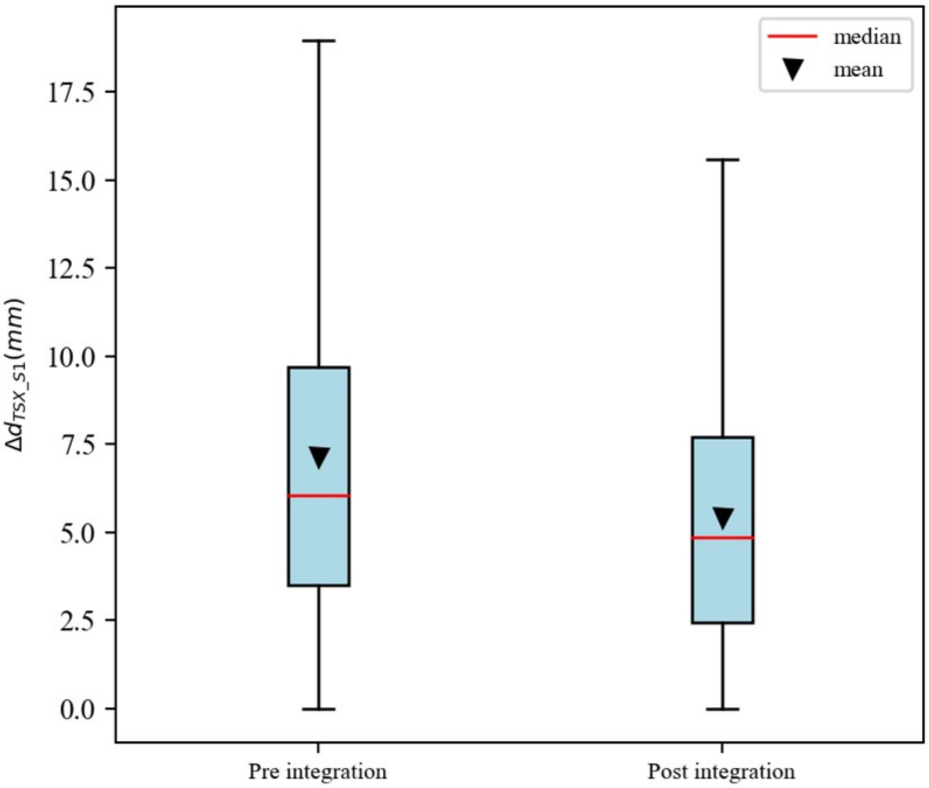

Figure 4.22: Box-plots of (Δd_{TSX-S1}) before and after applying the SVM-based integration method.

Table 4.7: Cross-validation for each dataset before and after SVM-based integration

Evaluation index (mm/year)/ Satellites	TSX	CSK	S1
Mean	0.97	1.19	3.61
STD	0.71	1.1	3.28
Median	0.93	0.78	2.31
$RMSE$	1.53	1.42	4.28

These $RMSE$ values elucidate that the TSX results were better than the CSK and S1 results. This could be attributed to the larger number of TSX interferograms involved in the integration process than the number of interferograms involved with CSK and S1.

Third, the results from different S1 datasets generated from different frames were

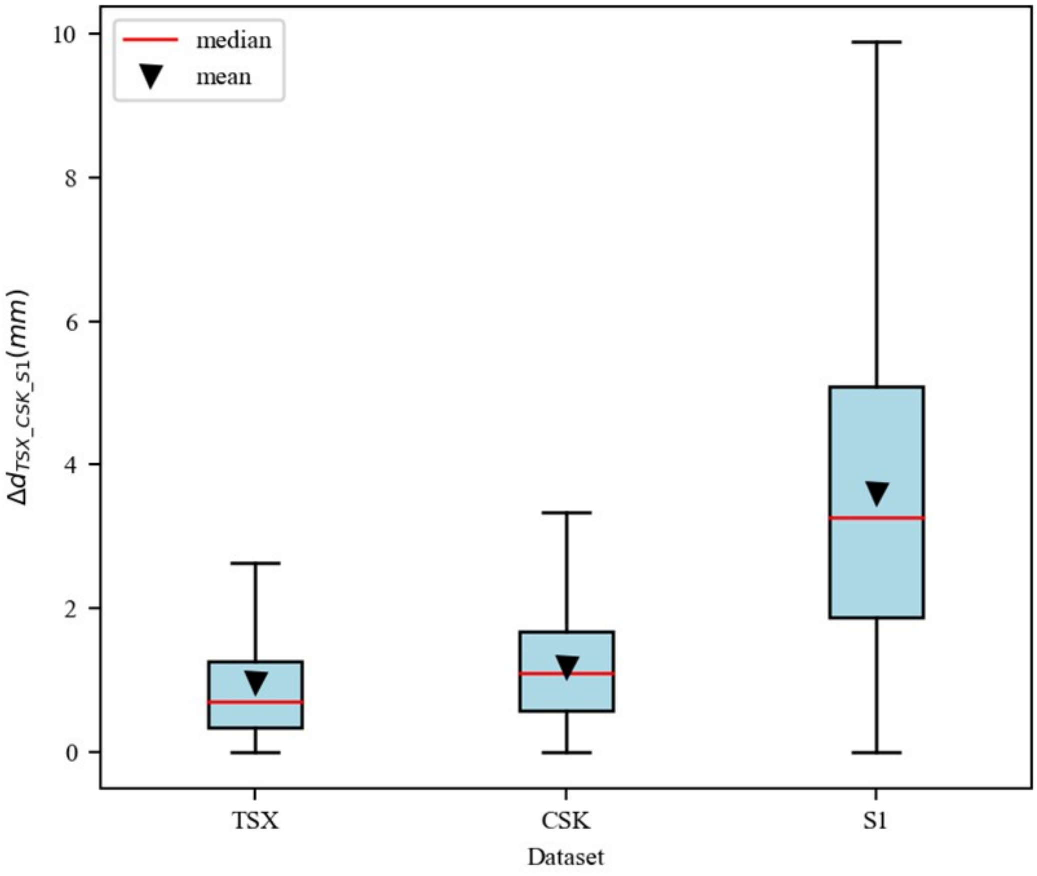

Figure 4.23: Box plots of the difference between AAD from TSX, CSK, and S1 before and after the SVM-based integration.

cross-validated as [139, 140] to study the effect of the SVM-based integration on the relation between different frames of S1 datasets as in Table 4.8. The standard deviations and $RMSE$ of the differences between the three frame datasets before and after integration are determined.

The $RMSE$ values are 5.60, 9.02, 10.35, and 1.43, 2.29, 2.05, and the standard deviations are 3.30, 5.91, 6.58, and 0.75, 1.54, 1.60 mm/year before and after integration, respectively, demonstrating excellent improvements among the results after applying the ML-based integration method. Figure 4.24 represents a comparison of the differences in measured displacement velocities of the Frame datasets' boxplots.

Table 4.8: standard deviations and $RMSE$ of the differences between the three frame datasets before and after integration

Evaluation index (mm/year)/ Frames	67-68		68-69		69-70	
	Pre	Post	Pre	Post	Pre	Post
Mean	4.52	1.21	6.80	1.70	7.99	1.29
Median	3.98	1.14	5.12	1.44	6.60	0.76
STD	3.30	0.75	5.91	1.54	6.58	1.60
$RMSE$	5.60	1.43	9.02	2.29	10.35	2.05

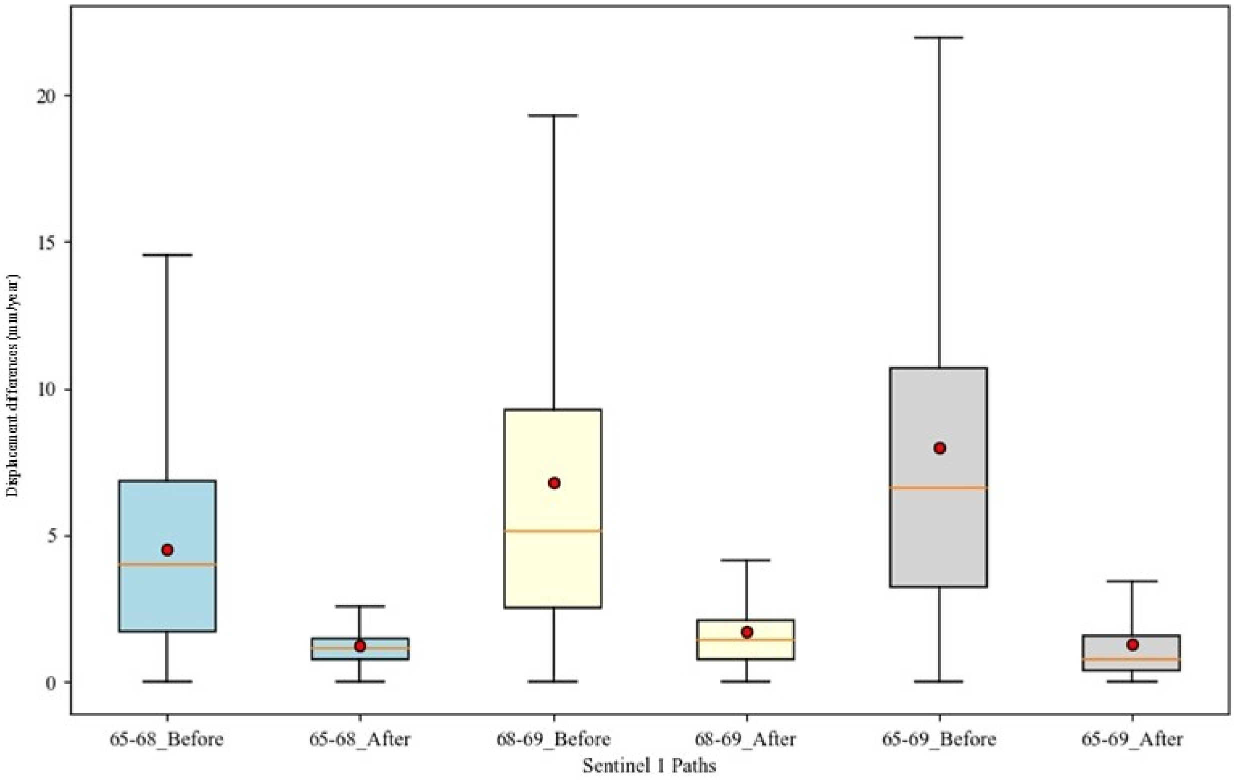

Figure 4.24: : Box plots of the difference between AAD from S1 Different Frames before and after the SVM-based integration.

4.2.4 Discussion

4.2.4.1 SVM for Multi-Sensor SAR Data Integration

The proposed framework primarily relies on SVR to integrate multi-satellite SAR data. SVR is rooted in statistical learning theory and offers several key advantages:

(1) It employs a learning method derived from the structural risk minimization principle, which balances regression accuracy with the complexity of the regression hyperplane; (2) It transforms real-world problems into a high-dimensional feature space, enabling nonlinear relationships to be represented using linear operators; (3) The model is solvable through convex quadratic programming, which theoretically guarantees a global optimal solution; (4) The regression function is determined by a few support vectors rather than the entire sample set, effectively overcoming the curse of dimensionality [141].

Our method operates as a post-processing step, meaning it does not require simultaneous handling of hundreds of differential SAR interferograms. Instead, it leverages recent advancements in generating LOS displacements. Integrating multi-satellite deformation components is highly dependent on the quality of LOS displacement information and the identification of highly coherent targets common to all datasets. Any disturbances in the LOS displacement can be estimated and filtered out before integration, preventing error propagation during the process. Our experimental results indicate that the ML-based approach performs effectively, with integrated displacements determined to sub-millimeter-level precision, comparable to those derived from individual LOS displacements. Therefore, the proposed method is expected to be particularly useful in investigating geological and geophysical processes where precise deformation discrimination is crucial.

4.2.4.2 Land Subsidence Based on Multi-sensor SAR Data

The number of satellite data vendors has been increasing, offering access to the latest C, X, and L-band SAR imagery from sensors like RADARSAT-2, S1A, ALOS-2, TSX, Tandem-X, and the CSK constellation, as well as from earlier SAR sensors such as ENVISAT and ERS. This expansion makes it possible to monitor surface displacements on scales ranging from regional levels to small structures. In this chapter, three distinct SAR datasets—TSX, CSK, and S1—were employed to study long-term ground subsidence.

From a frequency perspective, the C-band excels in displacement monitoring, while shorter wavelength and lower frequency bands like the X-band provide broader coverage of natural regions and reduce temporal decorrelation. These satellites have captured data over extended periods, enabling the tracking of long-term deformation. However, the uneven number of images and varying imaging characteristics present challenges in performance assessment. Despite this, the short revisit periods of TSX and S1 allowed for the observation of short-term land deformations, often due to human activities. Additionally, the overlap among the three datasets supports the integration of multi-sensor InSAR results.

Moreover, the cross-heading tracks of TSX and CSK images detected deformation on both sides, demonstrating that these tracks enhance displacement determination in the study area. In conclusion, the integration of multi-sensor SAR data demonstrates the feasibility of continuous deformation surveillance, providing a comprehensive approach to monitoring ground subsidence.

4.2.4.3 Local reclamation settlement, possible causes, and implications

The natural consolidation of reclamation fill is driven by three main mechanisms: (a) primary consolidation, which occurs within three years after reclamation; (b) long-term secondary compression of the alluvial clay deposits beneath the reclamation; and (c) creep within the reclamation fill, which can continue for over 40 years after reclamation. According to Ma et al. [142], variability in the fill material can affect the uniformity of consolidation, leading to uneven settlement. Ground deformation in these areas is influenced by the interaction between geological formations and human activities, which often reinforce each other.

The study area is comprised of granite, alluvium/colluvium, and reclaimed land. Granite, an intrusive igneous rock, is relatively stable, while the surrounding reclaimed land is less stable. Previous research has identified ground displacement in reclaimed areas of Hong Kong [16]. Human activities, such as the extensive underground train system in the western corridor, also contribute to ground displacement. Instances of sinking and building cracks have been documented by Qin and Perissin [2]. Therefore, the interaction between geological structures and subterranean projects likely contributes to the concentrated ground displacement observed in this region.

Long-term, large-scale subsidence poses significant risks, including increased flooding and saltwater intrusion due to rising sea levels [143]. Additionally, small-scale subsidence is a growing threat to buildings and infrastructure. This type of subsidence is more hazardous because it often occurs in densely populated areas, spreads widely, is difficult to detect, happens rapidly, and has complex causes [142]. Local governments are increasingly concerned about the substantial impacts of small-scale subsidence.

Validation of the developed approach demonstrated sub-millimeter-level accuracy in integrating multi-satellite SAR datasets. This approach enables the sequential integration of interferograms from different sensors and viewing orientations as they become available, resulting in 1-D displacements at each SAR interferogram time. A key advantage of this method is its ability to achieve significantly higher observation resolution by combining measurements from various radar sensors.

Therefore, the multi-satellite SAR-ML-based integration method shows promise in analyzing geological and geophysical processes. However, further in-depth evaluations are necessary to fully understand and assess the potential of the proposed method. This includes testing the approach with a similar number of images from each SAR satellite and applying it in various situations. Additionally, utilizing multi-platform SAR data to retrieve a multi-dimensional deformation map could be effective for monitoring deformation anomalies.

Moreover, the developed methodology maintains the high resolution of TSX and CSK while leveraging S1's superior monitoring capability and reducing the monitoring cycle. Given that Hong Kong's Kowloon district is one of the city's most densely populated areas, the results obtained through this approach are a valuable resource for disaster prevention, urban planning, and land reclamation efforts in the region.

4.2.4.4 Comparison with Previous Studies

In the absence of field measurements, the key findings of this research were compared with previous studies in the area, particularly two significant works that utilized InSAR data during the study period.

First, Qin et al. [2] analyzed ground displacement in the Hong Kong urban area using the PSI technique. Their study utilized 73 TSX and TDX images spanning October 2008 to September 2012. The PSI processing produced a line-of-sight LOS displacement velocity map, revealing an overall velocity close to zero in most regions, with localized variations ranging from -10 mm/year to 5 mm/year.

Notably, several locations within the western corridor (Figure 4.25) exhibited displacement trends exceeding -5 mm/year, primarily in areas situated on reclaimed land and near ongoing underground/ground construction sites. These displacement patterns suggest that both geological factors and human activities contributed to ground movement in these areas.

To assess the accuracy of the PSI technique, a corner reflector validation test was conducted. Manually adjusted reflectors were used to compare actual displacement values with PSI-derived results. A linear regression analysis between surveyed and PSI-derived values demonstrated a high correlation, with an RMSE of 1.20 mm, confirming that the PSI technique can achieve millimeter-level accuracy.

To compare this study with our results, a mean vertical displacement velocity map in Figure 4.26 was generated by extracting the vertical displacement values for the period from 2008 to 2012 from the results generated after applying the ML-based integration process.

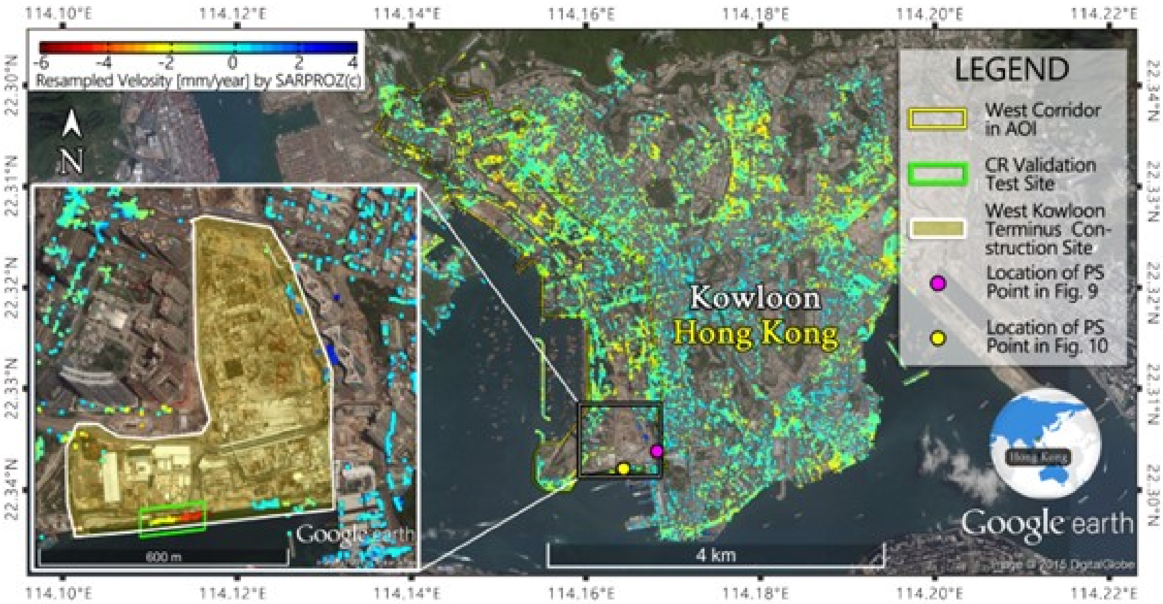

Figure 4.25: The annual velocity of the displacement map for PS points located in the Hong Kong urban area [2].

This map shows an overall velocity close to zero in most of the regions with partial regions varying from −11 mm/year to 6 mm/year. In particular, a number of spots inside the west corridor shown in Figure 7 show some displacement trends that exceed −6 mm/year; From the comparison, it is noted that the displacement behavior and magnitudes computed from our results closely match previous research in this area.

Seconed, Songbo et al.[3] investigate deformation caused by the underground construction of the To Kwa Wan (TKW) station in Hong Kong using an improved MT-InSAR method.

Multi-platform SAR datasets from TerraSAR-X, COSMO-SkyMed, and Sentinel-1A are utilized to retrieve comprehensive ground and building deformation for stability assessment. The results are validated through cross-comparison between SAR datasets, revealing both spatial and temporal variations in ground deformation. Figure 4.27 presents the deformation rate maps for individual SAR datasets. Figure 4.27 a shows ground deformation along the coastal areas of the Kowloon Peninsula, as

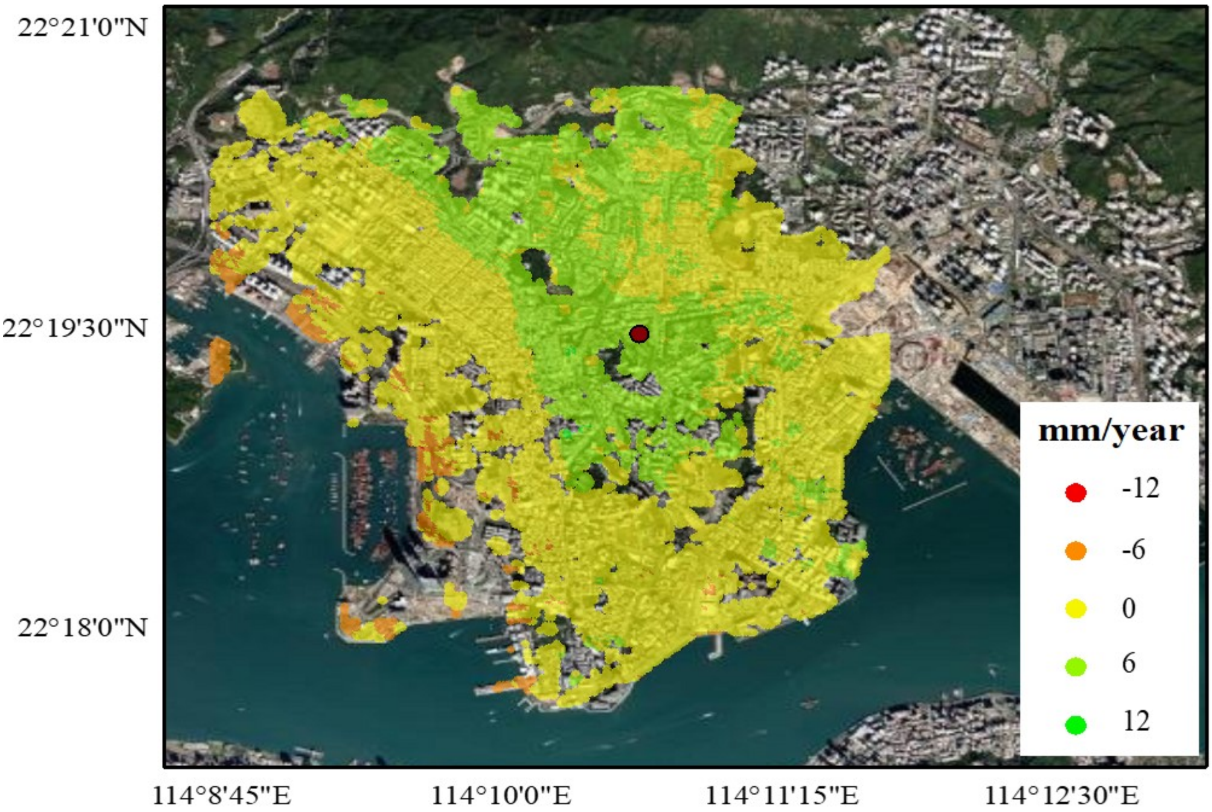

Figure 4.26: The mean vertical displacement velocity map from 2008 to 2012.

detected by TerraSAR-X (TSX) data from 2008 to 2017, with an annual deformation rate ranging from -10 to 10 mm/yr. Figure 4.27b, derived from COSMO-SkyMed (CSK) data, highlights significant deformation in the Kowloon Peninsula, with a maximum deformation rate of -15 to 15 mm/yr. Figure 4.27c, based on Sentinel-1A data, indicates relatively mild ground deformation across the peninsula. Among these datasets, deformation is primarily concentrated along the western corridor of the Kowloon Peninsula.

For comparison with the study by Songbo et al.[3], the mean displacement velocity maps for the TSX, CSK, and S1 SAR datasets were extracted from the integration results, as shown in Figure 4.28.

The TSX SAR data (2008–2017) reveal ground deformation along the western corridor of the Kowloon Peninsula, with a mean displacement velocity ranging from -10

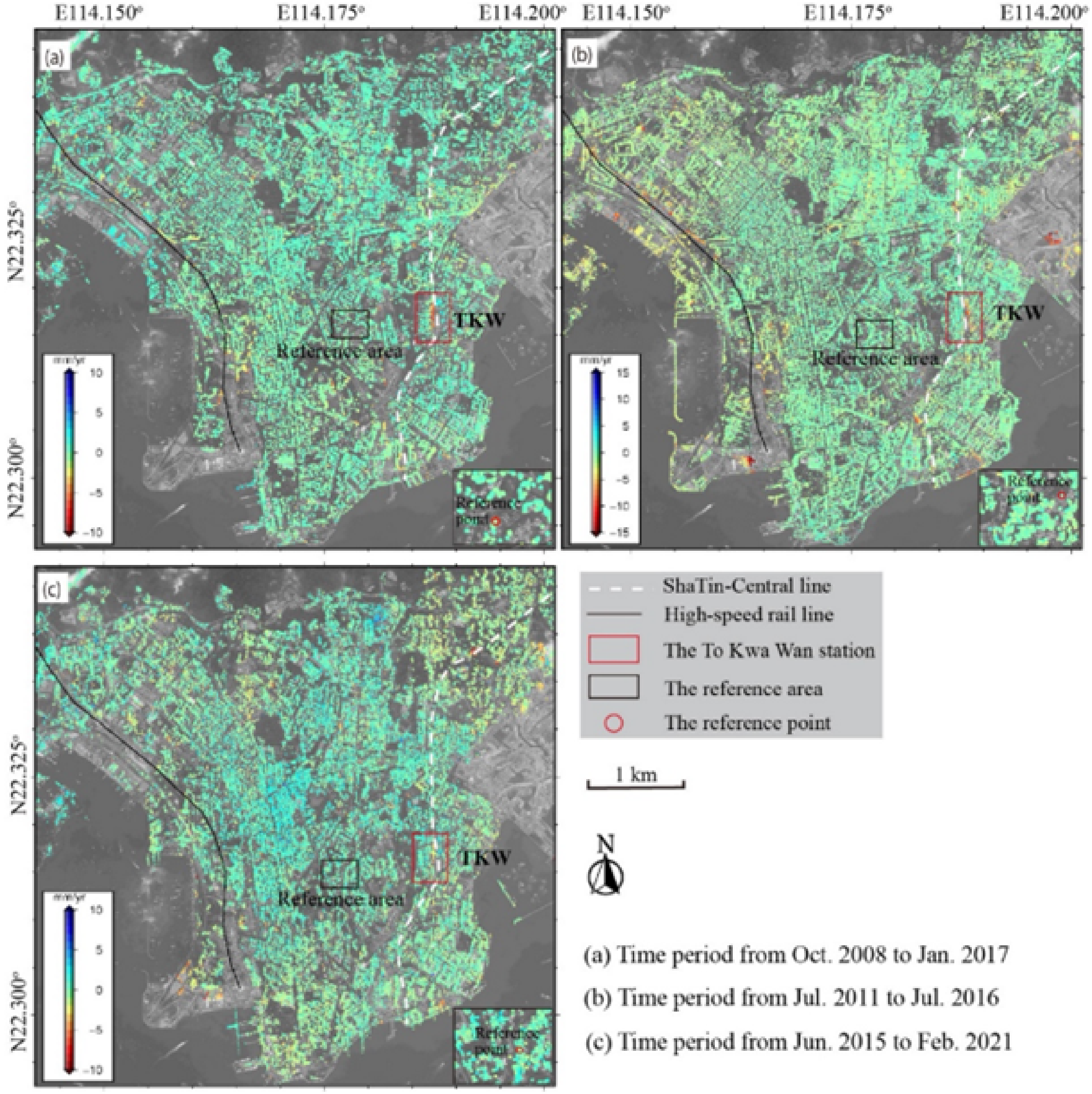

Figure 4.27: LOS deformation rate maps of the Kowloon Peninsula from (a) TSX (20081025-20170125), (b) CSK (20110731-20160728), and (c) Sentinel-1A (20150615-20210214) datasets. (Background image: Google Maps satellite image) [3].

to 10 mm/yr (Figure 4.28a). The CSK dataset shows a deformation rate ranging from −5 to 10 mm/yr (Figure 4.28b), while the S1 dataset indicates relatively mild deformation across the Kowloon Peninsula, with localized rates ranging from −15 to 10 mm/yr (Figure 4.28c). Across all three datasets, ground deformation is primarily

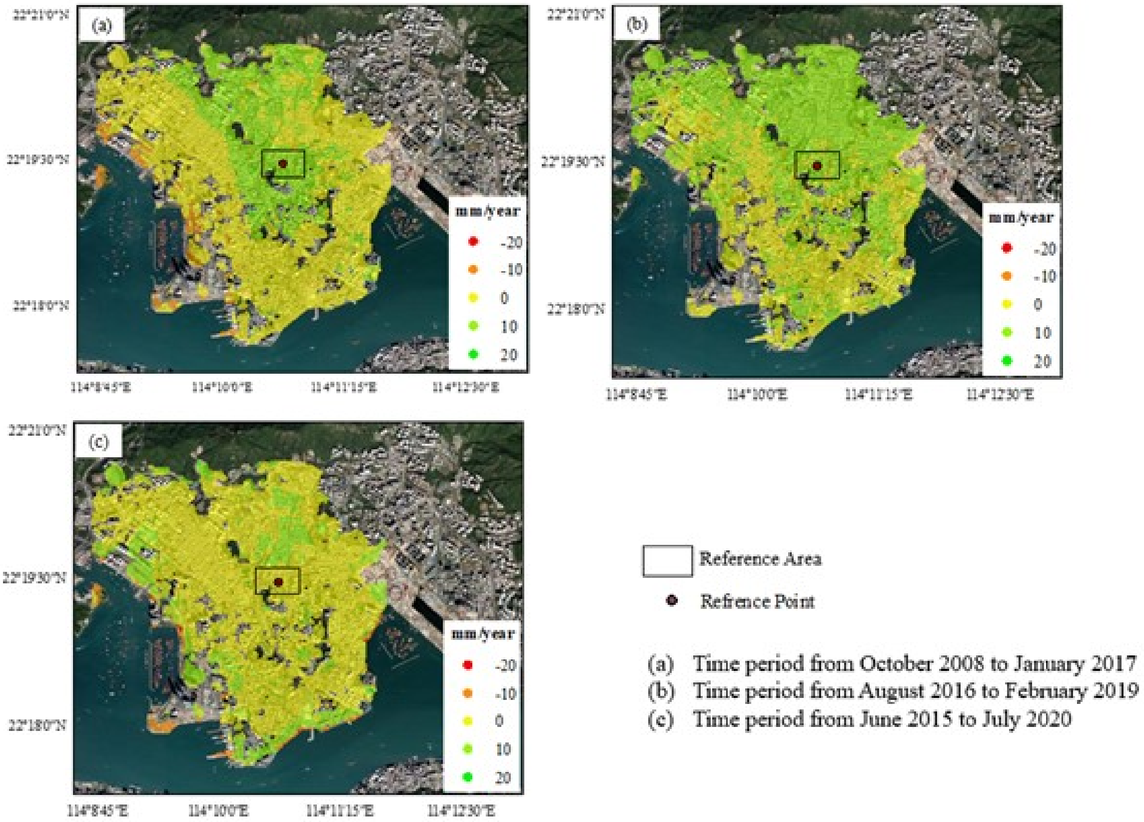

Figure 4.28: The mean displacement velocity maps for the TSX, CSK, and S1 SAR datasets after applying the integration.

concentrated along the western corridor of the Kowloon Peninsula.

From the comparison, it is observed that the displacement patterns and magnitudes are derived from TSX and S1 closely align with previous research in the area. However, the results from the CSK dataset show discrepancies, likely due to differences in the study period between the two studies.

4.3 Comparision between the two case studies

The effectiveness of the integration method for multi-satellite SAR data varies between Almokattam, Egypt, and Kowloon, Hong Kong, due to differences in geological stability, environmental conditions, and displacement characteristics. Almokattam is characterized by unstable limestone formations prone to landslides and human-induced excavations, leading to abrupt and localized vertical displacement. These sudden changes can cause phase decorrelation and inconsistencies when integrating SAR datasets from different sensors and periods. Additionally, the arid climate results in fewer seasonal variations, which, while reducing temporal decorrelation, limits the availability of natural coherence points over time. In contrast, Kowloon's displacement is more gradual and widespread, primarily due to land reclamation and underground infrastructure development. The steady nature of this deformation improves temporal coherence, making the integration process smoother. However, Kowloon's humid subtropical climate, with seasonal rainfall and typhoon-induced soil compaction, introduces short-term fluctuations that must be accounted for during SAR data fusion. The presence of well-maintained urban infrastructure in Kowloon also enhances the reliability of multi-sensor integration by providing consistent high-coherence scatterers. Overall, while both sites pose distinct challenges, the integration method is more effective in Kowloon due to its stable displacement trends and higher coherence, whereas Almokattam's abrupt ground failures make multi-temporal SAR integration more complex and less predictable. To explain this, a detailed comparision of the geological and environmental difference between the two case studies were made with thier impact on the vertical displacement patterns and the integration method's effectiveness as follows:

4.3.1 The Geological and Environmental Differences

- **Geological Characteristics**:
  - **Almokattam, Egypt**: Composed mainly of limestone and marl, making it prone to landslides and rockfalls due to fractures and weathering. High susceptibility to subsidence due to human activities like excavation and groundwater extraction.
  - **Kowloon, Hong Kong**: Composed mainly of granite and volcanic rocks,

providing greater stability. However, weathering processes and the presence of clay-rich soils contribute to slope instability and landslide susceptibility.

- **Topography**:
    - **Almokattam, Egypt**: Elevated plateau overlooking Cairo, with steep cliffs that increase the risk of rockfalls.
    - **Kowloon, Hong Kong**: Densely populated urban area with hilly terrain, featuring artificial land reclamation in coastal areas.
- **Seismic Activity**:
    - **Almokattam, Egypt**: Located in a relatively low to moderate seismic activity zone, though local faults and subsurface conditions can amplify ground movement effects.
    - **Kowloon, Hong Kong**: Subject to moderate seismic activity due to regional tectonic influences, including the active South China Sea subduction zones.
- **Climate and Weather Conditions**:
    - **Almokattam, Egypt**: Arid desert climate with minimal rainfall, reducing water-induced ground deformation but increasing the risk of soil shrinkage and subsidence.
    - **Kowloon, Hong Kong**: Humid subtropical climate with heavy seasonal rainfall, contributing to soil erosion, landslides, and water infiltration-induced ground deformation.
- **Human Impact**:
    - **Almokattam, Egypt**: Urban expansion, excavation, and groundwater extraction contribute significantly to land subsidence and instability.

  - **Kowloon, Hong Kong**: Rapid urbanization, infrastructure development, and underground construction projects (e.g., tunnels and metro systems) contribute to land movement and deformation.

- **Main Deformation Causes**:
  - **Almokattam, Egypt**: Subsidence due to excavation, underground construction, and water table fluctuations. Landslides triggered by weak rock formations.
  - **Kowloon, Hong Kong**: Subsidence due to artificial land reclamation from the sea and Human activities, such as the extensive underground train system.

4.3.2 How Geological and Environmental Differences Affect Vertical Displacement Measurements Between Almokattam and Kowloon

- **Geological composition and stability**:

  Almokattam is expected to show more localized and abrupt vertical displacement due to rockfalls and excavation, whereas Kowloon exhibits more uniform subsidence due to artificial ground settlement.

- **Climate and Weather Conditions**:

  Vertical displacement in Kowloon may fluctuate seasonally due to rainfall-induced soil compaction, while in Almokattam, it remains more gradual but linked to human activities.

- **Human Activities and Urbanization**:

  Kowloon experiences a slow, widespread subsidence due to land reclamation, while Almokattam is prone to localized, abrupt displacement from excavation and slope failure.

These differences help explain why Almokattam exhibits more sudden vertical shifts, while Kowloon experiences a more uniform, weather-dependent displacement pattern. Understanding these variations is crucial when interpreting InSAR-derived displacement maps and integrating multi-satellite SAR data.

4.3.3 Influence of Geological and Environmental Differences on the Effectiveness of the Integration Method

- **Impact of Geological Differences**:

  The localized and abrupt deformations in Almokattam pose challenges in maintaining data coherence across different sensors, whereas the gradual subsidence in Kowloon enhances integration consistency.

- **Impact of Climate and Environmental Conditions**:

  Almokattam benefits from stable seasonal conditions, while Kowloon experiences weather-related decorrelation, requiring additional corrections in integration.

- **Impact of Human Activities**:

  The erratic, abrupt displacement in Almokattam reduces integration effectiveness, while Kowloon's gradual deformation aligns better with long-term monitoring and integration models.

In conclusion, Kowloon's gradual, widespread subsidence enhances the effectiveness of the integration method, while Almokattam's abrupt, localized deformations introduce challenges, requiring advanced temporal filtering and adaptive weighting to improve integration accuracy.

Chapter 5

CONCLUSIONS AND OUTLOOK

This chapter summarizes the thesis, highlighting the key findings and research contributions. It begins by summarizing the main conclusions obtained from the research. Finally, the potential avenues for future research are identified, offering recommendations for further investigation and development based on the research outcomes.

5.1 Summary

This thesis introduced innovative solutions for integrating multi-satellite SAR data to retrieve time series displacement maps. The thesis started with presenting the main terms related to DInSAR technique as discussed in Chapter 2. After that, the multi-satellite SAR data integration was proposed based on two approaches: adaptation of traditional SBAS and utilization of machine learning, particularly, SVR.

In part I, the SAR data integration was performed by adaptation of the traditional multi-satellite SBAS based on TSVD. The proposed approach consists of three stages to integrate both temporally overlapping and temporally gapped multi-satellite SAR data. First, SAR data tracks have been processed individually. Then, the unwrapped phases have been geocoded and resampled at the high coherence points. Finally, the proposed multi-satellite SBAS has been employed to retrieve the vertical time series displacement maps using TSVD and least squares. The experimental design has involved 20 years of ERS, ENVISAT ASAR, and S1A data of Almokattam City in the Arab Republic of Egypt. The cross-validation results showed that the proposed approach enables a comprehensive interpretation of the deformation behavior within the study area. The main research findings include:

- The temporally overlapped and gapped DInSAR-derived vertical displacement values from ENVISAT, ERS, and S1 have been integrated based on MMSBAS.
- The proposed approach is the first to integrate 20 years of multisatellite SAR data sets in the city of Almokattam.
- The western part of Almokattam city is specifically prone to subsidence, where its rate reached -2.32 mm/year. This is consistent with the real ongoing subsidence observed during the study period.
- The results revealed a severe subsidence between 2000 and 2005, with rate reach to -59.5 mm/year and with a rate of -13.39 mm/year from 2004 to 2012. These

findings align with the documented historical subsidence incidents in 1993, 2000, 2002, 2004, and 2008.

- It is noted that there is an uplift in many places in Almokattam city especially in the eastern part with a displacement rate reach to 3.33 mm/year.
- Cross-validation results from S1 outperformed those from ENVISAT and ERS, with correlation coefficients of 0.92 for ERS, 0.97 for ENVISAT, and 0.99 for S1. Similarly, the root mean square errors (RMSE) were 1.92 mm for ERS, 1.66 mm for ENVISAT, and 1.19 mm for S1. This improved performance is primarily due to the larger number of images and the finer temporal resolution of the S1 satellite data.
- In general The validation results showed a consistency overall displacement velocity pattern before and after the integration, which indicates that the MMS-BAS approach performs effectively.
- In comparison to previous studies applied in the study area [136, 137], the proposed methodology has demonstrated sub-millimeter accuracy in estimating subsidence and its trend.
- Integrating multi-satellite InSAR has optimized their complementary nature which enables comprehensive coverage. Thus, improving the displacement results.

Part II explores SVR for integrating multi-sensor DInSAR data. The proposed framework addresses the challenge of processing large datasets by efficiently handling massive data volumes. As a post-processing approach, it streamlines the analysis of differential SAR interferograms, eliminating the need to simultaneously process hundreds of these complex structures. Furthermore, the framework facilitates the seamless integration of multi-satellite SAR data, reducing the need for extensive hyper-parameter adjustments, thus significantly improving the overall analysis efficiency and flexibility.

This approach employs SVR with multiple independent variables to integrate vertical displacement data from various sensors over common high-coherence points. Vertical displacements are computed from individual datasets and then integrated using the SVR algorithm. Experiments included high-resolution CSK and TSX images, along with a smaller monitoring cycle using S1 data over Kowloon City in Hong Kong. This research concluded that:

- The experimental results indicated that there is land subsidence in the west corridor of the Kowloon district, which corridor exceeded -12 mm/year.
- The subsidence of the land is mainly due to land reclamation and ongoing underground and ground construction projects.
- Human activities, such as the extensive underground train system in the western corridor, also contribute to ground displacement.
- C-band data offer superior capabilities for monitoring displacements, while shorter wavelengths and lower frequencies (e.g., X-band) provide more comprehensive coverage of natural areas and benefit from lower temporal correlation, allowing these satellites to capture data over longer periods for tracking long-term deformation.
- The short revisit times of TSX and S1 enabled observation of short-term land deformations due to human activities.
- The temporal overlap of the datasets supported effective multi-sensor InSAR integration.
- The cross-track geometries of the TSX and CSK images facilitated the identification of deformation on both sides of the features of interest, highlighting the importance of integration.

- TSX results outperformed those of CSK and S1, with standard deviation (STD) values of 0.71 mm/year for TSX, 1.1 mm / year for CSK and 3.26 mm / year for S1. Similarly, the root mean square error (RMSE) values were 1.53 mm/year for TSX, 1.42 mm/year for CSK, and 4.28 mm/year for S1. This improved performance is likely attributed to the larger number of TSX interferograms incorporated into the integration process compared to those used for CSK and S1.
- The displacement behavior and magnitudes computed from the proposed integration method closely match previous research in this area [2, 4], indicating the effectivity of the ML-based integration method.

5.2 Conclusions

- This thesis introduced solutions for integrating multi-satellite SAR data to retrieve long-term vertical displacement rate maps by benefiting from the advantages of each satellite individually.
- The multi-satellite SAR data integration was based on two approaches: adaptation of traditional SBAS MMSBAS and utilization of machine learning, particularly multiple independent variables SVR (ML-based integration).
- The focus on vertical displacement in this research is motivated by several key factors related to the nature of the deformation process, the characteristics of InSAR measurements, and the challenges of multi-sensor data integration.
  - **Relevance to the Study Area and Deformation Type:** In many regions, including the two study areas considered in this work, deformation is predominantly vertical, often due to processes such as land subsidence, or land reclamation from the sea. Horizontal displacements, while present, are typically less significant or more challenging to isolate with InSAR, making vertical motion the primary concern.

  - **Data Constraints and Computational Efficiency:** Estimating both horizontal and vertical components requires additional processing steps, such as incorporating GNSS data or using multiple acquisition geometries, which may not always be available. By restricting the study to vertical displacement, the research optimizes data usage while maintaining computational efficiency.
  - **Suitability for Multi-Sensor Integration:** Integrating SAR data from multiple satellites introduces challenges due to differences in sensor wavelengths, orbital geometries, and acquisition times. Vertical displacement is generally more consistent across different sensors, reducing cross-sensor biases and making the integration process more reliable. This choice enhances the accuracy and robustness of the final displacement maps.

- Our frameworks operate as a post-processing step, meaning that:
  - It does not require simultaneous handling of hundreds of differential SAR interferograms.
  - Any disturbances in the LOS displacement can be estimated and filtered out before integration, preventing error propagation during the process.
  - It reduces the need for extensive hyper parameter adjustments, thus significantly improving the overall analysis efficiency and flexibility.

- The proposed methods offer several general advantages compared to existing literature:
  - It does not require an external displacement model to bridge time gaps between datasets;
  - A relatively small number of SAR scenes are used;
  - It exploits the strengths of both PS and DS techniques to enhance the density of high-coherence points.

- Our integration approaches ensure a robust and temporally continuous deformation history, even in the presence of missing SAR acquisitions.
    - The MMSBAS method mitigates the impact of time gaps between SAR images by constructing a network of interferograms and applying temporal interpolation through the TSVD inversion process.
    - In the ML-based approach, ground displacement velocity is integrated instead of direct displacement values. By utilizing velocity rather than displacement, measurements are standardized across different datasets, facilitating the seamless merging of time-gapped data from multiple satellites.
- The Machine Learning role in integrating multi-satellite SAR datasets:
    - Assigning weights to displacement data in the integration process.
    - Reducing the remaining cross-sensor biases.
    - Automating the integration process.
    - Handling of large and complex datasets.
    - Improving accuracy of integrated displacement maps.

5.3 Outlook

The future work of this thesis research can be summarized in the following points:

- Conduct a thorough evaluation of the proposed methodology by incorporating field measurements, such as GPS and leveling, to validate and enhance the accuracy of the results.
- Extend the multi-satellite SBAS to combine DInSAR-driven 3D displacement time series. However, the success of this extension hinges on the validity of additional ground deformation signals from field measurments, such as GPS

or leveling, and the availability of both ascending and descending SAR flight paths.

- Expanding the dataset with more recent SAR acquisitions from multiple SAR satellites to enhance the temporal and spatial coverage and providing a more comprehensive understanding of ground displacement trends.
- Employ ensemble learning algorithms to monitor the long-term earth surface displacement. These ML algorithms involve training multiple machine learning models and combining their predictions to improve accuracy and robustness.
- It would be promising to employ deep learning techniques in multi-satellite SAR data integration. Deep learning algorithms have various advantages, including:
    - They provide a more automated integration process.
    - They can integrate SAR images from preprocessing to integrated displacement estimation in a single pipeline.
    - They effectively integrate data from multiple satellites with different resolutions, wavelengths (C-band, L-band, X-band), and temporal baselines.
    - They can predict future displacement trends and potential hazards (e.g., landslides, subsidence) using past DInSAR data.
    - They can capture long-term temporal dependences in ground displacement data.
    - They can process large-scale, high-dimensional DInSAR datasets efficiently using GPUs and cloud computing.
    - They can denoise and correct phase unwrapping errors directly from data and reduce atmospheric artifacts and noise.

In order to utilize deep learning (DL) algorithms to generate the 3D displacement maps, there were some challenges to apply such techniques:

- They require a large data annotation, which is not straightforward for displacement data.
- They often require GPUs or TPUs for training large networks, therefore requiring a high computational cost.

Consequently, in this thesis, machine learning techniques particularly SVR, is employed in InSAR data integration. Compared to DL algorithms, machine learning techniques do not require data annotation, and they have relatively low computational cost which make them faster and simpler.

References

[1] ArcGIS Services. Hong kong geology feature service, 2024. URL `https://services3.arcgis.com/6j1KwZfY2fZrfNMR/arcgis/rest/services/Hong_Kong_Geology/FeatureServer`. Accessed: 2024-07-22.

[2] Yuxiao Qin and D. Perissin. Monitoring ground subsidence in hong kong via spaceborne radar: Experiments and validation. *Remote Sensing*, 7:10715–10736, 08 2015. doi: 10.3390/rs70810715.

[3] Songbo Wu, Bochen Zhang, Hongyu Liang, Chisheng Wang, Xiaoli Ding, and Lei Zhang. Detecting the deformation anomalies induced by underground construction using multiplatform mt-insar: A case study in to kwa wan station, hong kong. *IEEE Journal of Selected Topics in Applied Earth Observations and Remote Sensing*, 14:9803–9814, 2021. doi: 10.1109/JSTARS.2021.3113672.

[4] Songbo Wu, Bochen Zhang, Hongyu Liang, Chi Wang, Xiaoli Ding, and Lei Zhang. Detecting the deformation anomalies induced by underground construction using multiplatform mt-insar: A case study in to kwa wan station, hong kong. *IEEE Journal of Selected Topics in Applied Earth Observations and Remote Sensing*, PP:1–1, 09 2021. doi: 10.1109/JSTARS.2021.3113672.

[5] Andrew K. Gabriel, Richard M. Goldstein, and Howard A. Zebker. Mapping small evaluation changes over large areas: Differential radar interferometry. *jgr*, 94(B7):9183–9191, July 1989. doi: 10.1029/JB094iB07p09183.

[6] Richard Bamler and Philipp Hartl. Synthetic aperture radar interferometry. *Inverse Problems*, 14(4):R1, aug 1998. doi: 10.1088/0266-5611/14/4/001. URL `https://dx.doi.org/10.1088/0266-5611/14/4/001`.

[7] Roland Bürgmann, Paul A. Rosen, and Eric J. Fielding. Synthetic aperture radar interferometry to measure earth's surface topography and its deformation. *Annual Review of Earth and Planetary Sciences*, 28(1):169–209, 2000. doi: 10.1146/annurev.earth.28.1.169.

[8] Ramon Hanssen. *Radar Interferometry Data Interpretation and Error Analysis*, volume 2. Springer Netherlands, 01 2001. ISBN 978-0-7923-6945-5. doi: 10.1007/0-306-47633-9.

[9] Didier Massonnet and Kurt Feigl. Radar interferometry and its application to changes in the earth's surface. rev. geophys. 36, 441-500. *Reviews of Geophysics*, 36, 11 1998. doi: 10.1029/97RG03139.

[10] Didier Massonnet, Marc Rossi, César Carmona-Moreno, Frederic Adragna, Gilles Peltzer, Kurt Feigl, and Thierry Rabaute. The displacement field of the landers earthquake mapped by radar interferometry. *Nature*, 364:138–142, 07 1993. doi: 10.1038/364138a0.

[11] Howard Zebker, Paul Rosen, Richard Goldstein, Andrew Gabriel, and Charles Werner. On the derivation of coseismic displacement fields using differential radar interferometry: The landers earthquake. *Journal of Geophysical Research Atmospheres*, 99, 11 1994. doi: 10.1029/94JB01179.

[12] Zhong Lu, Daniel Dzurisin, Charles Wicks Jr., John Power, Ohig Kwoun, and Russell Rykhus. *Diverse Deformation Patterns of Aleutian Volcanoes from Satellite Interferometric Synthetic Aperture Radar (InSAR)*, pages 249–261. American Geophysical Union (AGU), 2007. ISBN 9781118666371. doi: https://doi.org/10.1029/172GM18.

[13] Richard M. Goldstein, Hermann Engelhardt, Barclay Kamb, and Richard M. Frolich. Satellite radar interferometry for monitoring ice sheet motion: Application to an antarctic ice stream. *Science*, 262(5139):1525–1530, 1993. doi: 10.1126/science.262.5139.1525.

[14] Qian Sun, Lei Zhang, Xiaoli Ding, Jun Hu, and Hongyu Liang. Investigation of slow-moving landslides from alos/palsar images with tcpinsar: A case study of oso, usa. *Remote Sensing*, 7(1):72–88, 2015. ISSN 2072-4292. doi: 10.3390/rs70100072. URL `https://www.mdpi.com/2072-4292/7/1/72`.

[15] Wu Zhu, Qin Zhang, XiaoLi Ding, Chaoying Zhao, Chengsheng Yang, Feifei Qu, and Wei Qu. Landslide monitoring by combining of cr-insar and gps techniques. *Advances in Space Research*, 53(3):430–439, 2014. ISSN 0273-1177. doi: https://doi.org/10.1016/j.asr.2013.12.003.

[16] Xiaoli Ding, G.X. Liu, Zhiwei, Zhan-Lin Li, and Y.Q. Chen. Ground subsidence monitoring in hong kong with satellite sar interferometry. *Photogrammetric Engineering and Remote Sensing*, 70:1151–1156, 10 2004. doi: 10.14358/PERS.70.10.1151.

[17] Lei Zhang, Zhong Lu, Xiaoli Ding, Hyung sup Jung, Guangcai Feng, and Chang-Wook Lee. Mapping ground surface deformation using temporarily coherent point sar interferometry: Application to los angeles basin. *Remote Sensing of Environment*, 117:429–439, 2012. ISSN 0034-4257. doi: https://doi.org/10.1016/j.rse.2011.10.020. Remote Sensing of Urban Environments.

[18] Howard A. Zebker, Paul A. Rosen, and Scott Hensley. Atmospheric effects in interferometric synthetic aperture radar surface deformation and topographic maps. *jgr*, 102(B4):7547–7563, 4 1997. doi: 10.1029/96JB03804.

[19] H.A. Zebker and J. Villasenor. Decorrelation in interferometric radar echoes.

IEEE Transactions on Geoscience and Remote Sensing, 30(5):950–959, 1992. doi: 10.1109/36.175330.

[20] Xiaoli. Ding, Zhi-wei. Li, Jian-jun. Zhu, Guang-cai. Feng, and Jiang-ping Long. Atmospheric effects on insar measurements and their mitigation. *Sensors*, 8(9): 5426–5448, 2008. doi: 10.3390/s8095426.

[21] Yanan Du, Lei Zhang, Guangcai Feng, Zhong Lu, and Qian Sun. On the accuracy of topographic residuals retrieved by mtinsar. *IEEE Transactions on Geoscience and Remote Sensing*, PP:1–13, 11 2016. doi: 10.1109/TGRS.2016.2618942.

[22] Hongrui Ren and Xiaoman Feng. Calculating vertical deformation using a single insar pair based on singular value decomposition in mining areas. *International Journal of Applied Earth Observation and Geoinformation*, 92:102115, 2020. ISSN 1569-8432. doi: https://doi.org/10.1016/j.jag.2020.102115.

[23] Mimi Peng, Chaoying Zhao, Qin Zhang, Zhong Lu, Lin Bai, and Weiming Bai. Multi-scale and multi-dimensional time series insar characterizing of surface deformation over shandong peninsula, china. *Applied Sciences*, 10(7), 2020. ISSN 2076-3417. doi: 10.3390/app10072294.

[24] Nico Adam, Bert Kampes, and Michael Eineder. Development of a scientific permanent scatterer system: Modifications for mixed ers/envisat time series. In *Proceedings of the 2004 Envisat & ERS Symposium (ESA SP-572)*, 01 2004.

[25] Mario Costantini, Salvatore Falco, Fabio Malvarosa, Federico Minati, Francesco Trillo, and Francesco Vecchioli. Persistent scatterer pair interferometry: Approach and application to cosmo-skymed sar data. *IEEE Journal of Selected Topics in Applied Earth Observations and Remote Sensing*, 7(7):2869–2879, 2014. doi: 10.1109/JSTARS.2014.2343915.

[26] A. Ferretti, C. Prati, and F. Rocca. Permanent scatterers in sar interferometry. *IEEE Transactions on Geoscience and Remote Sensing*, 39(1):8–20, 2001. doi: 10.1109/36.898661.

[27] Andy Hooper, Howard Zebker, Paul Segall, and Bert Kampes. A new method for measuring deformation on volcanoes and other natural terrains using insar persistent scatterers. *Geophyiscal Research Letters*, 31:1–5, 12 2004. doi: 10.1029/2004GL021737.

[28] A. Hooper, P. Segall, and H. Zebker. Persistent scatterer interferometric synthetic aperture radar for crustal deformation analysis, with application to volcán alcedo, galápagos. *Journal of Geophysical Research: Solid Earth*, 112(B7), 2007. doi: https://doi.org/10.1029/2006JB004763.

[29] B. M. Kampes and N. Adam. The STUN Algorithm for Persistent Scatterer Interferometry. In H. Lacoste and L. Ouwehand, editors, *Fringe 2005 Workshop*, volume 610 of *ESA Special Publication*, page 16, February 2006.

[30] P. Berardino, G. Fornaro, R. Lanari, and E. Sansosti. A new algorithm for surface deformation monitoring based on small baseline differential sar interferograms. *IEEE Transactions on Geoscience and Remote Sensing*, 40(11): 2375–2383, 2002. doi: 10.1109/TGRS.2002.803792.

[31] O. Mora, J.J. Mallorqui, and A. Broquetas. Linear and nonlinear terrain deformation maps from a reduced set of interferometric sar images. *IEEE Transactions on Geoscience and Remote Sensing*, 41(10):2243–2253, 2003. doi: 10.1109/TGRS.2003.814657.

[32] R. Lanari, O. Mora, M. Manunta, J.J. Mallorqui, P. Berardino, and E. Sansosti. A small-baseline approach for investigating deformations on full-resolution differential sar interferograms. *IEEE Transactions on Geoscience and Remote Sensing*, 42(7):1377–1386, 2004. doi: 10.1109/TGRS.2004.828196.

[33] Sergey Samsonov, Marco Kooij, and Kristy Tiampo. A simultaneous inversion for deformation rates and topographic errors of dinsar data utilizing linear least square inversion technique. *Computers & Geosciences*, 37:1083–1091, 08 2011. doi: 10.1016/j.cageo.2011.01.007.

[34] David Schmidt and Roland Burgmann. Time-dependent land uplift and subsidence in the santa clara valley, california, from a large interferometric synthetic aperture radar data set. *Journal of Geophysical Research*, 108, 09 2003. doi: 10.1029/2002JB002267.

[35] Alessandro Ferretti, Alfio Fumagalli, Fabrizio Novali, Claudio Prati, Fabio Rocca, and Alessio Rucci. A new algorithm for processing interferometric datastacks: Squeesar. *IEEE Transactions on Geoscience and Remote Sensing*, 49 (9):3460–3470, 2011. doi: 10.1109/TGRS.2011.2124465.

[36] Ning Cao, Hyongki Lee, and Hahn Chul Jung. A phase-decomposition-based psinsar processing method. *IEEE Transactions on Geoscience and Remote Sensing*, 54, 09 2015. doi: 10.1109/TGRS.2015.2473818.

[37] Gianfranco Fornaro, Simona Verde, Diego Reale, and Antonio Pauciullo. Caesar: An approach based on covariance matrix decomposition to improve multibaseline–multitemporal interferometric sar processing. *IEEE Transactions on Geoscience and Remote Sensing*, 53:2050–2065, 2015.

[38] Sami Samiei Esfahany, Joana Martins, Freek Van Leijen, and Ramon Hanssen. Phase estimation for distributed scatterers in insar stacks using integer least squares estimation. *IEEE Transactions on Geoscience and Remote Sensing*, 54: 1–17, 06 2016. doi: 10.1109/TGRS.2016.2566604.

[39] Stefan Gernhardt and Richard Bamler. Deformation monitoring of single buildings using meter-resolution sar data in psi. *ISPRS Journal of Photogrammetry and Remote Sensing*, 73:68–79, 09 2012. doi: 10.1016/j.isprsjprs.2012.06.009.

[40] Peifeng Ma and Hui Lin. Robust detection of single and double persistent scatterers in urban built environments. *IEEE Transactions on Geoscience and Remote Sensing*, 54:1–16, 11 2015. doi: 10.1109/TGRS.2015.2496193.

[41] Andy Hooper. A multi-temporal insar method incorporating both persistent scatterer and small baseline approaches. *Geophysical Research Letters*, 35(16), 08 2008. doi: 10.1029/2008GL034654.

[42] Andrea Monti Guarnieri and Stefano Tebaldini. On the exploitation of target statistics for sar interferometry applications. *IEEE Transactions on Geoscience and Remote Sensing*, 46(11):3436–3443, 2008. doi: 10.1109/TGRS.2008.2001756.

[43] Ramon Brcic, Alessandro Parizzi, Michael Eineder, Richard Bamler, and Franz Meyer. Estimation and compensation of ionospheric delay for sar interferometry. In *2010 IEEE International Geoscience and Remote Sensing Symposium*, pages 2908 – 2911, 08 2010. doi: 10.1109/IGARSS.2010.5652231.

[44] I. Baran, M. Stewart, and S. Claessens. A new functional model for determining minimum and maximum detectable deformation gradient resolved by satellite radar interferometry. *IEEE Transactions on Geoscience and Remote Sensing*, 43(4):675–682, 2005. doi: 10.1109/TGRS.2004.843187.

[45] Pablo Euillades, Leonardo Euillades, Antonio Pepe, Pietro Mastro, Francesco Falabella, Pasquale Imperatore, Yixian Tang, and Patricia Rosell. Recent advancements in multi-temporal methods applied to new generation sar systems and applications in south america. *Journal of South American Earth Sciences*, 111:103410, 2021. ISSN 0895-9811. doi: https://doi.org/10.1016/j.jsames.2021.103410.

[46] A. Pepe, Giuseppe Solaro, Fabiana Calo, and Claudio Dema. A minimum acceleration approach for the retrieval of multiplatform insar deformation time

series. *IEEE Journal of Selected Topics in Applied Earth Observations and Remote Sensing*, 9:1–16, 07 2016. doi: 10.1109/JSTARS.2016.2577878.

[47] Laurence Gray. Using multiple radarsat insar pairs to estimate a full three-dimensional solution for glacial ice movement. *Geophysical Research Letters - GEOPHYS RES LETT*, 38, 03 2011. doi: 10.1029/2010GL046484.

[48] Sverrir Gudmundsson, Freysteinn Sigmundsson, and Jens Carstensen. Three-dimensional surface motion maps estimated from combined interferometric synthetic aperture radar and gps data. *Journal of Geophysical Research*, 107, 10 2002. doi: 10.1029/2001JB000283.

[49] Jhen-Jia Hu, Zhiwei, Xiaoli Ding, Zhu Jian-Jun, Lei Zhang, and Qiji Sun. 3d coseismic displacement of 2010 darfield, new zealand earthquake estimated from multi-aperture insar and d-insar measurements. *Journal of Geodesy*, 86, 11 2012. doi: 10.1007/s00190-012-0563-6.

[50] Tim Wright, Barry Parsons, and Zhong Lu. Toward mapping surface deformation in three dimensions using insar. *Geophys. Res. Lett*, 31, 01 2004. doi: 10.1029/2003GL018827.

[51] Hu Jun, Xiaoli Ding, Zhiwei, Zhu Jian-Jun, Qian Sun, and Lei Zhang. Kalman-filter-based approach for multisensor, multitrack, and multitemporal insar. *Geoscience and Remote Sensing, IEEE Transactions on*, 51:4226–4239, 07 2013. doi: 10.1109/TGRS.2012.2227759.

[52] Sergey Samsonov and Nicolas d'Oreye. Multidimensional time-series analysis of ground deformation from multiple insar data sets applied to virunga volcanic province. *Geophysical Journal International*, 191:1095–1108, 12 2012. doi: 10.1111/j.1365-246X.2012.05669.x.

[53] Ling Chang, Rolf Dollevoet, and Ramon Hanssen. Monitoring line-infrastructure with multisensor sar interferometry: Products and performance

assessment metrics. *IEEE Journal of Selected Topics in Applied Earth Observations and Remote Sensing*, PP:1–13, 3 2018. doi: 10.1109/JSTARS.2018.2803074.

[54] A. Pepe, Giuseppe Solaro, and Claudio Dema. A minimum curvature combination method for the generation of multi-platform dinsar deformation time-series. In *FRINGE 2015, Proceedings of the workshop*, 05 2015. doi: 10.5270/Fringe2015.pp150.

[55] Qing Zhao, Guanyu Ma, Qiang Wang, Tianliang Yang, Min. Liu, Wei. Gao, Francesco. Falabella, Pietro. Mastro, and Antonio. Pepe. Generation of long-term InSAR ground displacement time-series through a novel multi-sensor data merging technique: The case study of the Shanghai coastal area. *ISPRS Journal of Photogrammetry and Remote Sensing*, 154:10–27, August 2019. doi: 10.1016/j.isprsjprs.2019.05.005.

[56] Dominique Derauw, d. 'Oreye Nicolas, Maxime Jaspard, Alberto Caselli, and Sergey Samsonov. Ongoing automated ground deformation monitoring of Domuyo - Laguna del Maule area (Argentina) using Sentinel-1 MSBAS time series: Methodology description and first observations for the period 2015-2020. *Journal of South American Earth Sciences*, 104:102850, December 2020. doi: 10.1016/j.jsames.2020.102850.

[57] Sergey Samsonov. Three-dimensional deformation time series of glacier motion from multiple-aperture dinsar observation. *Journal of Geodesy*, 93, 11 2019. doi: 10.1007/s00190-019-01325-y.

[58] Sergey Samsonov and Nicolas d'Oreye. Multidimensional small baseline subset (msbas) for two-dimensional deformation analysis: Case study mexico city. *Canadian Journal of Remote Sensing*, 43, 07 2017. doi: 10.1080/07038992.2017.1344926.

[59] Sergey Samsonov, Antoine Dille, Olivier Dewitte, François Kervyn, and Nicolas d'Oreye. Satellite interferometry for mapping surface deformation time series in one, two and three dimensions: A new method illustrated on a slow-moving landslide. *Engineering Geology*, 266:105471, 2020. ISSN 0013-7952. doi: https://doi.org/10.1016/j.enggeo.2019.105471.

[60] Ling Chang, Ramon F. Hanssen, and R. P.B.J. Dollevoet. Detection of railway infrastructure settlement using satellite sar interferometry. *Proceedings of the Second International Conference on Railway Technology: Research, Development and Maintenance*, 110, 2016. ISSN 1759-3433.

[61] Ling Chang and Ramon F. Hanssen. Functional model selection for insar time series. In *2016 IEEE International Geoscience and Remote Sensing Symposium (IGARSS)*, pages 3390–3393, 2016. doi: 10.1109/IGARSS.2016.7729876.

[62] Hongyu Liang, Wenbin Xu, Xiaoli Ding, Lei Zhang, and Songbo Wu. *Urban Sensing with Spaceborne Interferometric Synthetic Aperture Radar*, pages 345–365. Springer, 04 2021. ISBN 978-981-15-8982-9. doi: 10.1007/978-981-15-8983-6_21.

[63] Michele Martone. *Onboard Quantization for Interferometric and Multichannel Synthetic Aperture Radar (SAR) Systems.* PhD thesis, Deutsches Zentrum für Luft- und Raumfahrt (DLR), 11 2019.

[64] Lawrence P. Orwig, Alan D. Aronoff, Paul M. Ibsen, Harold D. Maney, James D. O'Brien, and Hugh D. Holt. Wide-area terrain surveying with interferometric sar. *Remote Sensing of Environment*, 53(2):97–108, 1995. ISSN 0034-4257. doi: https://doi.org/10.1016/0034-4257(95)00045-3. Geologic Remote Sensing.

[65] PELTZER G., ROSEN P., ROGEZ F., and HUDNUT K. Poroelastic rebound along the landers 1992 earthquake surface rupture. *Journal of geophysical research*, 1998.

[66] Alessandro Ferretti, Andrea Monti-Guarnieri, Claudio Prati, Fabio Rocca, and Didier Massonet. Insar principles - guidelines for sar interferometry processing and interpretation. *ESA Training Manual*, 19, 01 2007.

[67] Zhiwei Li, Xiaoli Ding, and G.X. Liu. Modeling atmospheric effects on insar with meteorological and continuous gps observations: algorithms and some test results. *Journal of Atmospheric and Solar-Terrestrial Physics*, 66(11):907–917, 2004. ISSN 1364-6826. doi: https://doi.org/10.1016/j.jastp.2004.02.006.

[68] David T. Sandwell and Evelyn J. Price. Phase gradient approach to stacking interferograms. *Journal of Geophysical Research: Solid Earth*, 103(B12):30183–30204, 1998. doi: https://doi.org/10.1029/1998JB900008.

[69] Fabio Bovenga, Alberto Refice, Raffaele Nutricato, Luciano Guerriero, and Mt Chiaradia. Spinua: a flexible processing chain for ers/envisat long term interferometry. *Proceedings of ESA-ENVISAT Symposium, Salzburg, Austria*, pages 6–10, 04 2005.

[70] E. Sansosti, F. Casu, M. Manzo, and R. Lanari. Space-borne radar interferometry techniques for the generation of deformation time series: An advanced tool for earth's surface displacement analysis. *Geophysical Research Letters*, 37(20), 2010. doi: https://doi.org/10.1029/2010GL044379.

[71] Andrew Hooper, David Bekaert, Karsten Spaans, and Mahmut Arıkan. Recent advances in sar interferometry time series analysis for measuring crustal deformation. *Tectonophysics*, 514-517:1–13, 2012. ISSN 0040-1951. doi: https://doi.org/10.1016/j.tecto.2011.10.013.

[72] Charles L. Werner, Urs Wegmüller, Tazio Strozzi, and Andreas Wiesmann. Interferometric point target analysis for deformation mapping. *IGARSS 2003. 2003 IEEE International Geoscience and Remote Sensing Symposium. Proceedings (IEEE Cat. No.03CH37477)*, 7:4362–4364 vol.7, 2003.

[73] Javier Duro, Jordi Inglada, Josep Closa, N. Adam, and Alain Arnaud. High resolution differential interferometry using time series of ers and envisat sar data. *European Space Agency, (Special Publication) ESA SP*, pages 99–, 04 2005.

[74] M. Crosetto, Erlinda Biescas, Javier Duro, Josep Closa, and Alain Arnaud. Generation of advanced ers and envisat interferometric sar products using the stable point network technique. *Photogrammetric Engineering and Remote Sensing*, 74:443–450, 04 2008. doi: 10.14358/PERS.74.4.443.

[75] Janusz Wasowski and Fabio Bovenga. Investigating landslides and unstable slopes with satellite multi-temporal interferometry: Current issues and future perspectives. *Engineering Geology*, 174:103–138, 2014. ISSN 0013-7952. doi: https://doi.org/10.1016/j.enggeo.2014.03.003.

[76] S. Usai. A least squares database approach for sar interferometric data. *IEEE Transactions on Geoscience and Remote Sensing*, 41(4):753–760, 2003. doi: 10.1109/TGRS.2003.810675.

[77] Alessandro Ferretti, Claudio Prati, and Fabio Rocca. Nonlinear subsidence rate estimation using permanent scatterers in differential sar interferometry. *Geoscience and Remote Sensing, IEEE Transactions on*, 38:2202 – 2212, 10 2000. doi: 10.1109/36.868878.

[78] O. Mora, J.J. Mallorqui, J. Duro, and A. Broquetas. Long-term subsidence monitoring of urban areas using differential interferometric sar techniques. In *IGARSS 2001. Scanning the Present and Resolving the Future. Proceedings. IEEE 2001 International Geoscience and Remote Sensing Symposium (Cat. No.01CH37217)*, volume 3, pages 1104–1106 vol.3, 2001. doi: 10.1109/IGARSS.2001.976760.

[79] C. Colesanti, A. Ferretti, F. Novali, C. Prati, and F. Rocca. Sar monitoring

of progressive and seasonal ground deformation using the permanent scatterers technique. *IEEE Transactions on Geoscience and Remote Sensing*, 41(7):1685–1701, 2003. doi: 10.1109/TGRS.2003.813278.

[80] B.M. Kampes and R.F. Hanssen. Ambiguity resolution for permanent scatterer interferometry. *IEEE Transactions on Geoscience and Remote Sensing*, 42(11): 2446–2453, 2004. doi: 10.1109/TGRS.2004.835222.

[81] Tazio Strozzi, Pietro Teatini, and Luigi Tosi. Terrasar-x reveals the impact of the mobile barrier works on venice coastland stability. *Remote Sensing of Environment - REMOTE SENS ENVIRON*, 113:2682–2688, 12 2009. doi: 10.1016/j.rse.2009.08.001.

[82] C. Prati, A. Ferretti, and D. Perissin. Recent advances on surface ground deformation measurement by means of repeated space-borne sar observations. *Journal of Geodynamics*, 49(3):161–170, 2010. ISSN 0264-3707. doi: https://doi.org/10.1016/j.jog.2009.10.011. WEGENER 2008 - Proceedings of the 14th General Assembly of Wegener.

[83] N. Adam, Richard Bamler, M. Eineder, and B. Kampes. Parametric estimation and model selection based on amplitude-only data in ps-interferometry. In *Fringe 2005 Workshop, Proceedings of the Conference*, volume 610, page 21, 01 2006.

[84] Nico Adam, Bert Kampes, Michael Eineder, Jirathana Dittrich, and Michaela Kircher. The development of a scientific permanent scatterer system. In *Proceedings of the Joint ISPRS/EARSeL Workshop "High Resolution Mapping from Space 2003"*, 10 2003.

[85] Richard Bamler, Bert Kampes, Nico Adam, and Steffen Suchandt. Assessment of slow deformations and rapid motions by radar interferometry. In *Journal for Geographic Information Systems (GIS)*, volume 2006, 07 2005.

[86] Nico Adam, Bert Kampes, and Michael Eineder. Development of a scientific permanent scatterer system: Modifications for mixed ers/envisat time series. In *Proceedings of the 2004 Envisat & ERS Symposium*, 01 2004.

[87] Nico Adam, Alessandro Parizzi, Michael Eineder, and Michele Crosetto. Practical persistent scatterer processing validation in the course of the terrafirma project. *Journal of Applied Geophysics*, 69(1):59–65, 2009. ISSN 0926-9851. doi: https://doi.org/10.1016/j.jappgeo.2009.07.002. Advances in SAR Interferometry from the 2007 Fringe Workshop.

[88] Tom Rune Lauknes, A. Shanker, John Dehls, H. Zebker, Iain Henderson, and Y. Larsen. Detailed rockslide mapping in northern norway with small baseline and persistent scatterer interferometric sar time series methods. *Remote Sensing of Environment*, 114:2097–2109, 09 2010. doi: 10.1016/j.rse.2010.04.015.

[89] A. Pepe and R. Lanari. On the extension of the minimum cost flow algorithm for phase unwrapping of multitemporal differential sar interferograms. *IEEE Transactions on Geoscience and Remote Sensing*, 44(9):2374–2383, 2006. doi: 10.1109/TGRS.2006.873207.

[90] Gianfranco Fornaro, Antonio Pauciullo, and Diego Reale. A null-space method for the phase unwrapping of multitemporal sar interferometric stacks. *Geoscience and Remote Sensing, IEEE Transactions on*, 49:2323 – 2334, 07 2011. doi: 10.1109/TGRS.2010.2102767.

[91] Alessandro Spata, Francesco Guglielmino, Giuseppe Nunnari, and Giuseppe Puglisi. SISTEM: A New Approach to Obtain Three-Dimensional Displacement Maps by Integrating GPS and DInSAR Data. In H. Lacoste, editor, *ESA Special Publication*, volume 677 of *ESA Special Publication*, page 24, March 2010.

[92] Yuri Fialko, Mark Simons, and Duncan Agnew. The complete (3-D) surface displacement field in the epicentral area of the 1999 M_W7.1 Hector Mine Earth-

quake, California, from space geodetic observations. *grl*, 28(16):3063–3066, August 2001. doi: 10.1029/2001GL013174.

[93] Yuri Fialko, David Sandwell, Mark Simons, and Paul Rosen. Three-dimensional deformation caused by the bam, iran, earthquake and the origin of shallow slip deficit. *Nature*, 435:295–9, 06 2005. doi: 10.1038/nature03425.

[94] Manoochehr Shirzaei. A seamless multitrack multitemporal insar algorithm. *Geochemistry, Geophysics, Geosystems*, 16:n/a–n/a, 05 2015. doi: 10.1002/2015GC005759.

[95] M. Manzo, G.P. Ricciardi, F. Casu, G. Ventura, G. Zeni, S. Borgström, P. Berardino, C. Del Gaudio, and R. Lanari. Surface deformation analysis in the ischia island (italy) based on spaceborne radar interferometry. *Journal of Volcanology and Geothermal Research*, 151(4):399–416, 2006. ISSN 0377-0273. doi: https://doi.org/10.1016/j.jvolgeores.2005.09.010.

[96] Noel Gourmelen, Falk Amelung, and Riccardo Lanari. Interferometric synthetic aperture radar-gps integration: Interseismic strain accumulation across the hunter mountain fault in the eastern california shear zone. *J. Geophys. Res*, 115, 09 2010. doi: 10.1029/2009JB007064.

[97] Antonio Pepe. Advanced differential interferometric sar techniques. In *VDM publishing*, 2007.

[98] Tazio Strozzi, Adrian Luckman, Tavi Murray, and U. Wegmuller. Glacier motion estimation using sar offset-tracking procedures. *Geoscience and Remote Sensing, IEEE Transactions on*, 40:2384 – 2391, 12 2002. doi: 10.1109/TGRS.2002.805079.

[99] Francesco Casu, Andrea Manconi, A. Pepe, and Riccardo Lanari. Deformation time-series generation in areas characterized by large displacement dynamics: The sar amplitude pixel-offset sbas technique. *Geoscience and Remote Sensing,*

IEEE Transactions on, 49:2752 – 2763, 08 2011. doi: 10.1109/TGRS.2010.2104325.

[100] Francesco Casu and Andrea Manconi. Four-dimensional surface evolution of active rifting from spaceborne sar data. *Geosphere*, 12:GES01225.1, 04 2016. doi: 10.1130/GES01225.1.

[101] Taku Ozawa and Hideki Ueda. Advanced interferometric synthetic aperture radar (InSAR) time series analysis using interferograms of multiple-orbit tracks: A case study on Miyake-jima. *Journal of Geophysical Research (Solid Earth)*, 116(B12):B12407, December 2011. doi: 10.1029/2011JB008489.

[102] Author(s) Name(s). InSAR and its applications in geo-engineering: Case studies with ERS-1. In *Book Title*, page Chapter 18. Springer, 2024. doi: 10.1007/978-3-031-76528-5_18. URL `https://link.springer.com/chapter/10.1007/978-3-031-76528-5_18`.

[103] Homa Ansari, Marc Ru*β*wurm, Mohsin Ali, Sina Montazeri, Alessandro Parizzi, and Xiao Xiang Zhu. Insar displacement time series mining: A machine learning approach. In *2021 IEEE International Geoscience and Remote Sensing Symposium IGARSS*, pages 3301–3304, 2021. doi: 10.1109/IGARSS47720.2021.9553465.

[104] Nantheera Anantrasirichai, J. Biggs, Fabien Albino, P. Hill, and D. Bull. Application of machine learning to classification of volcanic deformation in routinely generated insar data. *Journal of Geophysical Research: Solid Earth*, 123, 08 2018. doi: 10.1029/2018JB015911.

[105] Bertrand Rouet-Leduc, Romain Jolivet, Manon Dalaison, Paul A. Johnson, and Claudia Hulbert. Autonomous extraction of millimeter-scale deformation in insar time series using deep learning. *Nature Communications*, 12(1), November

2021. ISSN 2041-1723. doi: 10.1038/s41467-021-26254-3. URL `http://dx.doi.org/10.1038/s41467-021-26254-3`.

[106] P. Maurya and P. Banerjee. Integration of multi-temporal insar and machine learning for landslide susceptibility mapping. *Journal of the Indian Society of Remote Sensing*, 2025.

[107] Ashutosh Tiwari and Nitheshnirmal Sadhasivam. Leveraging power of deep learning for fast and efficient elite pixel selection in time series sar interferometry, 2024. URL `https://www.researchgate.net/publication/378654003_Leveraging_power_of_deep_learning_for_fast_and_efficient_elite_pixel_selection_in_time_series_SAR_interferometry`.

[108] Nikolaos Bountos, Dimitrios Michail, and Ioannis Papoutsis. Learning from synthetic insar with vision transformers: The case of volcanic unrest detection. *IEEE Transactions on Geoscience and Remote Sensing*, 60:1–1, 01 2022. doi: 10.1109/TGRS.2022.3180891.

[109] Hewei Tang, Pengcheng Fu, Honggeun Jo, Su Jiang, Christopher S. Sherman, François Hamon, Nicholas A. Azzolina, and Joseph P. Morris. Deep learning-accelerated 3d carbon storage reservoir pressure forecasting based on data assimilation using surface displacement from insar, 2022. URL `https://arxiv.org/abs/2201.08543`.

[110] P. A. Rosen, S. Hensley, I. R. Joughin, F. K. Li, S. N. Madsen, E. Rodriguez, and R. M. Goldstein. Synthetic aperture radar interferometry. *Proceedings of the IEEE*, 88(3):333–382, 2000. doi: 10.1109/5.838084.

[111] H. Fattahi and F. Amelung. Dem error correction in insar time series. *IEEE Transactions on Geoscience and Remote Sensing*, 51(7):4249–4259, 2013. doi: 10.1109/TGRS.2012.2227761.

[112] D. P. S. Bekaert, A. Hooper, and T. J. Wright. A spatially variable power law tropospheric correction technique for insar data. *Journal of Geophysical Research: Solid Earth*, 120(2):1345–1356, 2015. doi: 10.1002/2014JB011557.

[113] S. Samsonov, K. Tiampo, P. J. R. Gonzalez, and N. d'Oreye. Fast sar interferometry time series analysis using the multidimensional small baseline subset algorithm. *IEEE Transactions on Geoscience and Remote Sensing*, 49(1):383–396, 2010. doi: 10.1109/TGRS.2010.2051959.

[114] Z. Du, L. Ge, A. H. Ng, and X. Li. A new method for correcting insar-derived displacement for l-band data based on gps measurements. *Remote Sensing of Environment*, 197:73–89, 2017. doi: 10.1016/j.rse.2017.05.029.

[115] W. Liu, J. Hu, H. Shen, and L. Zhang. Cross-sensor phase unwrapping for differential sar interferometry. *Remote Sensing*, 11(6):705, 2019. doi: 10.3390/rs11060705.

[116] S. Ghuffar, D. Fritsch, L. Meng, and V. Wichmann. A machine learning approach for large-scale interferometric phase unwrapping. *IEEE Transactions on Geoscience and Remote Sensing*, 51(4):2052–2064, 2013. doi: 10.1109/TGRS.2012.2207902.

[117] Y. Zhang, H. Lin, C. Wang, and X. Fu. A deep learning approach for sar interferometry phase unwrapping. *Remote Sensing*, 13(3):475, 2021. doi: 10.3390/rs13030475.

[118] Y. Dong, H. Wang, and J. Li. Fusion of multi-satellite insar data using deep learning for long-term ground displacement monitoring. *ISPRS Journal of Photogrammetry and Remote Sensing*, 183:95–109, 2022. doi: 10.1016/j.isprsjprs.2021.10.013.

[119] Richard Goldstein and Charles Werner. Radar interferogram filtering for geo-

physical applications. geophysical research letters, 25, 4035-4038. *Geophysical Research Letters*, 25, 11 1998. doi: 10.1029/1998GL900033.

[120] Hongyu Liang, Xin Li, Lei Zhang, Rou-Fei Chen, Xiaoli Ding, Kuo-Long Chen, Chi-Shan Wang, Chia-Shin Chang, and Chien-Yu Chi. Investigation of slow-moving artificial slope failure with multi-temporal insar by combining persistent and distributed scatterers: A case study in northern taiwan. *Remote Sensing*, 12(15), 2020. ISSN 2072-4292. doi: 10.3390/rs12152403.

[121] Antonio Pepe, Giuseppe Solaro, Fabiana Calò, and Claudio Dema. A minimum acceleration approach for the retrieval of multiplatform insar deformation time series. *IEEE Journal of Selected Topics in Applied Earth Observations and Remote Sensing*, 9:3883–3898, 2016.

[122] Per Christian Hansen. The truncatedsvd as a method for regularization. *BIT Numerical Mathematics*, 27:534–553, 1987.

[123] Guntuku Gupta, Amit Kumar, Sharath Chandra, Raghuram Karthik Desu, and Aditya Balu. Optimisation of turning parameters by integrating genetic algorithm with support vector regression and artificial neural networks. *The International Journal of Advanced Manufacturing Technology*, 77(1):331–339, 3 2015. ISSN 1433-3015. doi: 10.1007/s00170-014-6282-9.

[124] Yu Zhang, Qifan Wang, Xiaofei Chen, Yuchao Yan, Ruomiao Yang, Zhentao Liu, and Jiahong Fu. The prediction of spark-ignition engine performance and emissions based on the svr algorithm. *Processes*, 10(2), 2022. ISSN 2227-9717. doi: 10.3390/pr10020312. URL `https://www.mdpi.com/2227-9717/10/2/312`.

[125] Hao Duan, Yue Huang, Roopesh Kumar Mehra, Panpan Song, and Fanhua Ma. Study on influencing factors of prediction accuracy of support vector machine (svm) model for nox emission of a hydrogen enriched compressed natural gas

engine. *Fuel*, 234:954–964, 2018. ISSN 0016-2361. doi: 10.1016/j.fuel.2018.07.009.

[126] F. Pedregosa, G. Varoquaux, A. Gramfort, V. Michel, B. Thirion, O. Grisel, M. Blondel, P. Prettenhofer, R. Weiss, V. Dubourg, J. Vanderplas, A. Passos, D. Cournapeau, M. Brucher, M. Perrot, and E. Duchesnay. Scikit-learn: Machine learning in Python. *Journal of Machine Learning Research*, 12:2825–2830, 2011.

[127] AF Kamel and AA El Sokkary. Geologic hazards assessment of cairo and vicinity. *Natural hazards*, 13(3):253–274, 1996.

[128] Jean Cuvillier. *Revision du Nummulitique egyptein.* Impr. E. & R. Schindler, 1930.

[129] J Cuvillier. A conglomerate in the nummulitic formation of gebel moqattam, near cairo. *Geological Magazine*, 64(11):522–523, 1927.

[130] C.W. Chen and H.A. Zebker. Phase unwrapping for large sar interferograms: statistical segmentation and generalized network models. *IEEE Transactions on Geoscience and Remote Sensing*, 40(8):1709–1719, 2002. doi: 10.1109/TGRS.2002.802453.

[131] Kamila Pawluszek-Filipiak and Andrzej Borkowski. Integration of dinsar and sbas techniques to determine mining-related deformations using sentinel-1 data: The case study of rydułtowy mine in poland. *Remote Sensing*, 12(2), 2020. ISSN 2072-4292. doi: 10.3390/rs12020242.

[132] Lingxiao Wang, Philip Marzahn, Monique Bernier, and Ralf Ludwig. Sentinel-1 insar measurements of deformation over discontinuous permafrost terrain, northern quebec, canada. *Remote Sensing of Environment*, 248:111965, 2020. ISSN 0034-4257. doi: https://doi.org/10.1016/j.rse.2020.111965.

[133] Karl Alfred von Zittel. *Beitraege zur Geologie und Palaeontologie der libyschen Wüste und der angrenzenden Gebiete von Aegypten...* T. Fischer, 1883.

[134] EM El Shazly, MA Abdel Hady, AB Salman, MM El Rakaiby, MA Morsy, IE El Aassy, and MM El Shazly. Geological investigations on gebel el mokattam area. *Remote Sensing Center. Cairo, Egypt*, 23, 1976.

[135] AR Moustafa, F El-Nahhas, and S Abdel Tawab. Engineering geology of mokattam city and vicinity, eastern greater cairo, egypt. *Engineering geology*, 31(3-4): 327–344, 1991.

[136] Maurizio Poscolieri, Is. Parcharidis, Michael Foumelis, and Claudio Rafanelli. Ground deformation monitoring in the greater cairo metropolitan region (egypt) by sar interferometry. *Environmental Semeiotics*, 4:17–45, 2011.

[137] M. H. Aly, H. A. Zebker, J. R. Giardino, and A. G. Klein. Permanent Scatterer investigation of land subsidence in Greater Cairo, Egypt. *Geophysical Journal International*, 178(3):1238–1245, 09 2009. ISSN 0956-540X. doi: 10.1111/j.1365-246X.2009.04250.x.

[138] Qiang Chen, Guoxiang Liu, Xiaoli Ding, Jyr Ching Hu, Linguo Yuan, Ping Zhong, and M. Omura. Tight integration of gps observations and persistent scatterer insar for detecting vertical ground motion in hong kong. *International Journal of Applied Earth Observation and Geoinformation*, 12(6):477–486, June 2010. ISSN 1569-8432. doi: 10.1016/j.jag.2010.05.002.

[139] Alex Hay-Man Ng, Linlin Ge, Xiaojing Li, and Kui Zhang. Monitoring ground deformation in beijing, china with persistent scatterer sar interferometry. *Journal of Geodesy*, 86(6):375–392, 2012.

[140] Liming Jiang and Hui Lin. Integrated analysis of sar interferometric and geological data for investigating long-term reclamation settlement of chek lap kok

airport, hong kong. *Engineering Geology*, 110(3):77–92, 2010. ISSN 0013-7952. doi: 10.1016/j.enggeo.2009.11.005.

[141] Yaru Liu, Lei Wang, and Kaixuan Gu. A support vector regression (svr)-based method for dynamic load identification using heterogeneous responses under interval uncertainties. *Applied Soft Computing*, 110:107599, 2021. ISSN 1568-4946. doi: 10.1016/j.asoc.2021.107599.

[142] Peifeng Ma, Weixi Wang, Bowen Zhang, Jili Wang, Guoqiang Shi, Guangqing Huang, Fulong Chen, Liming Jiang, and Hui Lin. Remotely sensing large- and small-scale ground subsidence: A case study of the guangdong–hong kong–macao greater bay area of china. *Remote Sensing of Environment*, 232: 111282, 2019. ISSN 0034-4257. doi: 10.1016/j.rse.2019.111282.

[143] Thanh Duc Dang, Thomas A. Cochrane, Mauricio E. Arias, and Van Pham Dang Tri. Future hydrological alterations in the mekong delta under the impact of water resources development, land subsidence and sea level rise. *Journal of Hydrology: Regional Studies*, 15:119–133, 2018. ISSN 2214-5818. doi: 10.1016/j.ejrh.2017.12.002.